Electron Paramagnetic Resonance and Photophysical Investigations on Multifunctional Organic Molecules

Dipl.-Ing. Christine Onitsch

DISSERTATION

zur Erlangung des akademischen Grades
einer Doktorin der technischen Wissenschaften
der Studienrichtung
Technische Chemie
erreicht an der
Technischen Universität Graz

Univ.-Prof. Mag.rer.nat. Dr.phil. Georg Gescheidt-Demner
Institut für Physikalische und Theoretische Chemie
Technische Universität Graz

Graz 2010

Für meine Eltern
und Christian

Danksagung

Ich möchte mich an erster Stelle bei meinem Betreuer, Herrn Prof. Dr. Georg Gescheidt-Demner für all das bedanken, was ich während dieser drei Jahre von ihm lernen durfte. Ohne sein mir entgegengebrachtes Vertrauen und seine Unterstützung wäre die vorliegende Arbeit nicht möglich gewesen. Auch danke ich ihm dafür, dass ich meine Ergebnisse auf internationalen Konferenzen in Göteborg, Norwich und Toledo präsentieren durfte.

Bei Prof. Dr. Günter Grampp möchte ich mich für die Betreuung im Projekt „Quenching Experiments with 3-(Carboxymethyl)-lumiflavin“ bedanken, sowie für die Möglichkeit meine Ergebnisse in Berlin, Veszprém und Bad Hofgastein zu präsentieren.

Dem Fond zur Förderung der wissenschaftlichen Forschung (Projekt-Nr.: P20017) danke ich für die Finanzierung meiner Forschungsarbeit, sowie unserem Projektpartner Prof. Dr. Diederich von der ETH Zürich für das Bereitstellen der multifunktionalen Verbindungen.

Ich möchte mich bei allen Mitgliedern des Institutes bedanken, die zum Gelingen meiner Experimente beigetragen haben.

Das größte Dankeschön ergeht an Dr. Arnulf Rosspeintner für alles was ich von ihm durch unsere Zusammenarbeit während der Projekte „Photophysics of an Intramolecular Pyrene Excimer“ und „Extended Phenylenediamines“ lernen durfte, sowie für die komplexe Auswertung der experimentellen Daten in selbigen Projekten. Seine Begeisterung an wissenschaftlicher Arbeit ist ansteckend, und ich beneide jeden der in Zukunft mit ihm zusammenarbeiten darf.

DI Barbara Enko danke ich für die vielen Stunden, die wir gemeinsam vor der Vakuumlinie und vor allem vor unserem geliebten ENDOR verbracht haben, DI Markus Griesser für seine theoretischen Berechnungen an meinen

Molekülen sowie NMR Messungen, Dr. Gonzalo Angulo für die elektrochemischen Messungen, und Dr. Boryana Mladenova Kattnig und Dr. Faiza Jan Iftikhar als langjährige Bürokolleginnen für zahlreiche Diskussionen.

Bei Ing. Helmut Eisenkölbl möchte ich mich dafür bedanken, dass er Tarzan (den ENDOR-Radiofrequenzgenerator) immer wieder zum Laufen gebracht hat und mit Barbara Enko und mir (den zwei Janes) so lange am ESR/ENDOR Spektrometer herumgebastelt hat, bis es wieder funktioniert hat.

Ich danke Hilde Freißmuth dafür, dass sie das Labor immer in Schuss hält und Marion Hofmeister für ihre Unterstützung in administrativen Angelegenheiten. Es ist schön, dass sich in unseren vielen gemeinsamen Mittagspausen auch eine Freundschaft entwickelt hat.

Ich möchte mich an dieser Stelle auch bei meinen Eltern bedanken. Sie haben mir nicht nur diese Ausbildung ermöglicht, sondern sind auch jederzeit hinter mir gestanden und haben mich in allem und jedem bedingungslos unterstützt. Ein einfaches „Danke“ reicht wohl nicht aus.

Christian, wie gut dass ich in Graz studiert habe und Dich kennenlernen durfte. Danke, dass Du mich immer wieder zum Lachen bringst und mir zeigst was wirklich zählt. Diese Arbeit ist Dir und meinen Eltern gewidmet, weil ich es ohne Euch nicht geschafft hätte.

Eidesstattliche Erklärung

Ich erkläre an Eides statt, dass ich die vorliegende Arbeit selbstständig verfasst, andere als die angegebenen Quellen/Hilfsmittel nicht benutzt, und die den benutzten Quellen wörtlich und inhaltlich entnommenen Stellen als solche kenntlich gemacht habe.

Statutory Declaration

I declare that I have authored this thesis independently, that I have not used other than the declared sources/resources, and that I have explicitly marked all material which has been quoted either literally or by content from the used sources.

Graz, im Oktober 2010 ....

Abstract

This thesis addresses the experimental characterization of sophisticated molecules, whose complex functionalities originate mainly in charge-separation and electron transfer. The molecules under investigation are promising candidates for next-generation optoelectronic devices, such as molecular wires, molecular batteries or applications in non-linear optics. In order to investigate their exceptional optical, magnetic and electronic properties, optical spectroscopy together with EPR/ENDOR (Electron Paramagnetic Resonance/Electron Nuclear Double Resonance) spectroscopy were applied.

The work performed comprises experimental studies on the photophysics and quenching behavior of a biologically important flavin derivative, as well as on an intramolecular excimer of pyrene. Extended Wurster-type *p*-phenylenediamines as well as non-planar push-pull chromophores were investigated in terms of their absorption/emission characteristics in a variety of solvents. The electron distribution in charge-separated species was established by magnetic resonance and theoretical calculations. The results constitute a prerequisite for a deeper understanding of the functionalities of these molecules.

Zusammenfassung

Inhalt dieser Dissertation ist die experimentelle Charakterisierung hochentwickelter Moleküle, deren komplexe Funktionalitäten hauptsächlich in Ladungstrennung und Elektronentransfer begründet liegen. Die untersuchten Moleküle sind vielversprechende Kandidaten für optoelektronische Bausteine der nächsten Generation, wie z.B. molekulare Drähte, molekulare Batterien oder Anwendungen in nicht-linearer Optik. Die außergewöhnlichen optischen, magnetischen und elektronischen Eigenschaften dieser Moleküle wurden mithilfe von optischer Spektroskopie und ESR/ENDOR (Elektronenspinresonanz/Electron Nuclear Double Resonance) untersucht.

Die Arbeit umfasst experimentelle Studien zur Photophysik und des Löschverhaltens eines biologisch relevanten Flavin Derivates, sowie an einem intramolekularen Pyren-Excimer. Verlängerte Wurster-ähnliche *p*-Phenylendiamine sowie nicht-planare push-pull Chromophore wurden hinsichtlich ihrer Absorptions- und Emissionseigenschaften in verschiedenen Lösungsmitteln untersucht. Magnetische Resonanz und theoretische Berechnungen erlaubten Rückschlüsse auf die Elektronenverteilung in ladungsgetrennten Zuständen. Die erhaltenen Ergebnisse stellen eine Voraussetzung für ein tieferes Verständnis der Funktionalitäten dieser Verbindungen dar.

Contents

II Experiments 35

Chapter 1

Introduction

In the constant search for new materials, multifunctional organic molecules have gained increasing importance in the recent past as next-generation compounds for molecular optoelectronic devices. The interdisciplinary search involves the fields of organic chemistry, coordination chemistry and physical chemistry. After all, it has been extensively promoted by the increasing popularity of nanotechnology and nanoscience. [1]

Molecules employed in optoelectronic devices have to feature complex functionalities. Interestingly, the functionalities of these sophisticated molecules originate in basic chemical transformations, particularly charge-separation or electron transfer. [1, 2, 3]

However, the relationship between structural geometry and molecular properties of these multifunctional molecules is not straightforward and renders an effective search difficult. Advantageously, Electron Paramagnetic Resonance (EPR) and optical spectroscopy can be applied in order to establish correlations between the molecules' geometry and their unusual optical, magnetic and electronic properties.

The present thesis addresses the characterization of charge-transfer molecules featuring versatile functionalities. It contributes to the understanding of how these molecules interact, how they react to external stimuli and how modifications in the molecular design influence and control their molecular properties. Applying Electron Paramagnetic Resonance together with optical spectroscopy allows us to elaborate principle differences between various donor-acceptor systems and to shed light onto electron distribution upon electron addition or removal, respectively.

The obtained results permit a better insight into how these molecules function and are intended to contribute to facilitating the selective design of novel materials. The charge-transfer molecules under investigation within the scope of this work are promising candidates for potential applications in:

- *Molecular wires.* Molecular wires feature long-distance electron transfer and are reported to even conduct electrical current [4]. Applications reach from light-emitting diodes to single-molecule conductors, flash memory devices, chemical sensors or light harvesting arrays [5, 6].
- *Molecular batteries.* Molecules applied in molecular batteries have to feature exceptional electron uptake and storage capacities, such as *e.g.* dendritic donor-acceptor systems [7].
- *Organic photovoltaic devices.* Eligible candidates for application in organic photovoltaic devices have to feature *e.g.* broad absorption spectra combined with high extinction coefficients as well as suitable redox energies [8].
- *Non-linear optics.* Materials featuring non-linear optical properties can potentially facilitate all-optical computing and signal-processing [9, 10].

In the first part of the present thesis, the concepts of EPR, ENDOR and of paramagnetic organic species in general are elucidated to an extent relevant to this work. The chapters on EPR (chapter 2) and ENDOR (chapter 3) constitute an attempt to cover the physical fundamentals of two instrumental techniques used to characterize paramagnetic species within the scope of this work. The author likes to stress that emphasis was intentionally placed on a phenomenological approach to these topics, as an exact derivation of quantummechanical coherences should be ceded to theoreticians. Chapter 4 is intended to give a short overview of organic radicals, especially the methods of their generation. These three chapters establish the theoretical background.

The second part of this thesis is devoted to the experiments performed. It can be structured in three subject areas, comprising quenching experiments with a biologically relevant molecule (chapter 5), the photophysical characterization of a pyrene-derived excimer (chapter 6) as well as the main project, the photophysical and EPR/ENDOR investigations on novel organic materials (chapters 7 and 8).

Chapter 7 deals with the analysis of extended Wurster-type *p*-phenylenediamines. The molecules under investigation in this chapter serve as precursor substances for push-pull chromophores. Their analysis in terms of their electronic properties and their absorption/emission behavior in various solvents, respectively, make up a central core topic of this thesis. We succeeded in generating radical anions by means of reduction on a K metal mirror and prove their existence by EPR/ENDOR. Given the dominance of examples for radical cations of *p*-phenylenediamines in the literature, the characterization of radical anions of this type can be considered a substantial contribution to this field.

Chapter 8 covers the characterization of non-planar push-pull chromophores in terms of their optical and magnetic properties. The non-planar push-pull chromophores under investigation can be organized in four groups:

- donor-substituted tetracyanobutadienes (section 8.2),
- donor-substituted tetracyanoquinodimethanes (section 8.3),
- donor-substituted F_4-tetracyanoquinodimethanes (section 8.4) and
- donor-substituted octacyano[4]dendralenes (section 8.5).

All molecules have in common that they act as strong electron acceptors, despite substitution with donor moieties, and feature exceptional intramolecular charge-transfer interactions. An application of these molecules as next-generation compounds for optoelectronic devices seems promising, as they act as environmentally stable p-type dopants. [7]

Part I

Theoretical Background

Chapter 2

Electron Paramagnetic Resonance

Electron Paramagnetic Resonance (from now on referred to as EPR), also called Electron Spin Resonance (ESR), is a spectroscopic method working most commonly in the X-band microwave region of the electromagnetic spectrum. Definite resonance conditions being met, EPR studies the interactions between electronic magnetic moments and a magnetic field. EPR is a powerful technique for the selective detection of paramagnetic species. An EPR spectrum is usually visualized as the first derivative of the absorption spectrum.

Since the first magnetic resonance experiments were reported by E. K. Zavoisky on salts of transition metals in 1945 in Kazan (today in the Russian Federation) [11], as well as by Cummerow [12] and Bagguley [13] at almost the same time, the technique of Electron Paramagnetic Resonance was exploited rapidly. Its wide scope of applications in chemistry [14], physics, biology [15], materials sciences and food industry did not become fully amenable until technological progress promoted advancement from continuous-wave to pulsed-EPR [16] and multiresonance techniques such as Electron Nuclear Double Resonance (ENDOR) [17] or TRIPLE resonance techniques [18], respectively.

Today, EPR spectroscopy constitutes an established and valuable method for the selective and incontrovertible detection of paramagnetic species.
Molecules amenable to EPR spectroscopy can either be inherently paramagnetic or be transformed to paramagnetic stages by means of *e.g.* chemical methods or light irradiation. A surprisingly large number of molecules possesses unpaired electrons, however most substances are diamagnetic in their

parent state and can be studied by means of Nuclear Magnetic Resonance (NMR). It is thus not surprising that today, NMR is a more wide-spread technique, even though EPR was developed one year before NMR. However, it is the selectivity for paramagnetic species that makes EPR so interesting.

Systems which can be studied by means of EPR comprise organic and inorganic radicals, *i.e.* biradicals, triplet radicals, stages of higher multiplicity as well as transition group ions or natural systems [19, 20]. Time-resolved EPR techniques are applied to study transient radical species (*e.g.* in [21]).

Among industrial applications of EPR spectroscopy, the determination of anti-oxidant capacity in beer [22], wine [23] and tea [24] by means of spin-trapping technique is widely-spread. In biological sciences, EPR spectroscopy is *e.g.* applied to the study of photosynthetic systems [25, 26]. Practical applications in medical sciences include the usage of EPR for quality control for orthopedic polyethylene implants in terms of radiation degradation as well as radiation dosimetry with the stable radical of L-alanine. In environmental sciences, EPR spectroscopy is used for the detection of polycyclic aromatic hydrocarbons after oxidation to their radical cations [15].

In order to elucidate the phenomenon of electron paramagnetic resonance in the liquid phase, this chapter starts with an introduction to the spin of an electron and the Zeeman effect. Different models giving rise to the typical pattern of EPR spectra will be presented. Furthermore, this chapter includes the physical fundamentals for ENDOR, a double resonance technique, which shall be described in more detail in chapter 3.

2.1 Physical Fundamentals

2.1.1 The Spin of an Electron

Electrons possess an intrinsic, non-classical, mechanical angular momentum called spin. After the experiments of Stern and Gerlach, which prove that the magnetic moment of an electron can only have two discrete energy levels, the concept of spin was first introduced by Uhlenbeck and Goudsmit five years later in 1925 [27].
The electron spin is characterized by its spin quantum number $S = 1/2$, whereas its z component is characterized by the magnetic spin quantum number m_S. An electron can now exist in two spin states, namely

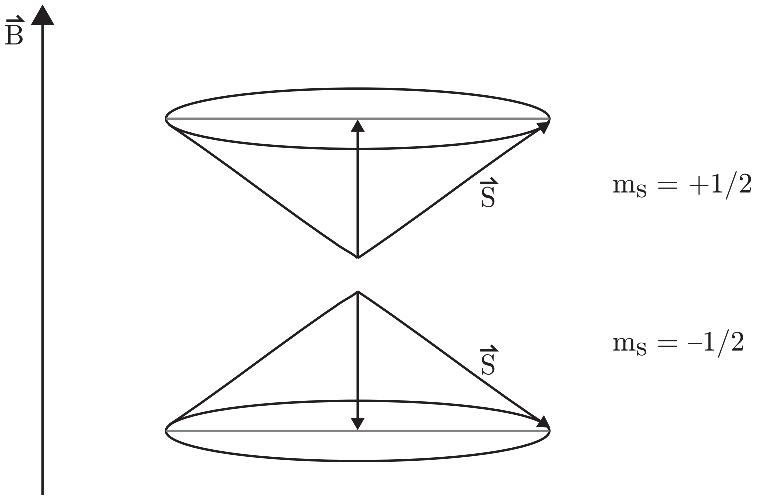

Figure 2.1: Precession of the spin $\vec{S}$ in z direction about the magnetic field $\vec{B}$. [28]

$$\begin{array}{ll} m_S = +1/2: & \text{spin-up } (\uparrow) \text{ or } \alpha \quad \text{and} \\ m_S = -1/2: & \text{spin-down } (\downarrow) \text{ or } \beta \end{array}$$

which are degenerate as long as there is no external magnetic field present. [28, 29]

In a magnetic field $\vec{B}$, the spin can be regarded as a vector $\vec{S}$ precessing about $\vec{B}$ in z direction. This is illustrated in figure 2.1. [28]

The magnetic moment $\vec{\mu}_e$ comes associated to the spin as a rotating charge:

$$\vec{\mu}_e = g_e \mu_B \vec{S} \tag{2.1}$$

where g_e stands for the dimensionless g factor of the free electron (g_e = 2.0023*). μ_B is the Bohr magneton (μ_B = -9.2741*10^{-24} J/T)

$$\mu_B = \frac{-|e|h}{4\pi m_e} \tag{2.2}$$

where e is the electronic charge, h is Planck's constant (h = 6.624*10^{-34} Js) and m_e is the mass of an electron. Note that the Bohr magneton is negative, which means that $\vec{\mu}_e$ and $\vec{S}$ are antiparallel (see figure 2.1). [29]

---

[*] g_e = 2.002319304386(20), one of the most accurately known physical constants [19].

2.1.2 Zeeman Splitting and Resonance Condition

When the electron is placed into a magnetic field, the energy E is determined by the size of the magnetic moment $\vec{\mu}_e$ and the strength of the magnetic field B:

$$E = -\vec{\mu}_e \cdot \vec{B} = g_e|\mu_B|m_S B \tag{2.3}$$

where B is the magnetic field strength in tesla (T)*.

As a consequence, the energies are different for α and β spins in a magnetic field.

$$\begin{array}{lll} E_{\alpha_e} = +(1/2)g_e|\mu_B|B & \text{for} & m_S = +1/2 \\ E_{\beta_e} = -(1/2)g_e|\mu_B|B & \text{for} & m_S = -1/2 \end{array} \tag{2.4}$$

This splitting of the energy is called Zeeman splitting and is illustrated in figure 2.2. Spin inversions thus follow the selection rule $\Delta m_S = \pm 1$.

Absorption of electromagnetic radiation $h\nu_e$ can raise the electron spin from its β state (the lower Zeeman energy state) to its α state (the higher Zeeman energy state) if it complies with two requirements:

- The magnetic vector of the radiation $h\nu_e$ has to be perpendicular to the direction of the magnetic field $\vec{B}$ and
- its energy has to equal the energy difference between α and β states.

$$h\nu_e = E_\alpha - E_\beta = g_e|\mu_B|B \tag{2.5}$$

Equation 2.5 is of fundamental importance in EPR spectroscopy and is known as resonance condition.
The ratio between frequency ν_e and magnetic field strength B is given by the gyromagnetic ratio of the electron γ_e and equals 28.024 $^{\text{MHz}}/_{\text{mT}}$ for the free electron. [28, 29]

$$\gamma_e = \frac{\nu_e}{B} = \frac{g_e|\mu_B|}{h} \tag{2.6}$$

---

* 1 tesla (T) = 1 $^{\text{kg}}/_{\text{sC}}$ = 1 $^{\text{Js}}/_{\text{Cm}^2}$ = 1 $^{\text{Vs}}/_{\text{m}^2}$ = 1*10^4 gauss (G) [19]

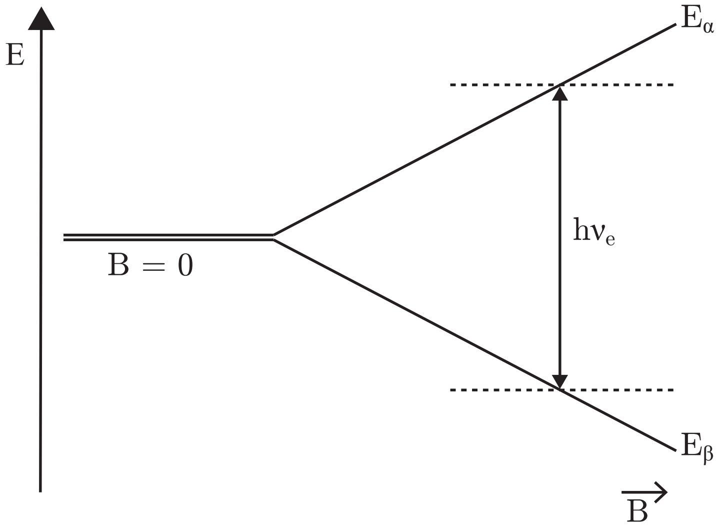

Figure 2.2: Energy-level scheme of a free electron showing Zeeman splitting as a function of the magnetic field strength B.

2.1.3 Relaxation

Subject of the EPR experiment is not a single electron, but many interacting electrons. Therefore, Boltzmann distribution law as given in equation (2.7) has to be considered:

$$\frac{n_\alpha}{n_\beta} = exp\left(\frac{-(E_{\alpha_e} - E_{\beta_e})}{kT}\right) = exp\left(\frac{-g_e|\mu_B|B}{kT}\right) \tag{2.7}$$

where k stands for Boltzmann constant (k = 1.3806*10^{-23} J/K) and T is the absolute temperature in K.
According to the Boltzmann distribution, the populations of the α and β states, n_α and n_β, respectively, are equal in the absence of a magnetic field. For $B > 0$, n_β is about 1/1000th part larger than n_α which means that more spins reside in the lower level energy state at room temperature [29]. Absorption of $h\nu_e$ now lifts the spins from the β to the α state whereas as a next step stimulated emission from α to β will take place. The Einstein coefficients being equal for the up- and down-transitions [30], it is due to the small excess of spins in the lower state that a net absorption of $h\nu_e$ can be observed. [28]

The returning of the so-called "hot spins" to the lower energy level β is enabled *via* spin-lattice relaxation: The lattice, so to speak the environment of the spins, is taking up the emitted energy and thus restores the thermal

equilibrium. This relaxation effect allows for a continuous absorption in the continuous-wave EPR experiment (CW-EPR). [29, 31]
The efficiency of spin-lattice relaxation is given by the inverse of the spin-lattice relaxation time T_e, the time it takes for $1/e$ of all "hot spins" to drop down. Spin-lattice relaxation can be attributed to spin-orbit coupling, which due to a lack of heavy atoms is weak for organic radicals. The spin-relaxation time is therefore rather long for organic radicals. [28]

2.2 Electron-Nuclear Interaction

In general, the EPR spectrum does not consist of a single line, as one would expect due to the explanations given above. In fact, most EPR spectra consist of several lines – the hyperfine structure – as a result of the interaction of the unpaired electron with the nucleus. [32]

2.2.1 Nuclear Spin and Nuclear-Zeeman Effect

Analogous to the electrons, nuclei possess a nuclear spin $\vec{I}$ and a nuclear magnetic moment $\vec{\mu}_n$.

$$\vec{\mu}_n = g_n \mu_N \vec{I} \tag{2.8}$$

where g_n is the g factor of the nucleus, which is positive as for protons or negative as for ^{15}N. μ_N is the nuclear magneton ($\mu_N = 5.0508*10^{-27}\,\mathrm{J/T}$). A selection of nuclear spins I is given in table 2.1. Note that the nuclear magnetic moment $\vec{\mu}_n$ is about three orders of magnitude smaller than its electron counterpart $\vec{\mu}_e$ due to the fact that μ_N is smaller than the Bohr magneton μ_B by a factor of $m_p/m_e = 1836$. [28]

The nuclear-Zeeman effect now describes the energy of nuclear spins as a function of the magnetic field [28, 19]:

$$E = -\vec{\mu}_n \cdot \vec{B} = -g_n \mu_N m_I B \tag{2.9}$$

where m_I is the nuclear magnetic spin quantum number. This gives

$$\begin{aligned} E_{\alpha_n} &= -(1/2) g_n \mu_N B \qquad \text{for} \qquad m_I = +1/2 \\ E_{\beta_n} &= +(1/2) g_n \mu_N B \qquad \text{for} \qquad m_I = -1/2 \end{aligned} \tag{2.10}$$

The resonance condition for NMR transitions can thus be expressed as follows [28]:

$$h\nu_n = g_n \mu_N B \tag{2.11}$$

Table 2.1: Nuclear spin quantum numbers I of selected magnetic nuclei.

^{12}C, ^{16}O	0
^{1}H, ^{13}C, ^{15}N	1/2
^{14}N	1
^{39}K	3/2
^{25}Mg	5/2
^{133}Cs	7/2

2.2.2 Hyperfine Splitting

The nuclear magnetic moment $\vec{\mu}_n$ itself gives rise to a magnetic field which interacts with the electron spin and influences the resonance condition. This leads to a splitting up of the EPR line into $2I + 1$ components – the hyperfine splitting. A small selection of nuclear spins relevant to EPR studies on organic radicals is given in table 2.1. [29]

The hyperfine interaction is composed of two terms: the classical, dipolar term E_{dip} leading to anisotropic hyperfine splitting and the quantum-mechanical Fermi contact term E_{Fc} responsible for isotropic hyperfine splitting. [28]

Dipolar Interaction Term

The dipolar interaction describes the hyperfine field external to the nucleus in a classical way. E_{dip} depends on the angle between the magnetic field and the vector joining the magnetic moment of the electron and of the nucleus in the form of $3\cos^2\phi - 1$. Furthermore, E_{dip} decreases with the third power of the distance between the electron and the nucleus. [28]

In liquid media, the dipole-dipole interaction is thus usually averaged out by the Brownian motion. Therefore, E_{dip} leads to anisotropic hyperfine splitting in solid media, *i.e.* solid samples or frozen solutions. [32]

Fermi Contact Term

The second contribution to hyperfine splitting is made up by the quantum-mechanical Fermi contact term E_{Fc}. E_{Fc} deals with the hyperfine field of the electron spin which enters the nuclear volume. It is responsible for isotropic splitting *i.e.* it is not dependent on spatial orientation.

The hyperfine coupling constant A is a function of the electron spin density φ_S on the nucleus and constitutes the distance between two EPR lines of a multiplet [29]. While the unit of the hyperfine coupling constant A is Joule (or a frequency unit, *e.g.* MHz, for A/h), the unit of the hyperfine splitting constant a is Tesla. The interconversion of the two constants follows $a = A/hg|\mu_B|$ [19]. As only s orbitals allow for spin density to be present at the position of the nucleus, φ_S is equivalent to the s orbital spin population (for spin density see equation 2.20). [33]

$$A = (2\mu_0/3)g_e|\mu_B|g_n\mu_N\varphi_S \tag{2.12}$$

where μ_0 is the permeability of vacuum ($\mu_0 = 4\pi{*}10^{-7}\,\mathrm{T^2m^3/J}$). [19]

At high magnetic fields, the energy given by the electron-Zeeman interaction is weakly perturbated by the nuclear-Zeeman interaction and the hyperfine interaction $a\vec{S}\cdot\vec{I}$ ("high field approximation").

$$E_{tot} = g_e|\mu_B|m_SB - g_n\mu_Nm_IB + Am_Sm_I \tag{2.13}$$

This yields in four different energies for a system of a free radical with $S = 1/2$ with one magnetic nucleus with $I = 1/2$ [29]:

$$\begin{aligned}
E_{\alpha_e\beta_n} &= +1/2g|\mu_B|B + 1/2g_N\mu_NB - A/4\\
E_{\alpha_e\alpha_n} &= +1/2g|\mu_B|B - 1/2g_N\mu_NB + A/4\\
E_{\beta_e\beta_n} &= -1/2g|\mu_B|B + 1/2g_N\mu_NB + A/4\\
E_{\beta_e\alpha_n} &= -1/2g|\mu_B|B - 1/2g_N\mu_NB - A/4
\end{aligned} \tag{2.14}$$

Applying the selection rules for EPR transitions

$$\Delta m_S = \pm 1 \qquad \text{and} \qquad \Delta m_I = 0 \tag{2.15}$$

yields only two allowed EPR transitions:

$$\nu_{\mathrm{EPR}_1} = \frac{E_{\alpha_e\alpha_n} - E_{\beta_e\alpha_n}}{h} = \frac{g|\mu_B|B + A/2}{h} \tag{2.16}$$

$$\nu_{\mathrm{EPR}_2} = \frac{E_{\alpha_e\beta_n} - E_{\beta_e\beta_n}}{h} = \frac{g|\mu_B|B - A/2}{h} \tag{2.17}$$

As the EPR experiment is usually performed at fixed frequency upon varying the magnetic field, transformations of the equations above give [29]:

$$B_1 = \frac{h\nu}{g|\mu_B|} - (A/2)g|\mu_B| \tag{2.18}$$

$$B_2 = \frac{h\nu}{g|\mu_B|} + (A/2)g|\mu_B| \tag{2.19}$$

The situation described above and in figure 2.3 results in an EPR spectrum with two signals, separated by the hyperfine splitting constant a, whereas for $a > 0$ the transition between the two positive m_I states gives rise to the low-field signal (EPR_1) and the transition between the two negative m_I states gives rise to the high-field signal (EPR_2).

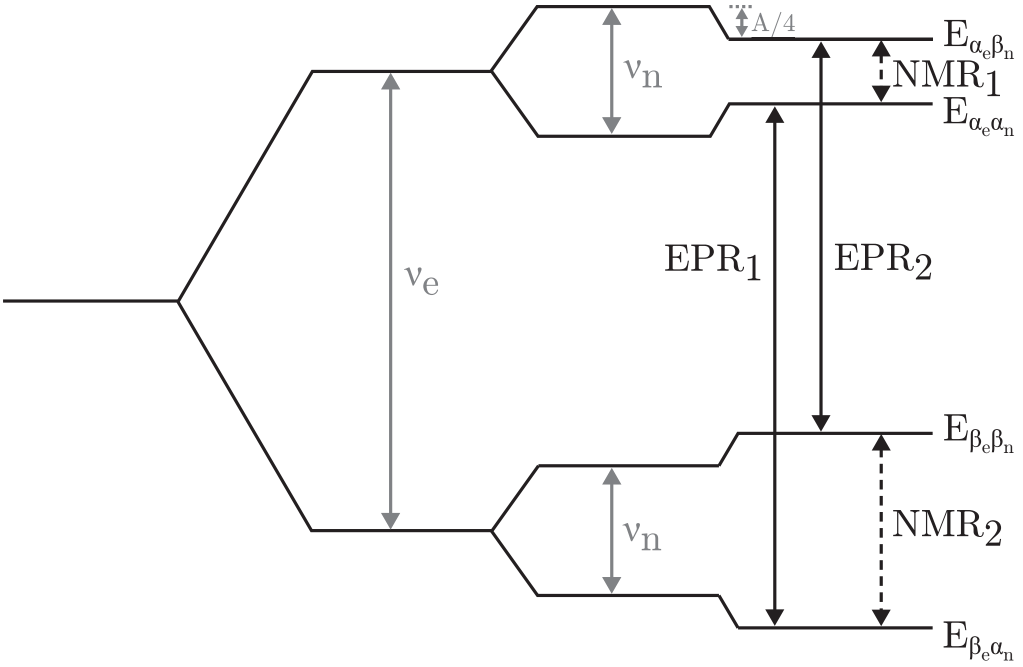

Figure 2.3: Energy-level diagram for one unpaired electron $S = 1/2$ with one nucleus $I = 1/2$ at high magnetic field. Electron-Zeeman, nuclear-Zeeman and hyperfine interaction with the nuclear spin are illustrated for positive values of the isotropic hyperfine coupling constant A and a nucleus with $g_n > 0$, *e.g.* a proton, for the case $A/2 < \nu_n$. Whereas the level for α spins of the electron is higher than for β spins, the situation is opposite for nuclei with $g_n > 0$. Hyperfine interaction stabilizes (lowers) the levels with opposite signs of m_S and m_I, whereas it destabilizes the levels of same sign, both by a factor of $A/4$.
Solid arrows show the two allowed EPR transitions ($\Delta m_S = \pm 1$ and $\Delta m_I = 0$), dashed arrows show the allowed NMR transitions ($\Delta m_S = 0$ and $\Delta m_I = \pm 1$). ν_e and ν_n are defined by their respective resonance conditions. [28]
Scheme is not to scale for reasons of clarity.

In general, there are five contributions to the overall interaction the electron experiences in the magnetic field: the electron-Zeeman interaction $\vec{S}\cdot\vec{B}$, the nuclear-Zeeman interaction $\vec{I}\cdot\vec{B}$, the fine splitting which is only relevant to triplets $\vec{S}\cdot\vec{S}$, the hyperfine splitting $\vec{S}\cdot\vec{I}$ as discussed above and a nuclear-nuclear contribution $\vec{I}\cdot\vec{I}$ also called spin-spin coupling. [28]
As given by the selection rules, EPR transitions take place between energy levels of the same nuclear spin state. The contribution of the nuclear-Zeeman effect is thus canceled out. In EPR spectroscopy, only the terms $\vec{S}\cdot\vec{B}$, $\vec{S}\cdot\vec{S}$ (for radicals with more than one unpaired electron) and $\vec{S}\cdot\vec{I}$ have to be taken into account, whereas $\vec{S}\cdot\vec{B} > \vec{S}\cdot\vec{I}$. [28]

2.2.3 Hyperfine Splitting of Equivalent Nuclei

An additional nucleus adds an additional splitting of every line into again $2I + 1$ lines. This leads to a total of $(2I + 1)^n$ lines for n nuclei, whereas it is being reduced to $2nI + 1$ lines for equivalent nuclei. For equivalent nuclei, some lines can coincide due to degenerate energy levels. This leads to an increased intensity in the order of the degeneration as shown by Pascal's triangle in figure 2.4.

2.3 Isotropic Hyperfine Structure of π Radicals

Hyperfine structure is attributed to the portion of spin at the position of the magnetic nucleus, as discussed in chapter 2.2.2 (see equation 2.12). As only s orbitals allow for spin density to be present at the position of the nucleus, it means that a portion of spin has to have s character if a hyperfine structure (HFS) shall be observed. In *e.g.* π orbitals, the nucleus lies in the nodal plane where no spin density is observed.

In most organic radicals, the spin does not reside in s orbitals where it is detectable but is delocalized between π orbitals. So the question is, how can π radicals then give rise to a hyperfine coupling constant? The answer is, the unpaired electron couples to adjacent α and β protons*. [32]

---

* Note that here, α and β have different meanings than before: they denote the position of the proton in regard to the atom bearing the free π electron. α protons are bound directly to the atom bearing the π electron whereas β protons are separated by two bonds from the atom and so on. In this case, α and β has nothing to do with spin-up or spin-down.

$I = 1/2$

$n = 0$: 1

$n = 1$: 1 1

$n = 2$: 1 2 1

$n = 3$: 1 3 3 1

$n = 4$: 1 4 6 4 1

$n = 5$: 1 5 10 10 5 1

$I = 1$

$n = 0$: 1

$n = 1$: 1 1 1

$n = 2$: 1 2 3 2 1

$n = 3$: 1 3 6 7 6 3 1

$n = 4$: 1 4 10 16 19 16 10 4 1

$n = 5$: 1 5 15 20 45 51 45 20 15 5 1

Figure 2.4: Pascal's triangle showing the intensity ratio of EPR lines for one unpaired electron $S = 1/2$ coupled to n equivalent nuclei with $I = 1/2$, *e.g.* protons (top) and $I = 1$, *e.g.* nitrogens (bottom), respectively.

Before going into detail with the coupling to α protons (by means of spin polarization) and the coupling to β protons (by means of hyperconjugation), the difference between spin density and spin population shall be discussed first. The two terms are closely related to each other, but are not the same.

Spin Density

Spin density φ_S is defined as the difference between contributions due to spin-up (α) and spin-down (β) electrons in m^{-3}:

$$\varphi_S = \varphi^\alpha - \varphi^\beta \tag{2.20}$$

For systems with at least one unpaired electron, it is in general positive or sometimes zero. However, in some cases as shown below, when β spin predominates it can be negative as well. [28]

Spin Population

Spin population φ_X^Ψ , on the other hand, is considered an integrated spin density in the orbital Ψ centered on nucleus X. As given by the definition in equation 2.21, φ_X^Ψ is positive if it is more probable to find the unpaired electron with α spin than with β spin and *vice versa* [28]. The spin population is dimensionless and the sum of spin populations of all centers is 1. [34]

$$\varphi_X^\Psi = \varphi_X^{\Psi\alpha} - \varphi_X^{\Psi\beta} \tag{2.21}$$

2.3.1 Spin Polarization

Given a typical organic π radical, like the benzene radical, the unpaired electron resides in the $\mathrm{p_z}$ orbital whose axis stands perpendicular to the sp^2 hybrid plane (compare the C−H fragment scheme in figure 2.5). As ^{12}C is not a magnetic nucleus, the EPR signal pattern from the benzene radical has to derive from the ^{1}H nuclei. The ^{1}H nuclei, however, lie in the nodal plane of the π system. This means that on the very spot of the protons, the probability of finding the free π electron is zero and can thus not give rise to an EPR signal. [32]

However, the unpaired electron shows a repulsive interaction with the formally paired spins in the C−H bond. This is called π,σ-interaction. As a consequence of Hund's rule, electrons with opposite spin can approach closer than electrons with same spin can do. This implies a slightly weaker repulsive interaction between the spin in the SOMO (Singly Occupied Molecular

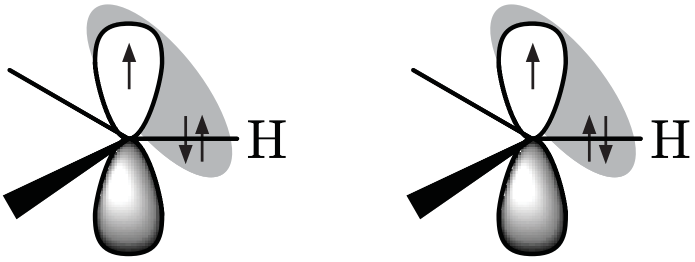

Figure 2.5: Principle of spin polarization schematically illustrated on a C−H fragment of the benzene radical. Left case: singlet spin arrangement, right case: triplet spin arrangement. The triplet is energetically favored, which leaves the β spin on the H atom and results in a negative a_{H}.

Orbital) of the π system, which is by convention an α spin, with the α spin from the C−H bond. As a consequence, the α spin is more likely to be found closer to the π system than the β spin. The β spin remains on the H atom giving rise to a negative spin density on the H atom (as given by equation 2.20) and as a consequence, a negative coupling constant on the H atom. [33] Regarding the C, the electron in the p_z orbital and the one originating from the σ bond but now close to the π system can be seen as a triplet (right case in figure 2.5) or as singlet (left case in figure 2.5). As triplets are slightly more stable, this case is more likely to be found. [28]

McConnell postulated that the hyperfine splitting constant of an H atom a_{H} is proportional to the spin population on the adjacent C atom $\varphi_{\mathrm{C}}^{\pi}$ [35]. This linear relationship is today known as McConnell equation (given in equation 2.22). McConnell determined the proportionality constant Q to be approximately -2.25 mT for aromatic C−H bonds [36, 37]. Its negative sign accounts for the negative coupling constant as a result of the mechanism of spin polarization.

$$a_{\mathrm{H}} = Q_{\mathrm{C-H}}^{\mathrm{H}} * \varphi_{\mathrm{C}}^{\pi} \tag{2.22}$$

2.3.2 Hyperconjugation

Whereas spin density describes the coupling of α protons, hyperconjugation describes the coupling to protons which are “farther apart”, so to speak β protons (compare figure 2.6). It can be observed in alkylsubstituted free π systems that spin is transfered in a direct way *via* hyperconjugation from a p_z orbital to a H_β atom. This direct spin transfer mechanism takes place upon retention of the spin state of the π orbital (which is by convention spin-up)

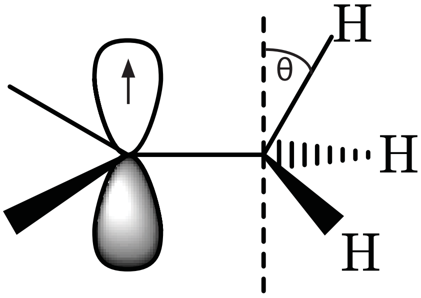

Figure 2.6: Principle of hyperconjugation schematically illustrated on a C−H fragment attached to a benzene radical.

and therefore leads to a positive sign of the hyperfine splitting constant a_{H_β}.

$$a_{\mathrm{H}_\beta} = \varphi^{\pi}_{\mathrm{C}_\alpha} * (A' + B' \cos^2 \Theta) \tag{2.23}$$

Here A' and B' are empirically describing spin transfer due to spin polarization and hyperconjugation, respectively. A' is usually much smaller than B' accounting for the fact that spin polarization is very weak over two σ bonds and can almost be neglected. It is interesting to note that B' depends on the charge of the π center: it is about 4-5 mT for radical anions and about 8-9 mT for radical cations. [33]
Θ denotes the dihedral angle formed by the $\mathrm{p_z}$ orbital and the $\mathrm{C{-}H}_\beta$ σ bond of the alkyl group. The size of a_{H_β} depends on the spatial orientation as indicated by the term $\cos^2 \Theta$ in equation 2.23. It is maximum for $\Theta = 0\,^\circ$, so to speak when the $\mathrm{p_z}$ orbital and the $\mathrm{C{-}H}_\beta$ σ bond of the alkyl group are parallel to each other. For $\Theta = 90\,^\circ$, hyperconjugation is ineffective due to $\cos 90 = 0$. For freely rotating alkyl groups, a_{H_β} is averaged out and becomes identical for all protons of the alkyl group. [28, 33]

Chapter 3

Electron Nuclear Double Resonance

The interaction of several magnetic nuclei in a radical can lead very fast to complicated and unresolved EPR spectra. Due to line broadening and splitting in a considerate number of lines, EPR spectra may loose important information about their hyperfine structure [33]. Analyzing paramagnetic species with NMR spectroscopy seems to be an alternative, however, this is as well problematic due to line broadening effects caused by fast electron spin relaxation.

ENDOR, a double resonance technique, helps to overcome the limited resolution of EPR and the low sensitivity of NMR. ENDOR stands for Electron Nuclear DOuble Resonance and was first applied to solids by Feher in 1956 [17] and by Hyde and Maki to organic radicals in solution in 1964 [38]. In ENDOR spectroscopy the sample is exposed to two resonant fields: NMR resonances are detected *via* intensity changes of an EPR line, which is simultaneously irradiated. ENDOR can thus be considered an NMR technique performed on an EPR spectrometer [39].

3.1 Principles of ENDOR

ENDOR, as mentioned before, is a double resonance technique. This means that the sample is exposed to two resonant fields simultaneously: one in the microwave region as in classical EPR and the second one in the radiofrequency region as in classical NMR. As a consequence, in order to understand how ENDOR works, one not only has to consider EPR selection rules but as well NMR selection rules. Referring back to section 2.2.2 (figure 2.3) and to what was deduced from there for EPR transitions, the same procedure shall now be applied for NMR transitions for the case $0 < A/2 < \nu_n$.

Applying the selection rules for NMR transitions,

$$\Delta m_S = 0 \qquad \text{and} \qquad \Delta m_I = \pm 1 \tag{3.1}$$

yields only two allowed NMR transitions [19, 28]:

$$\nu_{\mathrm{NMR}_1} = \frac{E_{\alpha_e\beta_n} - E_{\alpha_e\alpha_n}}{h} = \frac{g_N\mu_N B - A/2}{h} \tag{3.2}$$

$$\nu_{\mathrm{NMR}_2} = \frac{E_{\beta_e\beta_n} - E_{\beta_e\alpha_n}}{h} = \frac{g_N\mu_N B + A/2}{h} \tag{3.3}$$

Combining these findings with the resonance condition for NMR transitions as given in equation 2.11, gives what is called the ENDOR resonance condition [40]:

$$\nu_{\mathrm{ENDOR}} = |\nu_n - Am_S| \tag{3.4}$$

In order to illustrate the ENDOR effect, the Boltzmann population levels have to be taken into account. While the population difference between the nuclear spin levels is neglectably small, there is a population difference between the electronic levels as already pointed out in section 2.1.3. In figure 3.1, this excess population in the two lower energy levels (those with β spin) is visualized by means of the four dots. [28]

In order to perform an ENDOR experiment, one EPR line is selected (in the case as shown in figure 3.1, it is EPR_1 line). Upon increasing the microwave power on EPR_1 transition, the “hot spins” do not manage to return back to the lower energy level as the induced absorption rate is being enhanced to an extent where it competes with spin-lattice relaxation. This results in a (partial) saturation of the EPR_1 line and a much smaller EPR signal. [39, 40]

At this point, radiofrequency comes into play. Intense radiofrequency applied between the two upper energy levels equalizes the population of the two levels of NMR_1 transition *via* induced absorption. This results in a partial desaturation of the EPR_1 transition and thus an increase of the EPR_1 line: the first ENDOR line arises. Applying an intense radiofrequency between the two lower energy levels equalizes the population of the two levels involved in NMR_2 transition *via* induced emission. This results again in a partial desaturation of the EPR_1 transition and thus an increase of the EPR_1 line: the second ENDOR line arises. [39, 40]

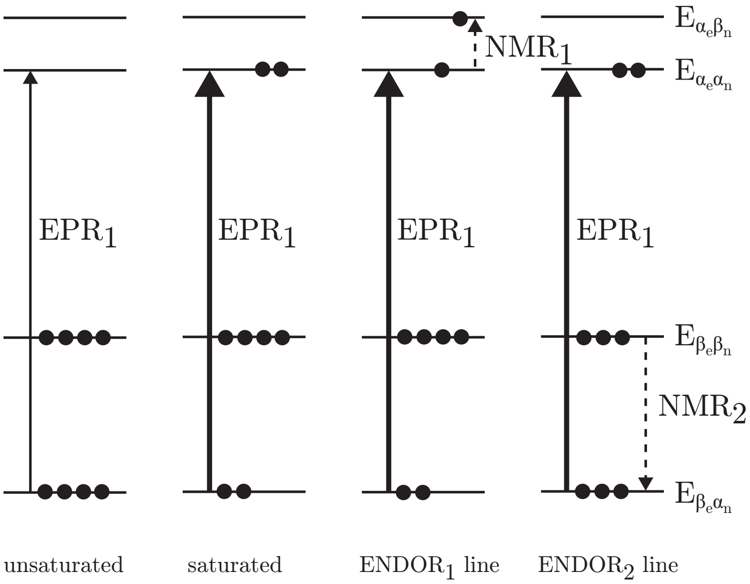

Figure 3.1: Energy scheme illustrating the ENDOR effect. Firstly, an EPR line is selected and secondly, it is saturated. Thirdly, radiofrequency is applied resulting in a saturation of NMR transitions and desaturation of the EPR transition giving rise to two ENDOR lines for a system with $S = 1/2$ and $I = 1/2$. [28]

Due to the so called "quantum transformation" from low frequency (which is used to irradiate) to high frequency (which is used to detect), the signal intensity is enhanced by a factor of up to 10^5 in the ENDOR experiment compared to a simple NMR experiment. [40, 41]

3.1.1 The Steady-State ENDOR Effect

In order to obtain a continuous ENDOR signal, relaxation pathways have to enable a returning to the initial configuration. Based on what was shown in the chapter on EPR in section 2.1.3, electron spin-lattice relaxation (W_e as shown in figure 3.2) enables "hot spins" to fall from $E_{\alpha_e\beta_n}$ back to $E_{\beta_e\beta_n}$. However, with the high microwave intensity applied in an ENDOR experiment, this process cannot compete with the induced absorption. [41]

Another possible relaxation pathway for the "hot spins" to return is the following: from $E_{\alpha_e\beta_n}$ to $E_{\alpha_e\alpha_n}$ *via* nuclear spin-lattice relaxation W_{n_I}, then from $E_{\alpha_e\alpha_n}$ to $E_{\beta_e\alpha_n}$ *via* W_{e_I} and then back to $E_{\beta_e\beta_n}$ *via* W_{n_II}.
This route is also known as the bypass-route. The nuclear spin-lattice relaxation is usually very weak compared to its electron counterpart and causes a so-called "bottleneck" in the relaxation pathway. However, as an intense

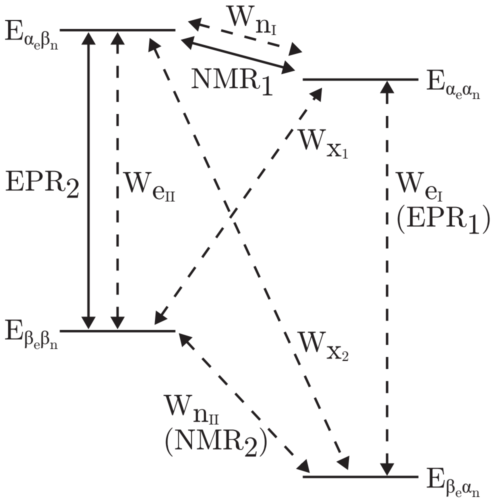

Figure 3.2: Energy scheme illustrating the relaxation pathways responsible for the steady-state ENDOR effect. Solid lines show irradiated induced transitions whereas dotted lines represent relaxation pathways. W_e and W_n are the electron and nuclear spin-lattice relaxation, respectively, whereas W_x stands for the cross-relaxation processes for electron and nuclear transitions occurring simultaneously. [40]

radiofrequency is applied in the ENDOR experiment which saturates the NMR transition, the nuclear spin-lattice relaxation is short-circuited. The efficiency of the relaxation pathway described above is thus improved. This is called the steady-state ENDOR effect. [41]

3.2 The ENDOR Spectrum

The ENDOR spectrum of one nucleus with spin $I = 1/2$ or one set of equivalent nuclei with spin $I = 1/2$ consists of two lines centered about ν_n and separated by A (in the case of $A/2 < \nu_n$).[*]

The main advantages of ENDOR spectra are the resolution enhancement (compared to EPR) and sensitivity enhancement (compared to NMR), especially for organic radicals in solution.

While the number of lines grow multiplicatively in EPR, it grows only additively in ENDOR. Given *e.g.* the triphenylmethyl radical, the EPR spec-

---

[*] For the opposite case of $A/2 > \nu_n$, the lines are centered about $A/2$ and separated by $2\nu_n$. This case, however, is rare for protons in organic π radicals. [28]

trum is expected to consist of 196 lines (due to one set of three equivalent protons and two sets of six equivalent protons, which makes $4 * 7 * 7 = 196$). As additional selection rules are introduced in ENDOR spectroscopy, an ENDOR spectrum consists of two lines for each set of equivalent nuclei. This makes a total of only six lines for the triphenylmethyl radical, whereas the distance between two lines of a pair is the hyperfine coupling constant in MHz. As the lines are centered about the Larmor frequency, even the interacting nucleus can be identified. The only drawback of ENDOR in this context is that it does not give any information on the number of interacting nuclei. [39]

However, the tremendous decrease in the number of lines makes the ENDOR spectrum much better resolved than the corresponding EPR spectrum. Compared to a conventional NMR spectrum of a radical, the detection of the NMR resonances in the microwave region leads to a sensitivity enhancement (due to “quantum transformation” as elucidated in section 3.1). [40]

Chapter 4

Paramagnetic Organic Species

Radicals are paramagnetic species whose molecular symmetry and electron distribution can be revealed by means of EPR spectroscopy. [33]
Paramagnetic organic species can be classified into neutral radicals and charged radicals: radical anions and radical cations. As a radical does not necessarily possess only one unpaired electron, biradicals will be addressed later in this chapter.

4.1 Neutral Radicals

For a neutral radical to be generated, a covalent bond must be cleaved homolytically. In order to cleave a C−C or C−H bond, respectively, dissociation energies of 300 to 400 $^{\mathrm{kJ}}/_{\mathrm{mol}}$ have to be overcome. This is usually effected by irradiation with a van de Graaf accelerator. An alternative is to replace the strong C−C or C−H bonds by weaker C−I bonds or peroxides, which are then in turn easier to cleave. [28, 33]

$$A{-}B \xrightarrow[\Delta]{h\nu} \mathrm{A}^{\bullet} + {}^{\bullet}\mathrm{B}$$

As an even simpler alternative, reactive radical precursors such as di(*t*-butyl)peroxide or $\mathrm{OH}^{\bullet}$ react with the precursor molecule, abstract an H atom and thus lead to the formation of a radical. [28]

Oxidizing an anion, with O_2, or reducing a cation, with Zn powder or electrolytically, are two alternative ways to generate neutral radicals. [33]

$$X^{\ominus} \xrightarrow{-e^{\ominus}} X^{\bullet} \qquad \text{oxidation}$$

$$X^{\oplus} \xrightarrow{+e^{\ominus}} X^{\bullet} \qquad \text{reduction}$$

At this point, two prominent examples of neutral radicals shall be given: the radical of 2,2-diphenyl-1-picrylhydrazyl (DPPH$^{\bullet}$) is used as a reference in EPR for the relative determination of g factors [42, 43, 44] and the nitroxyl radical 2,2,6,6-tetramethyl-4-oxopiperidinyl-1-oxyl (TEMPO$^{\bullet}$) is used as spin trap to scavenge short-lived radicals [45, 46].

4.2 Radical Anions

When a neutral diamagnetic molecule takes up an electron – is reduced – a radical anion is born. Radical anions are in general very reactive, which is the reason why they have to be generated and handled with great care. Oxygen as well as air moisture have to be excluded unconditionally by working under high vacuum. This implies that the solvents used have to be pure and water-free to the highest possible extent.

4.2.1 Generation of Radical Anions

Suitable solvents for the generation of radical anions are dimethoxyethane (DME), tetrahydrofuran (THF), 2-methyltetrahydrofuran (MTHF) as well as *N,N,N',N',N",N"*-hexamethylphosphoric triamide (HMPT). As radical anions are extremely sensitive against protic impurities, great attention has to be paid to their purification. [33]

In order to reduce the sample molecule to its radical anion, alkali metals *e.g.* Li, Na, K, Rb and Cs are used as reducing agents. In fact, the alkaline earth metals Ca, Sr and Ba are supposed to be suitable reducing agents as well. However, this has not proven experimentally. A possible explanation for this behavior may lie in the “nature of the reduction process”. [47]

A small piece of the metal is sublimated to its metallic mirror under high vacuum. The reduction process is then happening *via* valence electron transfer of the metal to the LUMO of the sample molecule, yielding an anion with one unpaired electron. However, the solvent plays an important role in the effectiveness of the electron transfer process [47]. Some cases are reported where alloys of Na and K in THF/DME mixtures showed the most promising results [48, 49]. Furthermore, mixtures of di(t-butyl)peroxide and KOH are known to promote the formation of aliphatic ketyl radical anions [50]. Irradiating the sample simultaneously to the reduction enhances its effectiveness [28].

$$\begin{aligned} \mathrm{K} + \mathrm{solv} &\xrightarrow{h\nu} \mathrm{K}^{\oplus} + \mathrm{e}^{\ominus}_{\mathrm{solv}} \\ \mathrm{R} + \mathrm{e}^{\ominus}_{\mathrm{solv}} &\longrightarrow \mathrm{R}^{\bullet\ominus} + \mathrm{solv} \end{aligned}$$

The radical anion $\mathrm{R}^{\bullet\ominus}$ might then react further to its diamagnetic dianion $\mathrm{R}^{2\ominus}$ or triplet dianion $\mathrm{R}^{\bullet\bullet 2\ominus}$, respectively. These states may then even react further to trianions $\mathrm{R}^{\bullet 3\ominus}$. [28, 51]

$$\begin{aligned} \mathrm{R}^{\bullet\ominus} + \mathrm{K} &\rightleftharpoons \mathrm{R}^{2\ominus}(\mathrm{R}^{\bullet\bullet 2\ominus}) + \mathrm{K}^{\oplus} \\ \mathrm{R}^{2\ominus}(\mathrm{R}^{\bullet\bullet 2\ominus}) + \mathrm{K} &\rightleftharpoons \mathrm{R}^{\bullet 3\ominus} + \mathrm{K}^{\oplus} \end{aligned}$$

Ion Pair Formation

The generated radical anion may form a contact ion pair with its counterion, the metal cation. This ion pair can be tight (contact ion pair) or loose (solvent-separated ion pair), dependent on how strong their interaction is. The factors determining the strength of this interaction:

- The electronic structure of the radical ion. Hard bases favor hard acids, *i.e.* radical ions with lone pairs on heteroatoms favor $\mathrm{Li}^{\oplus}$. Soft bases favor soft acids, *i.e.* radical ions with lone pairs on carbon favor $\mathrm{K}^{\oplus}$. [28]

- The concentration of the metal. The higher the concentration of each, the radical anion and the metal cation, or both, increases the chance for ion pairing. [28]

- The cation-solvating power of the solvent. Although maybe expected, the cation-solvating power of a solvent cannot be deduced from its dielectric constant. Ion pair formation is fostered, which means the cation-solvating power decreases, in the sequence HMPT, DME, THF, MTHF, DEE. For example, sodium naphthalene is present as a free radical in DME, whereas it is present as ion pair in THF [47]. Higher temperature *ceteris paribus* also favors ion pairing. [52]

- The size of the alkali metal cation. Appropriate geometric conditions being met, the formation of ion pairs depends on the size of the counterion. Ion pairs are more likely to be formed if the size of the counterion “fits” the geometry of the radical anion. [53, 54]

The radical anion–countercation interaction influences structure and stability of the radical anion [53] as a perturbation in the environment of the radical anion may result in changes of hyperfine splittings and g factors [52]. This interaction can be visible in EPR, as the metals used for reduction posses magnetic nuclei (compare table 2.1, for *e.g.* K it is $I = 3/2$).

4.3 Radical Cations

When an electron is abstracted from a neutral diamagnetic molecule – when the molecule is oxidized – a radical cation is born.

In the past, radical cations used to be generated *via* oxidation in sulfuric acid. Nowadays, several methods exist but there is no universal method for the generation of radical cations. A look at ionization energies and electrode potentials give a hint for finding a suitable method, but usually one has to rely on experience data with structurally related molecules. [55]
One of the major tasks is to find a method which gives persistent radical cations and allows for the prevention of back-electron transfer* from the reduced oxidant to the radical cation. [56]

Counterion effects do not only have to be taken into account for radical anions, but play as well a role for radical cations. One of the rare examples for radical cation–counteranion interactions is given by Gescheidt and coworkers [57] in the case of 9,9’-bianthryl whose radical cation spectra differ depending on counterion, solvent and temperature.

4.3.1 Generation of Radical Cations

In a review about methods for the generation of radical cations, Davies groups the methods in oxidizing metals, Lewis acids, protic acids, stable radicals,

---

* For the generation of radical anions, back-electron transfer is easily suppressed as the reductant (= the alkali metal) is turned from its free radical atomic state to a closed-shell alkali metal cation.

onium salts, halogens, quinones, nitro compounds, anionic oxidation, electromagnetic radiation, γ-irradiation, X-irradiation, electron irradiation and zeolithes. [55]

Out of the large pool of possible oxidizing agents, those of relevance to this work shall be presented at this point.

- $AlCl_3$ in CH_2Cl_2. While the oxidation potential of the system is known ($E_{ox} = +1.6\,V$ *vs.* SCE), the oxidation mechanism of $AlCl_3$ in CH_2Cl_2 is still uncertain. However, $AlCl_3$ in CH_2Cl_2 is a popular system and allows for the selective generation of radical cations with heteroatoms. [58]

- “Magic Blue”. Its high oxidizing power makes “Magic Blue” (= tris-(*p*-bromophenyl)ammoniumyl hexachloroantimonate) a very strong and wide-spread one-electron oxidizing agent for organic molecules. While the perchlorate salt is as well known for its oxidizing effect, the hexachloroantimonate salt is more stable against thermal and photochemical decomposition. [59]

- PIFA in HFP. Phenyliodine(III) bistrifluoroacetate in 1,1,1,3,3,3-hexafluoro-2-propanole is another strong oxidizing agent for organic molecules. However, PIFA is not a suitable oxidant for molecules that give unstable radicals. PIFA is therefore regarded as a convenient replacement for the highly toxic thallium tris(trifluoro)acetate in the generation of radicals of intermediate reactivity [60]. As an alternative, trifluororacetic acid (TFA) can be added to the solvent or used as a solvent itself, as its low freezing point allows for spectra recording at lower temperatures. However, compared to TFA as solvent, HFP promotes the generation of more persistent radicals, although it is actually a weaker acid and more nucleophilic. [61, 62]

- DDQ in HFP. 2,3-Dichloro-4,5-dicyanobenzoquinone serves as oxidant up to 1.6 V. An enforcement of the oxidation by means of UV light, however, promotes the generation of the DDQ anion which then masks the spectrum of the cation [62]. Under acid conditions, the DDQ anion is rapidly protonated and back-electron transfer thus inhibited. [56]

- Thallium tris(trifluoroacetate) [63] and $AgClO_4$ [33]. Thallium(III) and $AgClO_4$ are still wide-spread oxidants, although they are more and more replaced by substances that are easier and safer to handle.

4.4 Biradicals

A biradical is a two spin state system, *i.e.* a molecule with two unpaired electrons each in one orbital. If the two orbitals which accommodate the unpaired electrons are sterically separated from each other and do not interact, the biradical behaves like a double monoradical. This means that the spectrum of this biradical looks exactly like the spectrum of the monoradicals. One unpaired electron gives rise to a doublet (spin multiplicity $2S + 1 = 2$) and in case of a symmetric biradical, the doublet has twofold intensity. [32]

However, if the two unpaired electrons interact with each other, they can give rise to

- a singlet (spin multiplicity $2S + 1 = 1$ for $S = 1/2 - 1/2 = 0$) or
- a triplet (spin multiplicity $2S + 1 = 3$ for $S = 1/2 + 1/2 = 1$).

According to Hund's rule, the triplet is usually more stable. The energy difference between singlet and triplet is characterized by the exchange integral J. [28]

Similar to the interaction of the electron spin with the nuclear spin that has been discussed in chapter 2, the two electron spins interact as well, giving rise to a dipolar interaction $\vec{S_1} \cdot D \cdot \vec{S_2}$, where D is the zero-field splitting (ZFS) tensor. It describes the fine splitting of triplet EPR spectra which is observable without presence of a magnetic field. [28]
The principal values of D, namely D_{XX}, D_{YY}, D_{ZZ} describe the principal axes frame X, Y, Z. As the sum of these principal values is zero, it shall be split into two ZFS parameters: D and E, whereas

$$D = -3/2 D_{ZZ} \qquad \text{with} \qquad D' = \frac{D}{g_e|\mu_B|} \tag{4.1}$$

$$\text{and} \qquad E = 1/2(D_{YY} - D_{XX}) \qquad \text{with} \qquad E' = \frac{E}{g_e|\mu_B|} \tag{4.2}$$

The units of D and E, respectively, is cm^{-1} (wavenumbers) and of D' and E', respectively, is T (magnetic field strength). D allows for an estimation of the mean distance r between the triplet electrons ($|D'| = 2.78 * 10^9 \text{ r}^{-3}$) [28, 64] and provides information on changes in spin densities at the site of the radicals [65, 66]. E contains information about axial symmetry as it is zero for $D_{XX} = D_{YY}$ [29].

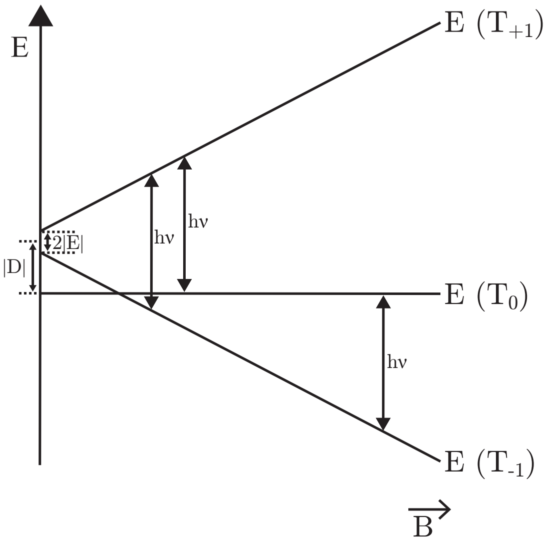

Figure 4.1: Zero-field and Zeeman splittings for a triplet state as a function of the magnetic field strength showing three transitions of equal energy $h\nu$: two are allowed as they obey the EPR selection rules and one is forbidden as it does not obey the EPR selection rules. [28]

Figure 4.1 shows three transitions of constant energy $h\nu$: The two allowed transitions occur at large magnetic fields and obey the EPR selection rule of $\Delta m_S = \pm 1$. The forbidden transition is a $\Delta m_S = \pm 2$ transition and occurs at half-field. [67]

It is important to note that triplet spectra are usually not observable in liquids as the large dipolar interaction between two close spins (large D) is not averaged out by the Brownian motion. Observing EPR spectra of triplets requires either single crystals or rigid glassy matrices, *e.g.* frozen solutions in MTHF. [28, 68]

4.5 Higher Spin States

Higher spin states are of interest for studies on “organic magnets” [51]. Reports on quartet spin multiplicity [69, 70, 71], quintet spin multiplicity [72], septet spin multiplicity [72, 73, 74], nonet spin multiplicity [75, 76] and even molecules with spin multiplicities of up to 11 [77] exist in literature. High multiplicities are often achieved with molecules containing transition-metal ions [78].

Part II

Experiments

Chapter 5

Quenching Experiments with 3-(Carboxymethyl)-lumiflavin

Lumiflavin, being a photodegradation product of riboflavin, oxidizes food components under light-illumination [79, 80]. Flavins in general are known to be photoreduced by amino acids and as the reactive species of flavins is their triplet state, this photoreduction occurs through their triplet state. Some aromatic amino acids inhibit photoreduction *via* quenching of the flavin triplet. This happens by means of a one-electron transfer between the amino acids and the flavin triplet. [81, 82]
However, the complex response of flavins toward irradiation strongly depends on the pH value.

The work presented here is explicitly dedicated to study the quenching behavior of 3-(carboxymethyl)-lumiflavin, a lumiflavin derivative, with four different amino acids (DL-cysteine, DL-histidine, DL-methionine and DL-tryptophan) in buffered aqueous solution at pH 7. Therefore, steady-state and time-resolved fluorescence techniques were applied and bimolecular quenching rate constants as well as electron transfer rate constants were determined. While *e.g.* melanin does not quench the fluorescence of flavin derivatives, although it complexes with them [83], quenching effects could be observed with the amino acids investigated. The results presented here supplement those on quenching experiments with riboflavin [84, 85, 86], known as vitamin B2, presented in [87] within the scope of an INTAS project entitled "A spin chemistry investigation on short-lived intermediates of biologically important molecules".

In order to study the photochemical reactions of 3-(carboxymethyl)-lumiflavin with various amino acids, Kaptein made use of the technique of

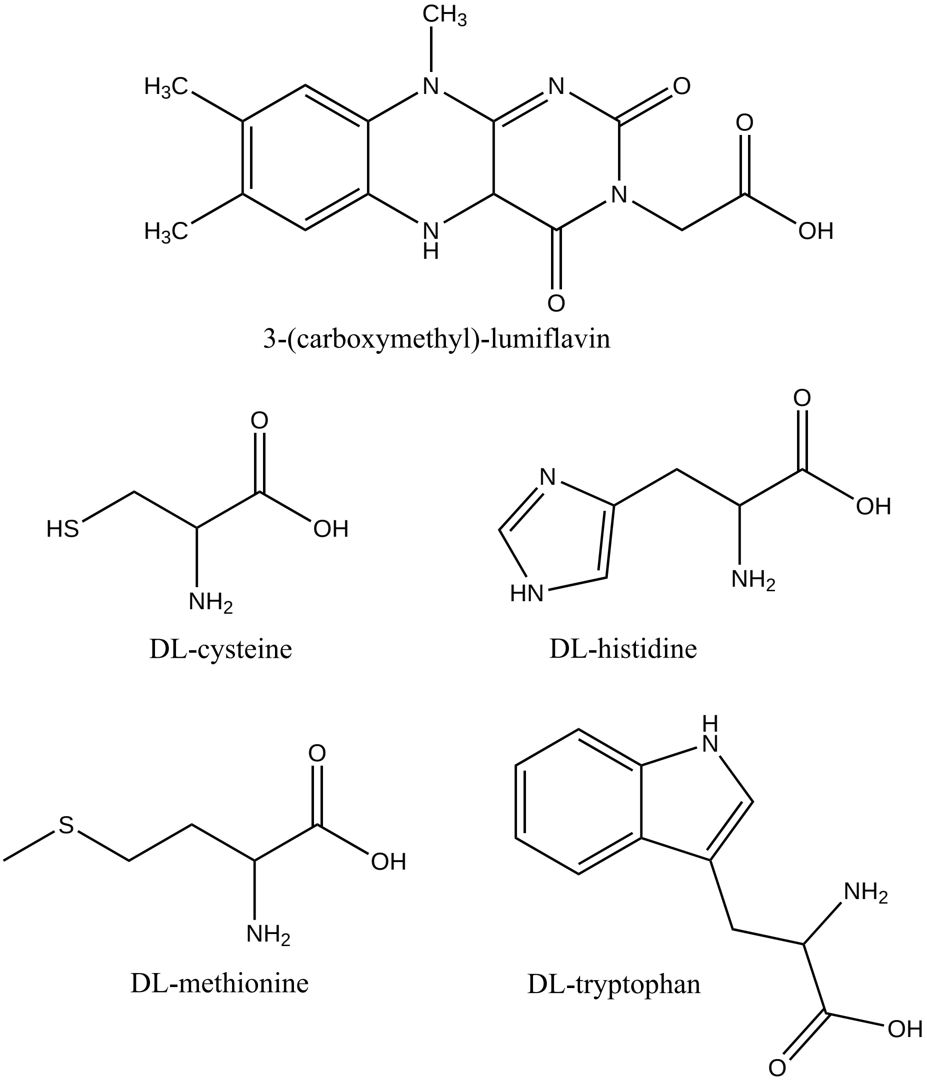

3-(carboxymethyl)-lumiflavin

DL-cysteine

DL-histidine

DL-methionine

DL-tryptophan

Figure 5.1: Molecular structures of 3-(carboxymethyl)-lumiflavin, DL-cysteine, DL-histidine, DL-methionine and DL-tryptophan.

CIDNP and found that a disproportionation reaction of the flavin radical is the reason for the partial cancellation of the CIDNP signal. [88, 89, 90]

5.1 Experimental

The sample, an orange powder, was supplied by the working group of Prof. Dr. Vieth from the Free University of Berlin.
DL-cysteine (Fluka, $\geq$ 95 %), DL-histidine (Fluka, $\geq$ 99.0 %) and DL-methionine (Fluka, $\geq$ 99.0 %) were used as received. DL-tryptophan (Fluka, $\geq$ 99 %) was recrystallized from water.
For performing the measurements, 3-(carboxymethyl)-lumiflavin was dissolved in Na_2HPO_4/KH_2PO_4 buffer pH 7 (Fluka, $\geq$ 99 %) as described in [87]. Oxygen was removed from all samples by bubbling with argon for 10 minutes.

Absorption spectra were recorded on a Shimadzu UV-3101 PC double-beam spectrometer using slit widths of 2 nm. Emission spectra were recorded on a FluoroMax-2 ISA®Jobin YVON-SPEX Instruments Spectrometer allowing for temperature control from 15 to 60 °C.
For time-resolved fluorescence spectroscopy, modulation technique with digital storage oscilloscope was used in the case of pure 3-(carboxymethyl)-lumiflavin and for the quenching experiments, time-correlated single-photon counting was applied. A 400 nm LED with an UG 5 excitation filter (Schott) and a GG 495 nm long pass emission filter (Schott) were used. The setup of these apparatuses was similar to the one described in [91].

5.2 Spectra of 3-(Carboxymethyl)-lumiflavin

The absorption spectrum of 3-(carboxymethyl)-lumiflavin in buffered aqueous solution at pH 7 shows major absorption bands in the UV-Vis region, namely at 223 nm, 270 nm, 370 nm and 444 nm, respectively (*cf.* figure 5.2). Excitation at 370 nm and 444 nm, respectively, gave identical emission spectra with one broad band at 520 nm. The emission spectrum, corrected according to manufacturer specifications, is shown in figure 5.3. Excitation spectra recorded at the wavelength of maximum emission agree well with the absorption spectrum.

The data published for the related 3-methyl-lumiflavin in water at pH 6 exhibit as well the characteristic absorption bands at 364 nm and 444 nm [92].

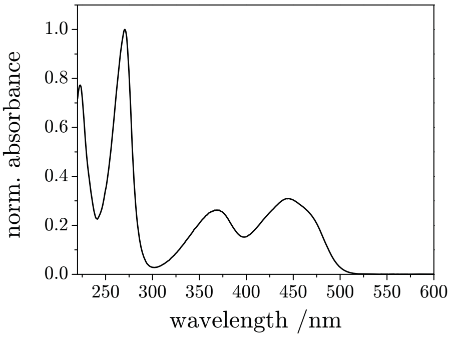

Figure 5.2: Absorption spectrum of 3-(carboxymethyl)-lumiflavin in phosphate buffer at pH 7.

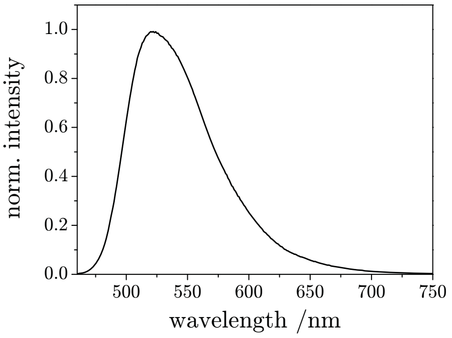

Figure 5.3: Emission spectrum of 3-(carboxymethyl)-lumiflavin in phosphate buffer at pH 7.

These data are also comparable to those of the ethyl-substituted derivative, 3-ethyl-lumiflavin [93], and the benzyl-substituted derivative, 3-benzyl-lumiflavin [94]. A comparison of the data with those of the parent molecule lumiflavin shows that the substitution in position 3 does not evoke major changes in the photophysical properties of the molecule. The two major absorption bands of lumiflavin in water at pH 6 are reported to appear at 367 nm and 445 nm, respectively, and the emission band at 530 nm and are thus in good agreement to the spectra of 3-(carboxymethyl)-lumiflavin. [92]

A monoexponential excited-state lifetime of 3-(carboxymethyl)-lumiflavin of 4.8 ns was determined using modulation technique with digital storage oscilloscope. Lifetimes in this range as well as relatively high quantum yields are characteristic for isoalloxazine derivatives, such as lumiflavin. [95, 96, 97]

5.3 Quenching Experiments

The fluorescence of 3-(carboxymethyl)-lumiflavin was quenched in four different experiments, using the amino acids DL-cysteine, DL-histidine, DL-methionine and DL-tryptophan as quenchers. The solvent for all experiments was aqueous Na_2HPO_4/KH_2PO_4 buffer pH 7.

The Stern-Volmer relation describes the quenching behavior for a monoexponential decay following a δ-pulse excitation [98]:

$$\frac{I_0}{I} = \frac{\tau_0}{\tau} = 1 + k_q\tau_0[Q] = 1 + K_{\mathrm{SV}}[Q] \tag{5.1}$$

with I_0 and I being the steady-state fluorescence intensity and τ_0 and τ being the lifetime of the fluorophore in s in the absence and in the presence of a quencher, respectively, k_q being the experimental bimolecular quenching rate constant in $^{\mathrm{m}^3}\!/_{\mathrm{mol\,s}}$, $[Q]$ being the concentration of the quencher in $^{\mathrm{mol}}\!/_{\mathrm{m}^3}$ and K_{SV} being the Stern-Volmer constant in $^{\mathrm{m}^3}\!/_{\mathrm{mol}}$.
$I_0/I = \tau_0/\tau$ is not valid for static quenching. Thus the way the equation is given above only holds for dynamic quenching. [87, 99]

Figures 5.4, 5.5, 5.6 and 5.7 show the Stern-Volmer plots for both, steady-state and time-resolved experiments: I_0/I, or τ_0/τ is plotted *vs.* the quencher concentration yielding an intercept on the ordinate of 1 and a slope equal to the Stern-Volmer constant. The Stern-Volmer constants and bimolecular quenching rate constants are summarized in table 5.1. A more detailed overview of the experimental data can be found in tables 5.4, 5.5, 5.6 and 5.7 in section 5.5.

For cysteine, the Stern-Volmer constant is comparable for steady-state ($K_{\mathrm{SV}}^{ss} = 3.65\,^{1}\!/_{\mathrm{mol}}$) and time-resolved measurements ($K_{\mathrm{SV}}^{tr} = 2.53\,^{1}\!/_{\mathrm{mol}}$). Therefore, it can be deduced that the quenching process of 3-(carboxymethyl)-lumiflavin with cysteine follows dynamic behavior.
The Stern-Volmer constants obtained for histidine ($K_{\mathrm{SV}}^{ss} = 14.9\,^{1}\!/_{\mathrm{mol}}$ and $K_{\mathrm{SV}}^{tr} = 9.74\,^{1}\!/_{\mathrm{mol}}$) and methionine ($K_{\mathrm{SV}}^{ss} = 18.5\,^{1}\!/_{\mathrm{mol}}$ and $K_{\mathrm{SV}}^{tr} = 14.1\,^{1}\!/_{\mathrm{mol}}$), respectively, are in the same order of magnitude compared to those of the quenching process of riboflavin. [87]
Similar to the quenching reaction of tryptophan with riboflavin [87], the slope of the time-resolved Stern-Volmer plot ($K_{\mathrm{SV}}^{tr} = 2.15\,^{1}\!/_{\mathrm{mol}}$) is much smaller than the slope of the steady-state Stern-Volmer plot ($K_{\mathrm{SV}}^{ss} = 15.7\,^{1}\!/_{\mathrm{mol}}$). It is likely that simultaneous static and dynamic quenching is happening in this case. To make sure one would have to investigate higher quencher concentrations, but unfortunately tryptophan is only poorly soluble in aqueous buffer at pH 7. This is why a possible upward curvature toward the ordinate, which would be an indicator of simultaneous static and dynamic quenching cannot be made out in figure 5.7. However, ground-state complex formation is rather unlikely at low concentrations [100].

These results are in line with those reported on the reactivity of flavin derivatives toward quenching by amino acid side chains in proteins, studied by means of photo-CIDNP. These studies reveal that quenching by tryptophan is almost diffusion controlled, that quenching by histidine is slower and that quenching by methionine is almost negligible. However, quenching by methionine was found to be slow in the molecular systems investigated. The

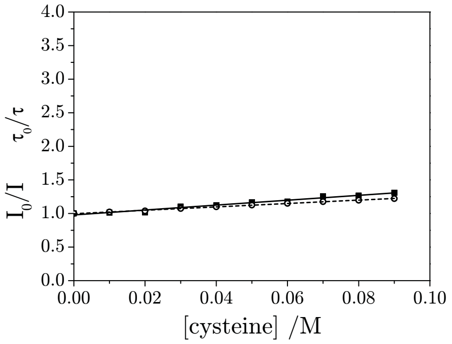

Figure 5.4: Stern-Volmer plot for cysteine as quencher of 3-(carboxymethyl)-lumiflavin in phosphate buffer at pH 7.

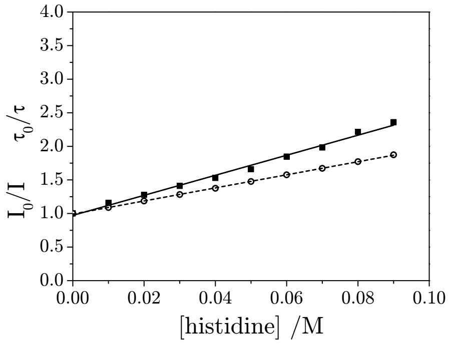

Figure 5.5: Stern-Volmer plot for histidine as quencher of 3-(carboxymethyl)-lumiflavin in phosphate buffer at pH 7.

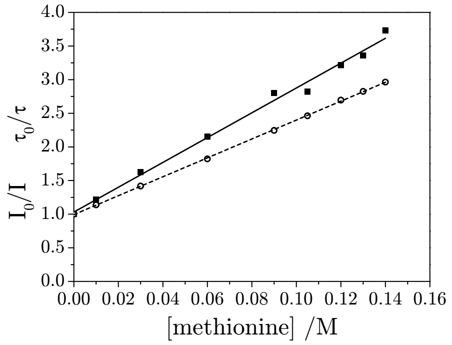

Figure 5.6: Stern-Volmer plot for methionine as quencher of 3-(carboxymethyl)-lumiflavin in phosphate buffer at pH 7.

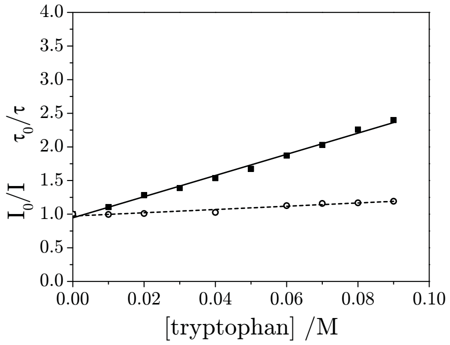

Figure 5.7: Stern-Volmer plot for tryptophan as quencher of 3-(carboxymethyl)-lumiflavin in phosphate buffer at pH 7.

Table 5.1: Stern-Volmer constants K_{SV} and bimolecular quenching rate constants k_q for the quenching reactions with the stated amino acids at pH 7.
"*ss*" stands for steady-state and "*tr*" for time-resolved measurement.

	K_{SV}^{ss} /$^{1}/_{\mathrm{mol}}$	k_q^{ss} /$^{1}/_{\mathrm{mol\ s}}$	K_{SV}^{tr} /$^{1}/_{\mathrm{mol}}$	k_q^{tr} /$^{1}/_{\mathrm{mol\ s}}$
cysteine	3.65	$7.71*10^8$	2.53	$5.35*10^8$
histidine	14.9	$3.17*10^9$	9.74	$2.07*10^9$
methionine	18.5	$4.01*10^9$	14.1	$3.05*10^9$
tryptophan	15.7	$3.55*10^9$	2.15	$4.84*10^8$

proposed quenching mechanism involves a flavin triplet state which is being quenched by amino acids in a diffusion controlled process. Static quenching can be ruled out. [101]

5.4 Summary of Rate Constants

Table 5.1 gives an overview of the Stern-Volmer constants and the bimolecular quenching rate constants obtained by both, steady-state and time-resolved measurements. Based on equation 5.1, k_q is obtained *via* division of K_{SV} by τ_0.

For calculating the association constant, knowledge of the molecules' radii is necessary. Therefore, the molecules were treated as ellipsoids and their radii estimated by using HyperChem 7.0. The approximate radius of 3-(carboxymethyl)-lumiflavin was determined to equal about 4.1 $\mathring{A}$. The radii of the quencher molecules were taken from [87] where they have been determined in a similar procedure: 3.04 $\mathring{A}$ for cysteine, 3.99 $\mathring{A}$ for histidine, 3.62 $\mathring{A}$ for methionine and 4.11 $\mathring{A}$ for tryptophan.

The association constant K_A in $^{\mathrm{m}^3}/_{\mathrm{mol}}$ is calculated by means of two approaches, namely the one by Eigen and Fuoss

$$K_A = \frac{4}{3}\pi N_A R_c^3 \exp\left(\frac{-W_r}{RT}\right) \tag{5.2}$$

and the Sutin approach

$$K_A = 4\pi N_A R_c^2 dR \exp\left(\frac{-W_r}{RT}\right) \tag{5.3}$$

Table 5.2: Association constants K_A and diffusional rate constants k_d. “E.F.” stands for the approach of Eigen-Fuoss and “N.S.” for Sutin’s approach. 3cmlf stands for 3-(carboxymethyl)-lumiflavin.

	$K_A^{E.F.}$ /$^{\mathrm{l}}/_{\mathrm{mol}}$	$K_A^{N.S.}$ /$^{\mathrm{l}}/_{\mathrm{mol}}$	k_d /$^{\mathrm{l}}/_{\mathrm{mol\,s}}$
3cmlf - cysteine	0.909	0.307	$6.63{*}10^9$
3cmlf - histidine	1.33	0.395	$6.49{*}10^9$
3cmlf - methionine	1.15	0.359	$6.51{*}10^9$
3cmlf - tryptophan	1.39	0.406	$6.49{*}10^9$

with the coulombic work term W_r in $^{\mathrm{J}}/_{\mathrm{mol}}$ given by

$$W_r = \frac{z_M z_Q e_0^2 N_A}{4R_c \pi \varepsilon_0 \varepsilon_S \left(1+\beta R_c \sqrt{I}\right)} \qquad \text{with} \qquad \beta = \sqrt{\frac{2N_A e_0^2}{1000\varepsilon_0 \varepsilon_S kT}} \tag{5.4}$$

where N_A is the Avogadro constant in mol^{-1}, R_c is the contact radius of the two molecules in m, dr is usually chosen as $8 * 10^{-11}$ m, R is the universal gas constant in $^{\mathrm{J}}/_{\mathrm{K\,mol}}$, T is the absolute temperature in K, z_M and z_Q are the charges of the fluorescent molecule and the quencher, respectively, e_0 is the elementary charge in C, ε_0 is the vacuum permittivity in $^{\mathrm{C}}/_{\mathrm{N\,m^2}}$, ε_S the dielectric constant of the solvent, I is the ionic strength in $^{\mathrm{mol}}/_{\mathrm{m^3}}$ and k is the Boltzmann constant in $^{\mathrm{J}}/_{\mathrm{K}}$ [102].

The diffusional rate constant k_d in $^{\mathrm{m^3}}/_{\mathrm{mol\,s}}$ was calculated using Debye-Smoluchowski equation in the following form:

$$k_d = \left(\frac{2RT}{3\eta}\right)(r_M + r_Q)\left(\frac{1}{r_M} + \frac{1}{r_Q}\right) \tag{5.5}$$

where η is the solvent viscosity at T in $^{\mathrm{kg}}/_{\mathrm{m\,s}}$ ($\eta_{\mathrm{H_2O},20^\circ\mathrm{C}} = 1.0019 * 10^{-3}\ ^{\mathrm{kg}}/_{\mathrm{m\,s}}$ [103]) and r_M and r_Q are the radii of the fluorescent molecule and the quencher, respectively, in m.

The electron transfer rate constant k_{ET} in s^{-1} was calculated by means of the following equation [104]:

$$\frac{1}{k_q} = \frac{1}{k_d} + \frac{1}{K_A k_{ET}} \tag{5.6}$$

Table 5.3 summarizes the electron transfer rate constants calculated using the bimolecular quenching rate constant obtained from both, steady-state

Table 5.3: Electron transfer rate constants k_{ET}.
"E.F." stands for the approach of Eigen-Fuoss and "N.S." for Sutin's approach. 3cmlf stands for 3-(carboxymethyl)-lumiflavin.

		$k_{ET}^{E.F.}$ /s^{-1}	$k_{ET}^{N.S.}$ /s^{-1}
steady-state	3cmlf - cysteine	$9.59*10^8$	$2.85*10^9$
	3cmlf - histidine	$4.67*10^9$	$1.57*10^{10}$
	3cmlf - methionine	$9.05*10^9$	$2.91*10^{10}$
	3cmlf - tryptophan	$5.65*10^9$	$1.93*10^{10}$
time-resolved	3cmlf - cysteine	$6.40*10^8$	$1.90*10^9$
	3cmlf - histidine	$2.29*10^9$	$7.70*10^9$
	3cmlf - methionine	$4.97*10^9$	$1.60*10^{10}$
	3cmlf - tryptophan	$3.77*10^8$	$1.29*10^9$

and time-resolved measurements. Two electron transfer rate constants are given for each reaction: One using Eigen-Fuoss' approach for the association constant and a second one using Sutin's approach. [102]

5.5 Supplementary Material on Experimental Data

Figures 5.8 and 5.9 show the absorption and emission spectra, respectively, of 3-(carboxymethyl)-lumiflavin in the presence of cysteine at pH 7, figures 5.10 and 5.11 for histidine, figures 5.12 and 5.13 for methionine and figures 5.14 and 5.15 for tryptophan. Tables 5.4, 5.5, 5.6 and 5.7 summarize the experimental data on each quenching experiment.

Due to quenching, the emission intensity decreases upon increasing the quencher concentration. However, in order to account for slightly alternating fluorophor concentrations in the quenching experiments, the absorbance of the fluorophor has to be taken into account. This yields a corrected emission intensity I_{corr}:

$$I_{\text{corr}} = \frac{1 - 10^{-\frac{A_{\text{corr}}}{2}}}{1 - 10^{-\frac{A_{0,\text{corr}}}{2}}} * \frac{I_0}{I} \tag{5.7}$$

where A_{corr} stands for the absorbance corrected by the baseline. The index "0" indicates the absence of a quencher.*

---

* No such correction has to be taken into account for the time-resolved measurements, as lifetime is not dependent on the concentration of the fluorophore within certain limits.

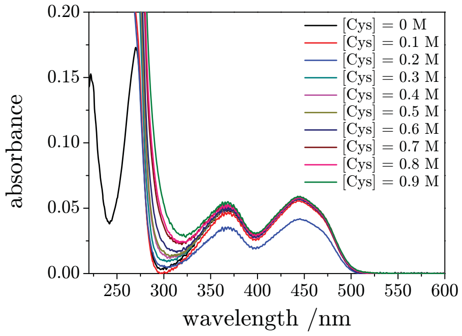

Figure 5.8: Absorption spectra of 3-(carboxymethyl)-lumiflavin in the presence of cysteine at pH 7.

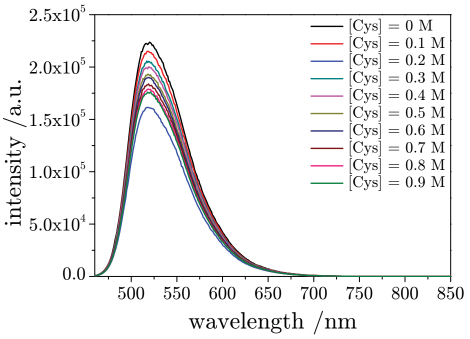

Figure 5.9: Emission spectra of 3-(carboxymethyl)-lumiflavin in the presence of cysteine at pH 7.

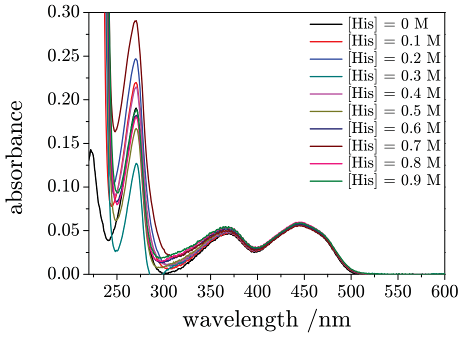

Figure 5.10: Absorption spectra of 3-(carboxymethyl)-lumiflavin in the presence of histidine at pH 7.

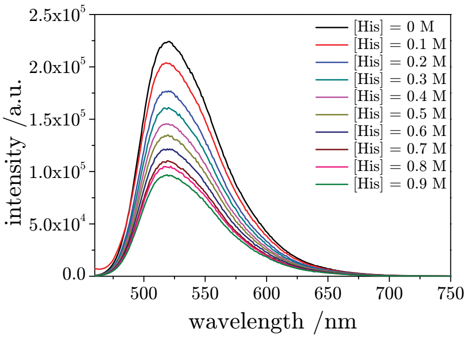

Figure 5.11: Emission spectra of 3-(carboxymethyl)-lumiflavin in the presence of histidine at pH 7.

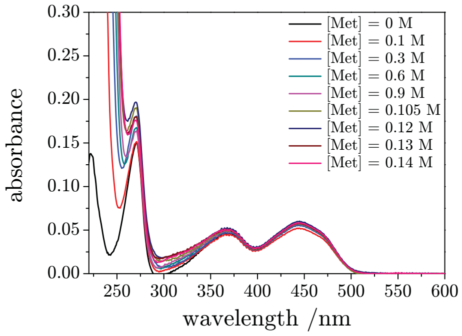

Figure 5.12: Absorption spectra of 3-(carboxymethyl)-lumiflavin in the presence of methionine at pH 7.

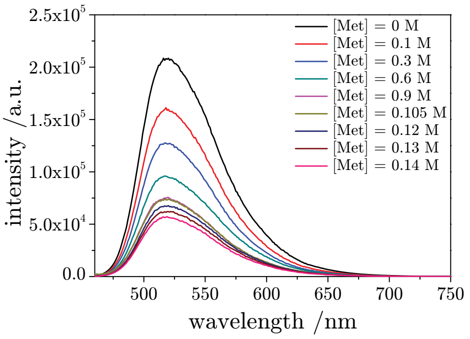

Figure 5.13: Emission spectra of 3-(carboxymethyl)-lumiflavin in the presence of methionine at pH 7.

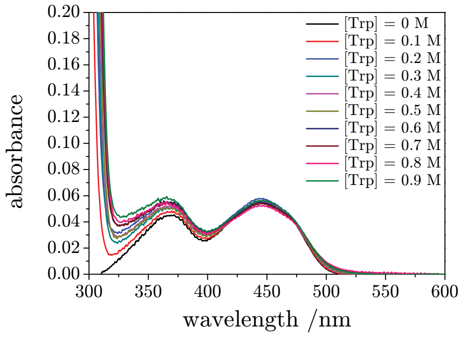

Figure 5.14: Absorption spectra of 3-(carboxymethyl)-lumiflavin in the presence of tryptophan at pH 7.

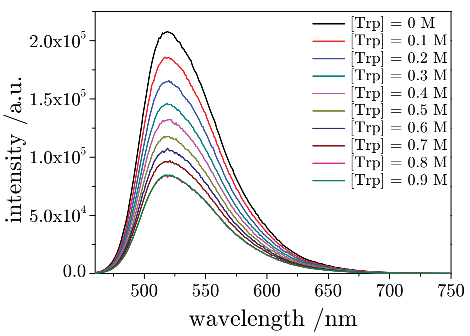

Figure 5.15: Emission spectra of 3-(carboxymethyl)-lumiflavin in the presence of tryptophan at pH 7.

Table 5.4: Data for the quenching experiments with cysteine at pH 7.
c stands for the concentration of the quencher in $^{\mathrm{mol}}/_{\mathrm{l}}$, $A_{444,\mathrm{corr}}$ stands for the mean corrected absorbance between 446 and 441 nm, I_{exp} stands for the experimentally determined intensity in arbitrary units, I_0 stands for the emission intensity in absence of a quencher, I_{corr} stands for the corrected emission intensity and τ_0 and τ stand for the excited-state lifetime in ns in the absence and presence of the quencher, respectively.

c /$^{\mathrm{mol}}/_{\mathrm{l}}$	$A_{444,\mathrm{corr}}$	I_{exp} /a.u.	(I_0/I_{corr})-1	τ /ns	$(\tau_0/\tau)-1$
0.00	0.0570	$1.750*10^7$	0.0000	4.73	0.000
0.01	0.0555	$1.679*10^7$	0.0143	4.62	0.023
0.02	0.0415	$1.264*10^7$	0.0159	4.55	0.039
0.03	0.0578	$1.606*10^7$	0.1034	4.40	0.074
0.04	0.0572	$1.566*10^7$	0.1213	4.30	0.100
0.05	0.0574	$1.511*10^7$	0.1654	4.20	0.125
0.06	0.0568	$1.479*10^7$	0.1779	4.11	0.151
0.07	0.0586	$1.433*10^7$	0.2546	4.02	0.177
0.08	0.0577	$1.396*10^7$	0.2676	3.95	0.198
0.09	0.0586	$1.373*10^7$	0.3092	3.87	0.222

Table 5.5: Data for the quenching experiments with histidine at pH 7. Caption as in table 5.4.

c /mol/l	$A_{444,corr}$	I_{exp} /a.u.	(I_0/I_{corr})-1	τ /ns	$(\tau_0/\tau)-1$
0.00	0.0562	$1.751*10^7$	0.0000	4.70	0.000
0.01	0.0565	$1.522*10^7$	0.1568	4.32	0.088
0.02	0.0566	$1.382*10^7$	0.2775	3.97	0.186
0.03	0.0568	$1.256*10^7$	0.4094	3.67	0.282
0.04	0.0566	$1.141*10^7$	0.5279	3.42	0.375
0.05	0.0568	$1.049*10^7$	0.6595	3.19	0.476
0.06	0.0572	$9.484*10^6$	0.8470	2.98	0.576
0.07	0.0554	$8.515*10^6$	0.9817	2.81	0.672
0.08	0.0594	$8.120*10^6$	1.2157	2.65	0.772
0.09	0.0585	$7.515*10^6$	1.3600	2.51	0.875

Table 5.6: Data for the quenching experiments with methionine at pH 7. Caption as in table 5.4.

c /mol/l	$A_{444,corr}$	I_{exp} /a.u.	(I_0/I_{corr})-1	τ /ns	$(\tau_0/\tau)-1$
0.00	0.0564	$1.647*10^7$	0.0000	4.60	0.000
0.01	0.0518	$1.250*10^6$	0.2156	4.05	0.138
0.03	0.0551	$9.922*10^6$	0.6250	3.25	0.418
0.06	0.0563	$7.620*10^6$	1.1510	2.53	0.822
0.09	0.0567	$5.842*10^6$	1.8011	2.05	1.246
0.105	0.0572	$5.839*10^6$	1.8199	1.87	1.463
0.12	0.0598	$5.336*10^6$	2.2140	1.71	1.695
0.13	0.0575	$4.902*10^6$	2.3598	1.63	1.826
0.14	0.0581	$4.448*10^6$	2.7333	1.55	1.963

Table 5.7: Data for the quenching experiments with tryptophan at pH 7. Caption as in table 5.4.

c /mol/l	$A_{444,corr}$	I_{exp} /a.u.	(I_0/I_{corr})-1	τ /ns	$(\tau_0/\tau) - 1$
0.00	0.0559	$1.628*10^7$	0.0000	4.43	0.000
0.01	0.0557	$1.469*10^7$	0.1049	-	-
0.02	0.0576	$1.304*10^7$	0.2806	-	-
0.03	0.0549	$1.152*10^7$	0.3877	-	-
0.04	0.0555	$1.044*10^7$	0.5354	-	-
0.05	0.0541	$9.305*10^6$	0.6740	-	-
0.06	0.0548	$8.391*10^6$	0.8712	3.93	0.127
0.07	0.0538	$7.622*10^6$	1.0299	3.82	0.159
0.08	0.0521	$6.654*10^6$	1.2559	3.79	0.169
0.09	0.0560	$6.681*10^6$	1.3986	3.72	0.192

Chapter 6

Photophysics of an Intramolecular Pyrene Excimer

Pyrene is well known – apart from its monomeric emission – for a concentration dependent red-shifted broad and unstructured emission attributed to its “excited dimer” or “excimer” [105]. Among other molecules allowing efficient charge-transfer via π–π stacking, pyrene-based molecules belong to the group of organic conjugated compounds [106] which play an important role in optoelectronics with applications as organic light-emitting diodes (OLEDs) [107], organic field-effect transistors (OFETs) [108] and organic photovoltaic cells (OPVs) [109].

In the present study, the photophysics of a compound consisting of a molecular hinge with two pyrenylethynyl moieties linked to the principal axis (for molecular structure see figure 6.2) was investigated in terms of monomer and excimer derived properties.*

An introduction on pyrene excimers as exemplification of the general concept of excimers shall be given before going into experimental details and results.

6.1 Introduction to Pyrene Excimers

A diluted solution of pyrene gives a structured emission band in the violet region (at about 27,000 cm^{-1} or 370 nm) originating from pyrene in its first

---

* This project was performed in close collaboration with Dr. A. Rosspeintner, formerly Graz University of Technology, now University of Geneva. [110]

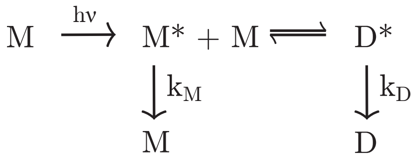

Figure 6.1: Birks' scheme of the kinetics of excimer formation [111].

excited state (^{1}M*).

$$^1\mathrm{M}^* \longrightarrow {}^1\mathrm{M} + h\nu_\mathrm{M}$$

The higher the concentration of pyrene, the more the intensity of the structured band decreases while a structureless band in the blue region appears. The structureless band at lower energies originates from an excited dimer (^{1}D*) which is formed by a collision of excited monomers (^{1}M*) with unexcited monomers (^{1}M): [105, 111]

$$\begin{aligned} {}^1\mathrm{M}^* + {}^1\mathrm{M} &\rightleftharpoons {}^1\mathrm{D}^* \\ {}^1\mathrm{D}^* &\longrightarrow {}^1\mathrm{M} + {}^1\mathrm{M} + h\nu_\mathrm{D} \end{aligned}$$

Förster and Kasper were the first who reported on a structureless emission band in the blue region upon increasing the concentration of pyrene in a solution [112]. The term "excimer" was originally proposed by Stevens and Hutton [113]. It is important to distinguish excimers from normal dimers in the excited states, as excimers are dissociated in the ground state. Excimers do not exist as dimers in the ground state.

Birks extended the definition given by Stevens and Hutton, made it valid as well for intramolecular excimers and defined an excimer as "a molecular dimer or stoichiometric complex which is associated in an excited electronic state and which is dissociative (*i.e.* would dissociate in the absence of external restraints) in its ground electronic state". [114]

A molecule with two aromatic moieties which are separated by an aliphatic chain, can form an intramolecular excimer if the excited moiety (^{1}M*) manages to approach the unexcited moiety (^{1}M) within its excited-state lifetime. Similar to the case described above, an intramolecular excimer (^{1}D*) is formed. [111]

The general scheme proposed by Birks [111] (see figure 6.1) holds for inter- and intramolecular excimer formation. It predicts double-exponential

decay with identical values for the time-constants of the monomer and the excimer. [115]
However, some authors claim that the scheme is different for intramolecular excimers [116, 117]. Three-exponential decays have been observed as well and were ascribed to structurally different conformers of the exciplex [118, 119], *e.g.* full and partial ring overlap [120]. Furthermore, much influence is ascribed to the length and flexibility of the chain linking the two pyrene moieties [121] and the presence of other bulky substituents [122].
Some cases are reported where the ground-state dimer as well as excimers exist, resulting in a change of the kinetics because diffusion of the excited and the unexcited moieties does not play a role anymore. However, the presence of a ground-state dimer is reflected in additional bands in the absorption spectrum, whereas the existence of excimers does not change the absorption spectrum. Furthermore, ground-state dimers are responsible for a change of the monomer-to-excimer emission intensity ratio upon changing the excitation wavelength. [118]

Unlike pyrene moieties being linked by aliphatic chains, which are well known to exhibit triple-exponential fluorescence decays [123], the restricted intramolecular flexibility of the system under investigation (see figure 6.2) is not expected to afford such a behavior. We therefore expected two fluorescing species: one being attributed to the open conformation and a second one to a π-stacked conformer (*via* rotation about one of the two central C$-$C single bonds). Interestingly, our experiments revealed three absorbing and emitting species.

6.2 Experimental

The compound under investigation, from now on referred to as “pyrene A”, a diphenylacetylene core substituted with two pyrenylethynyl units, was supplied to us by Prof. Dr. Sankararaman from the Indian Institute of Technology Madras. The synthesis of analogous compounds has already been reported [124, 125]. Its molecular structure is illustrated in figure 6.2.

The solvents used, namely hexane (Fluka, puriss. p.a.), acetonitrile (Riedel de Haen, spektranal. grade), propyl acetate (Sigma-Aldrich, puriss. p.a.) and butyronitrile (Fluka, purum $\geq 99.0\,\%$) were distilled and dried over molecular sieves. Paraffin oil (Fluka) was used as received.
Optically dilute solutions (optical density < 0.1) were prepared and deaerated in septa-sealed quartz cuvettes by bubbling with argon for 10 minutes.

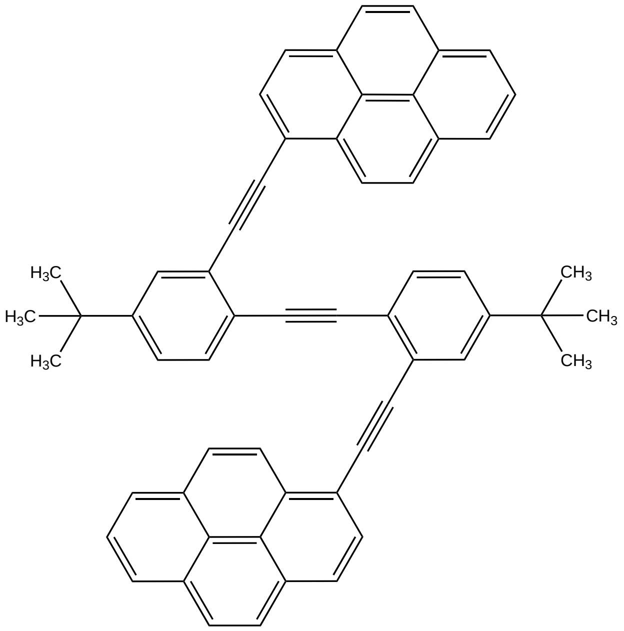

Figure 6.2: Molecular structure of “pyrene A”.

Absorption spectra were recorded on a Shimadzu UV-3101 PC double-beam spectrometer using slit widths of 2 nm. Fluorescence spectra were recorded on a FluoroMax-2 ISA®Jobin YVON-SPEX Instruments Spectrometer allowing for temperature control from 15 to 60 °C.
Temperature scan measurements were performed in a separate, nitrogen purged module, allowing for temperature control from -20 to 80 °C, which was connected to the spectrometer *via* liquid light guides (Lumatec).
Time correlated single photon counting measurements were performed with a 394 nm vertically polarized laser diode as excitation light source. A polarizer set to the magic angle conditions (54.7°) and different interference filters were used in the emission pathway. The set-up was similar to the one described in [91].

6.3 Data Treatment

In the following, the procedure how certain data were obtained and corrected, respectively, shall be explained briefly.

6.3.1 Viscosity

The dynamic viscosity η was determined according to

$$\eta = \nu\rho \tag{6.1}$$

whereas the kinematic viscosity, ν, was measured using a thermostatted Ubbelohde viscosimeter (Schott instruments) and the mass density, ρ, was obtained using a pycnometer.

6.3.2 Emission and Excitation Spectra

For the fluorescence measurements in highly viscous paraffin oil, polarizers (Prinz) were used in excitation and emission. Emission spectra were corrected according to manufacturer specifications.
The total fluorescence emission intensity $I(\lambda)$ is then corrected to

$$I(\lambda) = \frac{I_{\mathrm{VV}}(\lambda) + 2G(\lambda)I_{\mathrm{VH}}(\lambda)}{T(\lambda)} \tag{6.2}$$

where $T(\lambda)$ denotes the transmittance of the emission polarizer and the first subindex in I_{ij} refers to the position of the excitation polarizer transmission axis and the second one to the emission polarizer position, whereas V denotes vertical and H denotes horizontal. The sensitivity of the detection system to differently polarized light is taken into account via $G(\lambda)$, which is given by: [99]

$$G(\lambda) = \frac{I_{\mathrm{HV}}(\lambda)}{I_{\mathrm{HH}}(\lambda)}. \tag{6.3}$$

6.3.3 Quantum Yield

The fluorescence quantum yield ϕ_{x} was obtained using a 10^{-5} M quinine sulfate solution in 0.5 M H_2SO_4 as reference ($\phi_{\mathrm{r}} = 0.55$ [126]) and applying the following equation:

$$\phi_{\mathrm{x}} = \frac{I_{\mathrm{x}}}{I_{\mathrm{r}}}\frac{1 - 10^{-A_{\mathrm{x}}}}{1 - 10^{-A_{\mathrm{r}}}}\frac{n_{\mathrm{r}}^2}{n_{\mathrm{x}}^2}\phi_{\mathrm{r}} \tag{6.4}$$

where I_i denotes the integrated fluorescence intensity of species i, A_i is the absorbance of species i at the excitation wavelength and n_i is the refractive index of the corresponding solution which was determined using a temperature controlled Abbé refractometer (Atago). [126]

6.3.4 Estimation of Absorbing and Emitting Species

The fact that all experimental data inherently possess experimental error requires a criterion for the determination of contributing species.
In order to evaluate the number of participating species in a series of experiments such as excitation/emission spectra (a $c \times r$ data matrix, of r excitation experiments recorded at c wavelengths), a method called "principal component analysis" was applied. Principal component analysis (PCA) is the first step in abstract factor analysis. Based on this method, we chose the "factor indicator function" (IND) introduced by Malinowski, which holds the advantage that no knowledge of the experimental error is needed. The only limitations are that the error has to be relatively uniform and free from systematic influences. [127]
The IND function is defined *via* the real error, RE, as

$$\mathrm{RE} = \left(\frac{\sum\limits_{j=n+1}^{c} \lambda_j}{r(c-n)} \right)^{1/2} \tag{6.5}$$

$$\mathrm{IND} = \frac{\mathrm{RE}}{(c-n)^2} \tag{6.6}$$

where λ_j is the j^{th} eigenvalue, n represents the number of factors used to reproduce the experimental data and r and c are the numbers of rows and columns constituting the data matrix. Malinowski found that the IND function reached a minimum if the correct number of factors was used. We thus analyzed our excitation/emission matrices in acetonitrile, hexane and paraffin oil with respect to this method.

While the determination of the number of independent species is comparably simple and straightforward, the assignment of the corresponding spectra, by *e.g.* using "independent component analysis" (ICA), is not and usually requires substantial additional information (*e.g.* about underlying mechanisms interconverting the individual species). [128, 129]

6.4 Results

First, we performed experiments in hexane and acetonitrile. In these two solvents, we recorded absorption and emission spectra and determined quantum yield and excited-state lifetime of "pyrene A". Oxygen quenching experiments allowed us to disentangle the various emitting species. The recording of a 3D

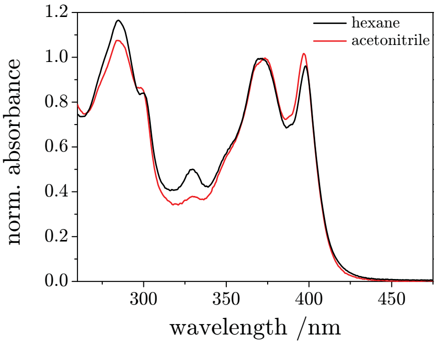

Figure 6.3: Absorption spectra of "pyrene A" in hexane and acetonitrile, respectively.

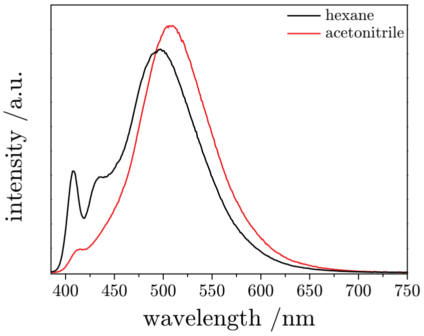

Figure 6.4: Emission spectra of "pyrene A" in hexane and acetonitrile, respectively.

excitation/emission matrix in hexane and acetonitrile, respectively, showed a slight excitation wavelength dependence of the emission spectrum.
Second, we performed temperature scan measurements in THF.
Third, we chose paraffin oil as highly viscous solvent in order to perform another temperature scan as well as absorption, excitation/emission scans and single-photon counting experiments.
As fourth set of experiments, we chose propyl acetate/butyronitrile mixtures for absorption, emission and single-photon counting experiments. Again, we performed oxygen quenching experiments as an attempt to disentangle the various emitting species.

6.4.1 Experiments in Hexane/Acetonitrile

Figures 6.3 and 6.4 depict the absorption and emission spectra of "pyrene A" in hexane and acetonitrile, respectively. The absorption spectra were arbitrarily normalized to the second low lying maximum (in the range from 370 to 380 nm). The emission spectra were recorded using $\lambda_{\text{exc}} = 380\,\text{nm}$.
Both, absorption and emission spectra in these two solvents of similar viscosity ($\eta \approx 0.3\,\text{cP}$) but different dielectric constant (acetonitrile: $\varepsilon_{\text{S}} = 35.94$, hexane: $\varepsilon_{\text{S}} = 1.8799$ [103]) differ.

Figure 6.5 shows the excitation/emission matrices for hexane and acetonitrile in two different representations.
The upper graphics show the matrix when the spectra are normalized to the second low lying maximum in an excitation range. This allows differentiating excitation spectra upon changing the emission wavelength.

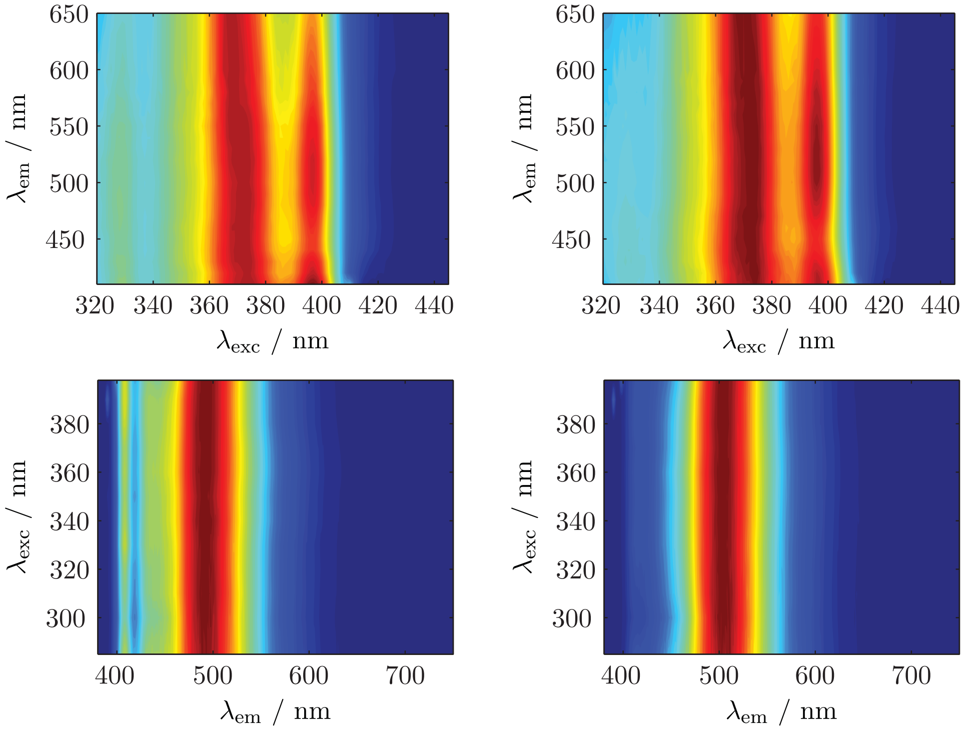

Figure 6.5: 3D excitation spectrum of "pyrene A" in hexane (upper left) and acetonitrile (upper right), respectively. The excitation spectra have been arbitrarily normalized to the second low energy maximum (between $360 < \lambda_{exc} < 380\,\text{nm}$). 3D emission spectrum of "pyrene A" in hexane (lower left) and acetonitrile (lower right). The emission spectra have been arbitrarily normalized to the spectral maximum. [110]

The lower panel shows the same matrix, when being normalized to the emission maximum. Analogous to the previous representation, this allows observing changes in the emission spectra shapes upon changing the excitation wavelength. Slight changes can be made out in the emission spectrum upon changing the excitation wavelength and we could reveal three (instead of the expected two – the monomer and its intramolecular folded excimer) species contributing to the excitation/emission spectra.

Figures 6.6, 6.7, 6.8 and 6.9 summarize the result of applying PCA to the excitation/emission matrix for "pyrene A" in hexane. They show that presumably three spectral components are required to reproduce the entire excitation/emission matrix.
While the residuals between the two component fit and the experimental data (*cf.* figure 6.6) shows notable structure, the same presentation for three

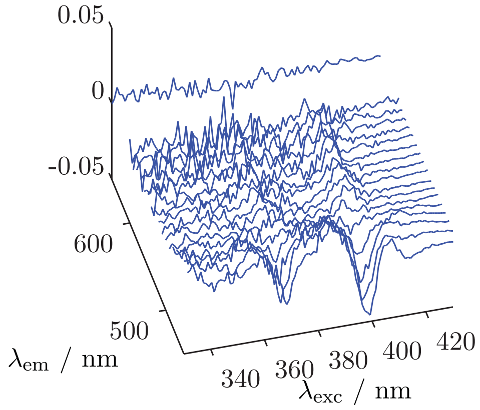

Figure 6.6: Comparison of the residuals when using two components for the description of the 3D excitation/emission matrix of “pyrene A” in hexane. [110]

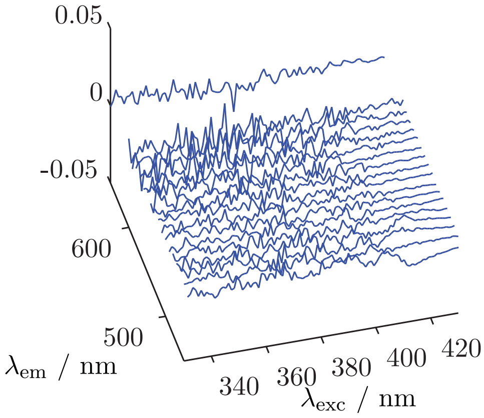

Figure 6.7: Comparison of the residuals when using three components for the description of the 3D excitation/emission matrix of “pyrene A” in hexane. [110]

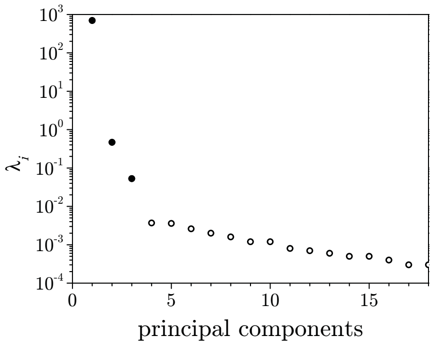

Figure 6.8: Determination of the number of contributing principal components using the magnitude of the eigenvalues. [110]

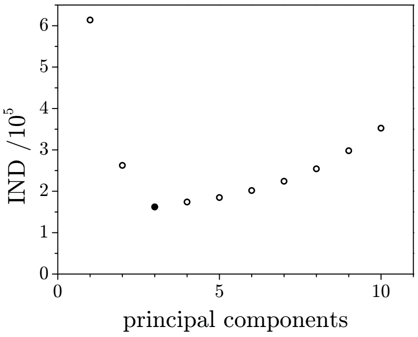

Figure 6.9: Determination of the number of contributing principal components using the factor indicator function. [110]

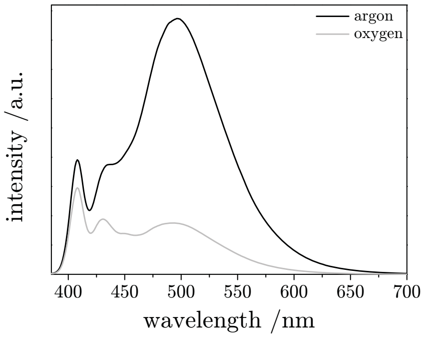

Figure 6.10: Emission spectra ($\lambda_{\mathrm{exc}} = 380\,\mathrm{nm}$) in hexane upon saturation with argon and oxygen, respectively.

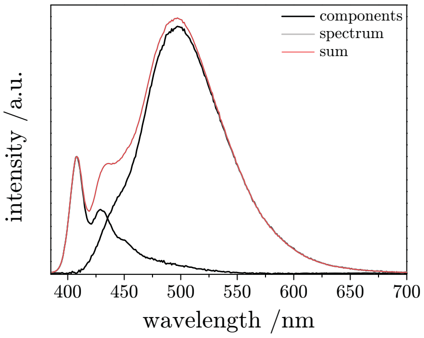

Figure 6.11: Decomposition of the emission spectrum into "monomer" and "intramolecular excimer" in hexane.

species results in perfectly random noise (*cf.* figure 6.7). In accord with this finding is the fact that the size of the first three eigenvalues, obtained from PCA, is notably larger than that of the remaining ones (*cf.* figure 6.8). Eventually, the factor indicator function, introduced in section 6.3.4, shows a minimum when using three principal components (*cf.* figure 6.9).

Figure 6.10 shows the fluorescence spectrum of "pyrene A" in an argon saturated and in an oxygen saturated solution, respectively. From the ratio of these intensities, we attempted to decompose the fluorescence spectrum into the two components which were expected, namely the monomer and an intramolecular excimer. Application of these spectra at different excitation wavelengths resulted in different component spectra, when for two species the two obtained spectral shapes should not at all depend on the excitation wavelength.

6.4.2 Experiments in Tetrahydrofuran

The temperature dependence of the emission spectra of "pyrene A" was studied in THF. Spectra were recorded by coupling a temperature controlled module to the FluoroMax spectrometer *via* liquid light guides. This set-up holds the inconvenience that it does not allow using neither excitation nor emission polarizers. The obtained spectral shapes are thus to be handled with care, as soon as large fluorophores with short fluorescence lifetimes in highly viscous solvents are investigated.

The fluorescence spectra of "pyrene A" in THF in the temperature range

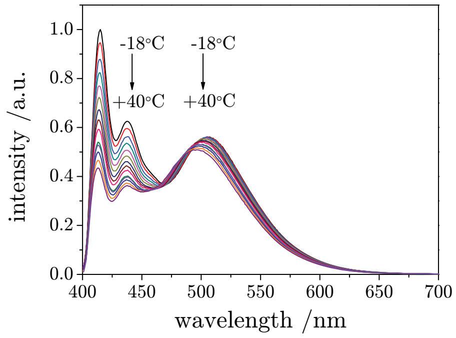

Figure 6.12: Temperature dependence of the emission spectra of "pyrene A" in THF.

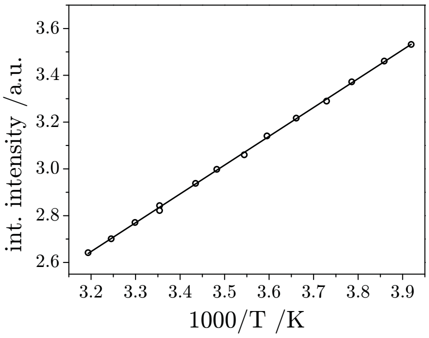

Figure 6.13: Temperature dependence of the emission intensity (quantum yield) of "pyrene A" in THF.

from -18 to +40 °C are shown in figure 6.12. Qualitatively described, the monomer emission decreases drastically as the temperature is raised, while the unstructured red shifted emission remains virtually unaltered. The overall fluorescence quantum yield decreases by more than 40 % in the temperature range studied (*cf.* figure 6.13).

6.4.3 Experiments in Propyl Acetate/Butyronitrile Mixtures

It has been shown recently that mixtures of propyl acetate/butyronitrile allow changing the dielectric constant ε_S from 6 to 24 while keeping viscosity and refractive index constant [130]. The experiments in propyl acetate/butyronitrile mixtures were performed in order to investigate the dependence of the emission spectra on the dielectric constant ε_S (*cf.* figure 6.14).

Increasing the dielectric constant results

- in a slight shift of the entire spectrum to lower energies and
- in an increase of the relative intensity of the unstructured emission(s).

The unsuccessful attempt to disentangle the spectra into monomer and excimer from the oxygen quenching behavior led to the assumption of again three species being present. The presumable presence of three species inhibited us from obtaining further insights as it was not possible to extract

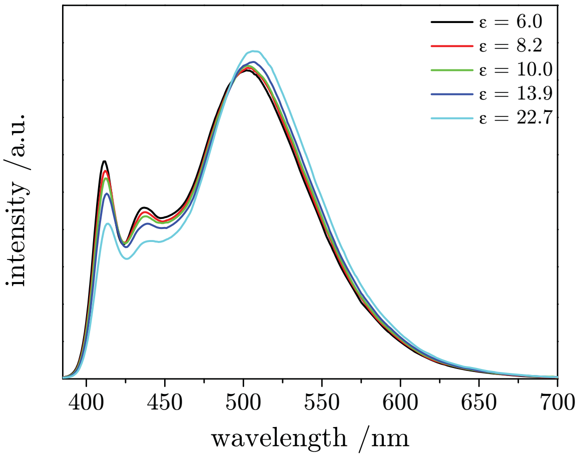

Figure 6.14: Dependence of the emission spectra ($\lambda_{\text{exc}} = 374\,\text{nm}$) on the dielectric constant of the solvent, ε_S, in mixtures of propyl acetate/butyronitrile with $6 < \varepsilon_S < 23$ ($\eta = 0.58\,\text{cP}$). Note that the structured band decreases with increasing dielectric constant, while the broad emission at longer wavelengths increases.

the individual spectral shapes. It should, however, be noted that the obtained time-resolved data in the propyl acetate/butyronitrile mixtures hint at a trend of a decreasing τ_1 upon increasing ε_S, which is in line with the observations for hexane and acetonitrile.

6.4.4 Experiments in Paraffin Oil

The temperature dependence of the fluorescence of “pyrene A” in paraffin oil in the range from 16.5 to 56.8 °C is depicted in figure 6.15. Apparently the structured component decreases (also observed in decreasing τ_1) while the unstructured component(s) increase. Within the experimental error, the quantum yield did not change with temperature and thus viscosity. This finding is contrary to the findings in THF. However, we assume that the expected decrease of about 10 % of ϕ in the observed temperature range is too small for the experimental error of the measurements in paraffin oil. It shall be kept in mind that the paraffin oil measurements were primarily aimed at and devised for the elucidation of the number of spectral species.

The excitation/emission matrix (depicted in figure 6.16) was subjected to a principal component analysis, giving rise to at least three different contributing species. An independent component analysis of the three major

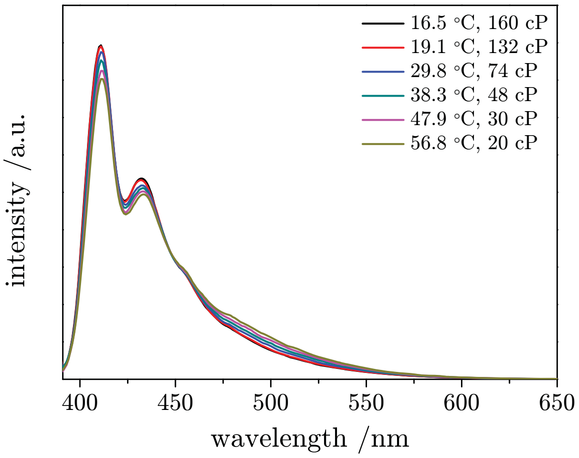

Figure 6.15: Temperature and viscosity dependence of the emission spectra of "pyrene A" in paraffin oil. Note, that upon increasing the temperature the intensity of the structured band decreases while the intensity of the broad emission at longer wavelengths increases.

principal components was performed using the MCR-ALS program written and published online by R. Tauler, A. de Juan and J. Jaumot [131]. The alternating least squares procedure for the optimization was subjected to the following constraints:

- only non-negative spectral components and
- only non-negative relative contributions of these components.

As initial guesses, the two excitation spectra at the extremal emission wavelengths and a spectrum at intermediate emission wavelength were chosen. The fitting result is depicted in figure 6.17. It should, however, be noted that the given spectra do not necessarily represent the "true" component spectra. Finally the absorption spectrum of "pyrene A" in paraffin oil was decomposed into the three spectral components obtained from the MCR-ALS program (*cf.* figure 6.18).

6.5 Conclusion

The main conclusion which can be drawn from a comparison of absorption and excitation spectra of "pyrene A" as well as from the 3D excitation/emission matrices in hexane, acetonitrile and paraffin oil and the applied

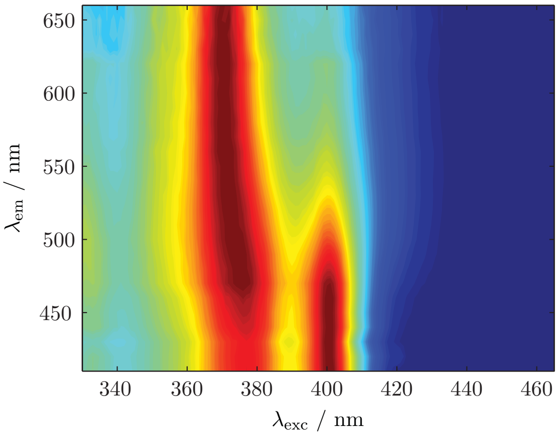

Figure 6.16: 3D excitation spectrum of "pyrene A" in paraffin oil at 16.5 °C. The excitation spectra have been arbitrarily normalized to the spectral maximum. [110]

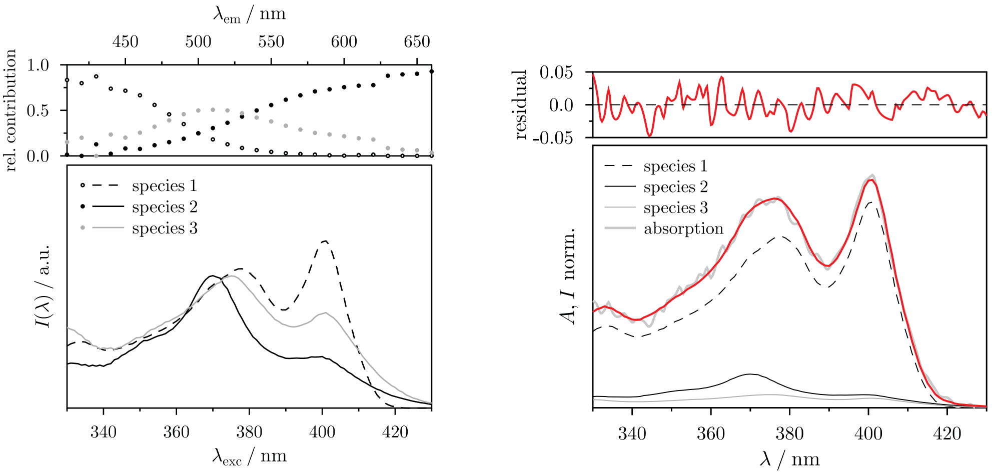

Figure 6.17: Three possible spectral species (excitation spectra) obtained from ICA on "pyrene A" in paraffin oil at 16.5 °C and their corresponding relative contributions at the different emission wavelengths. [110]

Figure 6.18: Decomposition of the absorption spectrum in paraffin oil into the contributions of the three spectral species obtained from ICA on the excitation/emission matrix. [110]

principal component analysis is that presumably three spectral species are contributing in the system investigated. All experimental evidences point at three absorbing (three different excitation spectra) and emitting (three different emission spectra) species for “pyrene A”.

The fact that the excitation spectrum is not identical to the monomeric one gives evidence that the intramolecular dimer(s) does (do) not only exist in the excited state but also in the ground electronic state.

The fact that the fluorescence decay curves could only be fitted by triple exponentials gives additional evidence for the presence of three emitting species. These findings are rather surprising as initially we had expected only two components, namely a monomer and an intramolecular dimer.

Time-Resolved Fluorescence

From the fluorescence decays it becomes evident that presumably three emitting species are present. While the lifetimes of the two long-lived spectral components seem to be little to not affected by the solvent, the lifetime of the short-lived definitely is (*cf.* table 6.1). Two influences are observable:

1. Decreasing solvent viscosity by increasing the temperature leads to a decrease in τ_1. This can either be understood in terms of an enhanced formation of the intramolecular excimer and/or an additional increase of the non-radiative rate constant or different populations of different conformers. Most probably the observed dependence is the result of a combination of these influences.

2. Comparison of hexane and acetonitrile – both having similar viscosity – indicates that the monomer to excimer conversion proceeds slower in the former than in the latter. An effect of the non-radiative rate constant of the monomer does not seem to interfere as the overall fluorescence quantum yield remains unaltered upon changing the solvent.

Quantum Yield

The quantum yield of “pyrene A” is, within experimental error, independent of

- the excitation wavelength (from 280 to 410 nm),

- the dielectric constant of the medium (compare the values for acetonitrile, hexane and the propyl acetate/butyronitrile mixtures in table 6.1) and of

Table 6.1: Fluorescence lifetimes and quantum yields of “pyrene A” in the studied solvents and some of their corresponding properties.
n.m. stands for “not measured” and pa/bn for the propyl acetate/butyronitrile mixture.

solvent	θ /°C	ε_S	η /cP	ϕ	τ_1 /ns	τ_2 /ns	τ_3 /ns
paraffin oil	20	≈ 2	160	n.m.	1.8	14	34
acetonitrile	22	35	0.3	0.62[a]	0.2	15	37
hexane	22	2	0.3	0.59[a]	0.4	14	37
pa/bn	22	6 to 23	0.58	0.63[b]	0.8	14	37

[a] *vs.* quinine sulfate in 0.5 M H_2SO_4 [b] *vs.* DCA in dioxane

- temperature and solvent viscosity within the temperature range (15 to 60 °C) and viscosity range (160 to 23 cP) covered in the paraffin oil experiment*.

6.6 Future Outlook

More experiments with an eventually purified sample are necessary in order to be able to assign the third component to any particular conformation or substance.

Once the nature of the third contributing component is solved, a detailed study of the temperature, viscosity and dielectric constant dependence will allow for further interesting and revealing insights. The use of various alkanes as solvents would allow to establish the effects of temperature and viscosity on the fluorescence properties of “pyrene A”, which has not been possible through the use of paraffin oil at different temperatures as a means to change viscosity. For a more detailed study, a larger temperature range and the individual spectral components should be accessible, *e.g.* by performing the temperature scan with argon and oxygen saturated solutions. Especially the dielectric constant dependence is of interest as the monomer emission of pyrene decays within 200 ps in acetonitrile (compare to the value of 200 ns for pyrene itself), while it takes twice as long in hexane and a factor of four longer in the propyl acetate/butyronitrile mixtures.

---

* However, the experimental error is within the range of the expected change extrapolated from the THF temperature dependent measurements.

Furthermore, in conjunction with optical spectroscopy, an investigation by means of EPR/ENDOR could reveal interesting results. Additionally, the “pyrene A - model compound”, a molecule with only one pyrenylethynyl unit which is thus unable to form intramolecular dimers could contribute to revealing further insights.

Chapter 7

Extended Phenylenediamines

Despite the predominant electron donor character of extended *p*-phenylenediamine derivatives, our studies show that they cannot only be oxidized, giving well-known Wurster type radical cations, but as well be reduced, giving radical anions. We chemically generated radical cations and anions and analyzed them using EPR/ENDOR spectroscopy. Supported by DFT calculations, we were able to reveal the extent of π electron delocalization in the paramagnetic species. Furthermore, we performed electrochemical characterizations using cyclic voltammetry. With regard to the photophysical characterization, we recorded absorption, emission and excitation spectra, determined the quantum yield and the excited-state lifetime of the species in hexane and acetonitrile, respectively.*

The molecules under investigation constitute building blocks of conjugated organic polymers and are thus of interest for their application as molecular wires. Due to their characteristic electronic properties, persistent oxidized as well as reduced stages, they are handled as substitutes for conventional materials in optoelectronic devices, *e.g.* organic light-emitting diodes. [6]

7.1 Introduction

The oxidation products of *p*-phenylenediamines and their derivatives have a long history in chemistry, since they were first described by Wurster in 1879 [132]. The one-electron oxidation product of *N,N,N',N'*-tetramethyl-*p*-

---

* The present chapter, with few adjustments, serves as a manuscript version to be handed in with a peer-reviewed journal with following authorship: C. Onitsch, Dr. A. Rosspeintner, Dr. G. Angulo, Dr. M. Kivala, Dr. B. Frank, Prof. F. Diederich, Prof. G. Grampp and Prof. G. Gescheidt.

phenylenediamine, also called Wurster's blue radical cation, owes its stability to the π electron delocalization in its semi-quinone structure [133, 134]. Being one of the most stable organic radicals, Wurster's radical cations were even among the first to be investigated by EPR spectroscopy [135]. Since then, numerous papers have been published dealing with the radical cations of various *p*-phenylenediamines.

Michaelis *et al.* dealt with the stability and color of the free radicals of the type of Wurster's salts [136], as well as Milligan who studied higher members of the Wurster salts series [137]. Yamauchi *et al.* examined the magnetic properties of the *N,N,N',N'*-tetramethyl-*p*-phenylenediamine cation radical ("Wurster's Blue") and the effect on changing its counterions [138, 139]. Grampp *et al.* published their EPR/ENDOR investigations on substituted *N,N,N',N'*-tetraalkyl-*p*-phenylenediamine radical cations in solution [140]. Furthermore, they reported on the dimerization enthalpies of substituted *p*-phenylenediamines [141]. Omelka *et al.* have as well investigated the cation radicals of *N*-phenyl substituted *p*-phenylenediamine [142].

However, only a few examples of radical anions of substituted *p*-phenylenediamines are present in the literature. Gerson *et al.* reported on a one-electron reduction of a *N*-trimethylsilyl-substituted *p*-phenylenediamine to a radical anion which was established by means of EPR in 1969 [143, 144]. They explained their success in reducing an electron-rich molecule with a distortion of the n_N/π-delocalization due to a twisting of the bulky $[Me_3Si]_2N$ groups around the bond between the N and the ring C atom [145]. Stegmann *et al.* reported on the formation of radical anions of substituted *o*-phenylenediamine upon reaction with diphenylthallium hydroxide [146]. Angulo *et al.* published their work on a spectroscopic characterization of tetracyano-*p*-phenylenediamine, which, although containing the *p*-phenylenediamine moiety, due to the substitution with four cyano groups becomes a strong oxidant and can rather be regarded as a cyanobenzene-derivative than as a representative of the *p*-phenylenediamine group [147].

In contrast to our studies, the examples given above deal with substituted *p*-phenylenediamine derivatives which ascribe their special abilities to substitution with acceptor groups. In our study, we report on EPR/ENDOR and optical studies on the *p*-phenylenediamine derivatives without acceptor substitution, namely **1**, 4,4'-[1,4-phenylenebis(ethyne-2,1-diyl)]bis(*N,N*-dihexylaniline), and **2**, 4-[[4-(dimethylamino)phenyl]ethynyl]-*N,N*-dimethylaniline, respectively. Synthesis of the compounds under investigation has already been described in [148, 149].

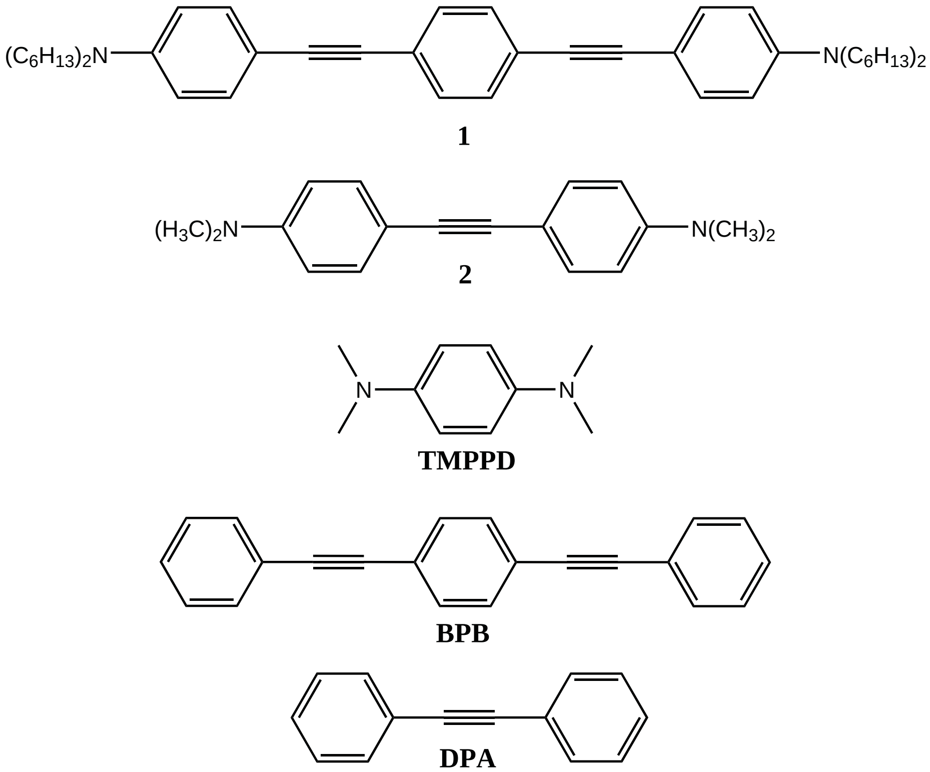

Figure 7.1: Molecular structures of the extended phenylenediamines **1**, 4,4'-[1,4-phenylenebis(ethyne-2,1-diyl)]bis(*N,N*-dihexylaniline) and **2**, 4-[[4-(dimethylamino)phenyl]ethynyl]-*N,N*-dimethylaniline as well as of the reference compounds *N,N,N',N'*-tetramethyl-*p*-phenylenediamine (**TMPPD**), 1,4-bis(phenylethynyl)benzene (**BPB**) and diphenylacetylene (**DPA**).

We found that **1** and **2** cannot only be oxidized but as well be reduced and analyzed the generated radical cations and anions using EPR/ENDOR spectroscopy. Density functional theory (DFT) calculations allowed us to reveal the extent of π electron delocalization in the paramagnetic species and shed light onto the geometry and bond lengths. Furthermore, we used cyclic voltammetry to gain insight into the thermodynamics of the redox processes. We recorded absorption, emission and excitation spectra, determined the quantum yield and the excited-state lifetime of the species in an apolar and a polar solvent, hexane and acetonitrile, respectively, in order to establish elementary differences originating in solvent effects.

Recently, we performed an elaborate study of these solvent effects of **1** and **2** in 25 solvents. We found solute polarizability to be responsible for the bathochromic shifts in the optical spectra upon increasing solvent polarity (see section 7.5.1). [6]

As reference compounds, we not only chose *N,N,N',N'*-tetramethyl-*p*-phenylenediamine (**TMPPD**) but as well the unsubstituted cores, 1,4-bis-(phenylethynyl)benzene (**BPB**) and diphenylacetylene (**DPA**), commonly referred to as tolan, in order to inspect the influence of the aromatic moiety of the molecules. Both molecules also served as reference compounds for our solvatochromic study [6].

7.2 Experimental

7.2.1 EPR/ENDOR

EPR and ENDOR spectra were recorded on a Bruker ESP 300 X-band spectrometer. Measurements were performed at 220 K. EPR spectra simulations were performed by means of WinSim, a public domain program [150].

Radical Cations

Dichloromethane was heated to reflux over molecular sieves and stored under these water-free conditions under high vacuum. For sample preparation, the required volume was condensed into the Pyrex glass tube which was connected to the vacuum line. It was degassed by three or four freeze-pump-thaw cycles under high vacuum. 1,1,1,3,3,3-Hexafluoropropan-2-ole (HFP) was bought from Aldrich and stored under argon after distillation. The required volume of HFP was transferred into the sample tube with a syringe and after sealing the glass, it was degassed by three or four freeze-pump-thaw cycles similar to CH_2Cl_2. Trifluoroacetic acid (TFA) and phenyliodine(III) bistrifluoroacetate (PIFA) were purchased from Aldrich and used without further purification. Oxidations were performed under high vacuum by mixing of the solutions of the sample with that of the oxidizing agents.

Radical Anions

THF was heated to reflux over a Na/K alloy and stored over a Na/K alloy under high vacuum. Its deep blue color was used as indicator for perfect water-free conditions. Sample preparation was performed in a special sample tube which was connected to the vacuum line. First, a K metal mirror was sublimated to the wall of the sample tube and next, about 0.4 ml THF were freshly condensed in the sample tube where it was degassed by three or four freeze-pump-thaw cycles under high vacuum. The sample tube was then disconnected from the vacuum line by melting it off under high vacuum. Reduction was performed by contact of the THF solution of the parent molecule with the K metal mirror in the evacuated sample tube. Samples were stored at 190 K (isopropanole/dry ice bath) or immediately transferred into the microwave cavity of the ESR spectrometer, which was cooled to 220 K with the vapor of liquid nitrogen.

7.2.2 Electrochemistry

Cylic voltammograms were recorded by Dr. G. Angulo at the Institute of Physical Chemistry, Polish Academy of Sciences, Warsaw, Poland.
Solutions of 1 mM of the species and 0.1 M tetrabutylammonium hexafluorophosphate (Bu_4NPF_6) as conducting salt were prepared in acetonitrile (Aldrich spectrophotometric grade, used as received). A W-wire served as reference electrode and a Pt-disc of 2 mm diameter which was always freshly polished with diamond paste as working electrode. A Pt-wire was used as counter electrode. The scan rate for cyclic voltammetry was set to be $100\,^{\mathrm{mV}}/_{\mathrm{s}}$. Ferrocene was used as an internal reference. Oxygen was purged from the solutions with dried argon for at least 15 minutes.

7.2.3 Photophysics

Hexane ($\varepsilon_S = 1.8799$, $\eta = 0.2942$ cP at 298 K [103]) (Fluka) and acetonitrile ($\varepsilon_S = 35.94$, $\eta = 0.341$ cP at 298 K [103]) were distilled and dried over molecular sieves, pore size 4 Å and 3 Å, respectively.
Quinine hemisulfate monohydrate 99 % (Alfa Aesar) in 1 N H_2SO_4 (Loba Feinchemie) was used as received as a quantum yield standard, as it meets most of the requirements for an ideal standard, as defined *e.g.* in [126].

Absorption spectra were recorded on a Shimadzu 3101-UVPC double-beam spectrometer, using slit widths of 2 nm. Fluorescence spectra were recorded on a Jobin Yvon FluoroMax-2 spectrometer, allowing for temperature control.
Time-resolved measurements were performed making use of both, time-correlated single-photon counting and modulation technique using a digital storage oscilloscope in a setup as described in [91]. In the case of **1**, a 370 nm light-emitting diode (PicoQuant) was used as excitation source as well as filters in excitation (Schott UG 11) and in emission (long pass: Schott GG 400 plus KS 385). In the case of **2**, a 340 nm light-emitting diode (PicoQuant) and a

long pass filter in emission (Schott GG 360) were used. Both, steady-state and time-resolved measurements were performed temperature-controlled at 298 K.

For determination of the extinction coefficients, solutions which did not exceed an OD of 1 were prepared. Thus absorption spectra were recorded in the linear range of Beer-Lambert Law [111]. Emission measurements were performed with optically dilute solutions (OD∼0.05) in septa-sealed quartz-cuvettes. All samples were deaerated by bubbling with argon for 15 minutes. Spectra were corrected according to manufacturer specifications.

7.3 Results and Discussion

Starting with an analysis of the hyperfine splitting constants obtained from EPR/ENDOR spectroscopy and a comparison to other *p*-phenylenediamine derivatives, we go on to the electrochemical and photophysical characterization.
The section on "solvatochromism" (section 7.5.1) constitutes a short overview on our solvatochromic studies which were already published (see reference [6]).

7.3.1 EPR/ENDOR Results

This section is organized in two parts: the first one deals with the wide-spread and well-known radical cations and the second one with radical anions which are rather unusual for this type of molecules.

Radical Cations

Oxidations were attempted with $AgClO_4$ in HFP, $AlCl_3$ in CH_2Cl_2 and PIFA in acetonitrile, respectively, but without success. The use of PIFA in CH_2Cl_2 and thallic trifluoroacetate in CH_2Cl_2, respectively, did not give EPR spectra with a lifetime sufficient for precise analysis.
For the oxidation of the parent molecules **1** and **2**, the combination of PIFA and TFA serving as oxidants in HFP under high vacuum has proven to be the most successful, yielding spectra of an intensity which allowed straightforward analysis (see figure 7.2 for the EPR spectrum of $\mathbf{1}^{\bullet\oplus}$ and figure 7.3 for that of $\mathbf{2}^{\bullet\oplus}$).

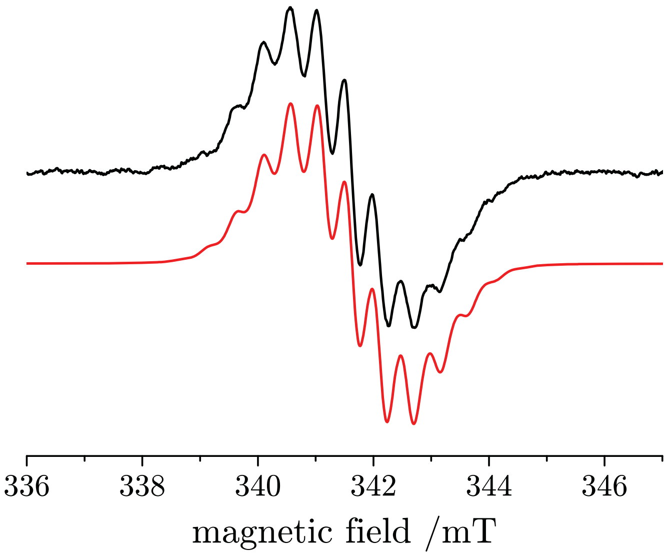

Figure 7.2: Experimental (upper) and simulated (lower) EPR spectra of $\mathbf{1}^{\bullet\oplus}$.

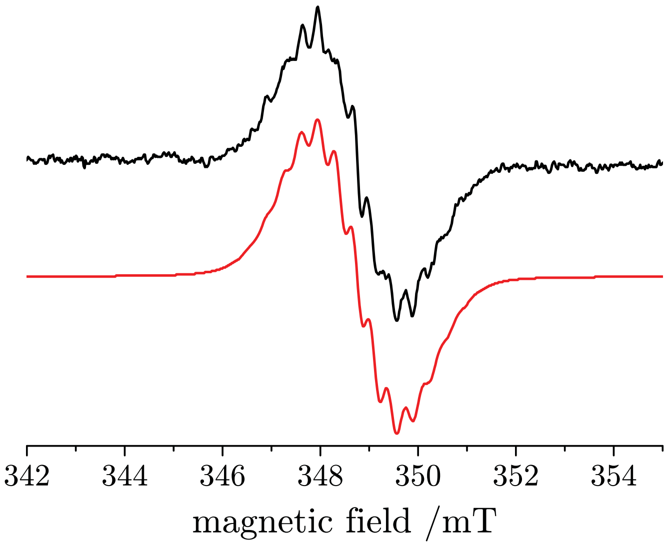

Figure 7.3: Experimental (upper) and simulated (lower) EPR spectra of $\mathbf{2}^{\bullet\oplus}$.

The EPR spectrum of $\mathbf{1}^{\bullet\oplus}$ shows a structured, but not fully resolved pattern. The two highest hfsc can be assigned to the protons of the methylene groups (0.481 mT) and to the nitrogen atoms (0.224 mT). The three smaller hfsc of 0.091 mT, 0.041 mT and 0.066 mT belong to the four *ortho*- and *meta*-protons and the protons on the central ring, respectively (see table 7.1).

The EPR spectrum of $\mathbf{2}^{\bullet\oplus}$ is less structured than that of $\mathbf{1}^{\bullet\oplus}$. For $\mathbf{2}^{\bullet\oplus}$, the dominating hfsc can again be assigned to the protons of the methyl groups (0.382 mT) and to the nitrogens (0.349 mT). The smaller hfsc of 0.257 mT and 0.066 mT belong to the *ortho*- and *meta*-protons, respectively (see table 7.2). The higher ^{14}N hfsc of $\mathbf{2}^{\bullet\oplus}$ in comparison to $\mathbf{1}^{\bullet\oplus}$ goes hand in hand with the smaller conjugated π system of molecule **2** which leaves a higher portion of the spins at the N atoms.

For the radical cations, the hybridization on the nitrogen has substantial sp^2 character due to the significant amount of spin located at the rather large N atoms. They thus appear rather planarized. A shorter bond length as well as double-bond character can be postulated for the radical cations, as proposed from the quantum-mechanical calculations: For **2**, the bond length between the N and the C of the methyl group decreases from 1.447 $\AA$ for $\mathbf{2}^{\bullet\ominus}$ to 1.358 $\AA$ for $\mathbf{2}^{\bullet\oplus}$. Furthermore, the calculations revealed the planar structure for $\mathbf{2}^{\bullet\oplus}$. The long hexyl substituents in **1** allow only for certain conformations on the EPR time scale, whereas the smaller methyl groups can be regarded as freely rotating.

The high spin population on the nitrogen and the adjacent methyl and methylene group, respectively, of $\mathbf{1}^{\bullet\oplus}$ and $\mathbf{2}^{\bullet\oplus}$ is in line with the those of Wurster's Blue radical cation $\mathbf{TMPPD}^{\bullet\oplus}$ (^{14}N hfsc of 0.705 mT and ^{1}H hfsc of the –CH_3 group of 0.677 mT in absolute methanol at 293 K [151]) and other Wurster's radical cations [140].

Radical Anions

Prior to contact of the solution with the K metal mirror, no EPR signal was observed. After reduction of the parent molecules **1** and **2** with a K metal mirror under high vacuum, the solution turned from colorless to purple (see absorption spectrum of the radical anion in section 7.5.2) and yielded EPR spectra which could be very well analyzed using hfsc derived from ENDOR spectroscopy (see figures 7.6 and 7.8 for EPR/ENDOR spectra of $\mathbf{1}^{\bullet\ominus}$ and figures 7.7 and 7.9 for spectra of $\mathbf{2}^{\bullet\ominus}$).

Table 7.1: Hyperfine splitting constants of $\mathbf{1}^{\bullet\oplus}$ and $\mathbf{1}^{\bullet\ominus}$ obtained by ENDOR and EPR in mT.

	$\mathbf{1}^{\bullet\oplus}$		$\mathbf{1}^{\bullet\ominus}$		
	EPR	calc	ENDOR	EPR	calc
N	0.224 (2)	+0.280 (2)	-	0.093 (2)	+0.057 (2)
c-H	0.066 (4)	-0.054 (4)	0.047 (1.32 MHz)	0.045 (4)	-0.099 (4)
o-H	0.091 (4)	-0.096 (4)	0.109 (3.05 MHz)	0.112 (4)	+0.085 (4)
m-H	0.041 (4)	-0.042 (4)	0.138 (3.87 MHz)	0.136 (4)	-0.219 (4)
$–CH_2–$	0.481 (8)	+0.322 (12)	0.023 (0.64 MHz)	0.023 (8)	+0.031 (12)

Table 7.2: Hyperfine splitting constants of $\mathbf{2}^{\bullet\oplus}$ and $\mathbf{2}^{\bullet\ominus}$ obtained by ENDOR and EPR in mT.

	$\mathbf{2}^{\bullet\oplus}$		$\mathbf{2}^{\bullet\ominus}$		
	EPR	calc	ENDOR	EPR	calc
N	0.349 (2)	+0.377 (2)	-	0.048 (2)	-0.078 (2)
o-H	0.257 (4)	-0.125 (4)	0.073 (2.03 MHz)	0.071 (4)	+0.087 (4)
m-H	0.066 (4)	-0.068 (4)	0.280 (7.84 MHz)	0.280 (4)	-0.318 (4)
$–CH_3$	0.382 (12)	+0.427 (12)	0.034 (0.94 MHz)	0.035 (12)	+0.027 (12)

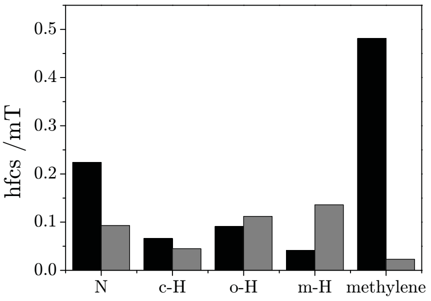

Figure 7.4: Spin distribution of $\mathbf{1}^{\bullet\oplus}$ (black) and $\mathbf{1}^{\bullet\ominus}$ (gray), respectively.

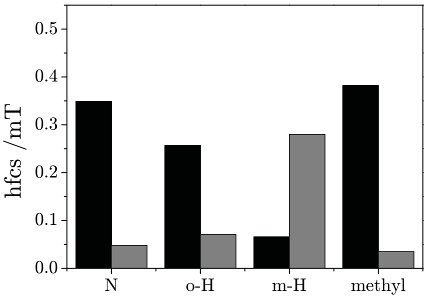

Figure 7.5: Spin distribution of $\mathbf{2}^{\bullet\oplus}$ (black) and $\mathbf{2}^{\bullet\ominus}$ (gray), respectively.

The observed spectral pattern of $\mathbf{1}^{\bullet\ominus}$ is produced by five different hfsc. The two largest hfsc of 0.136 mT and 0.112 mT can be assigned to the four

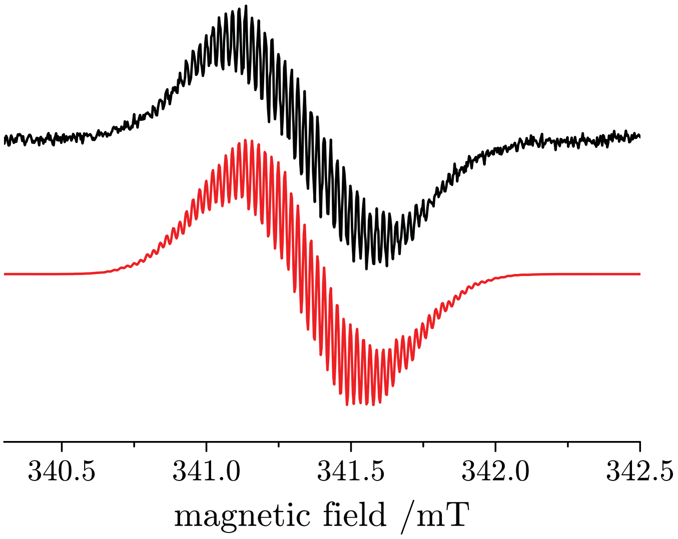

Figure 7.6: Experimental (upper) and simulated (lower) EPR spectra of **1**$^{\bullet\ominus}$.

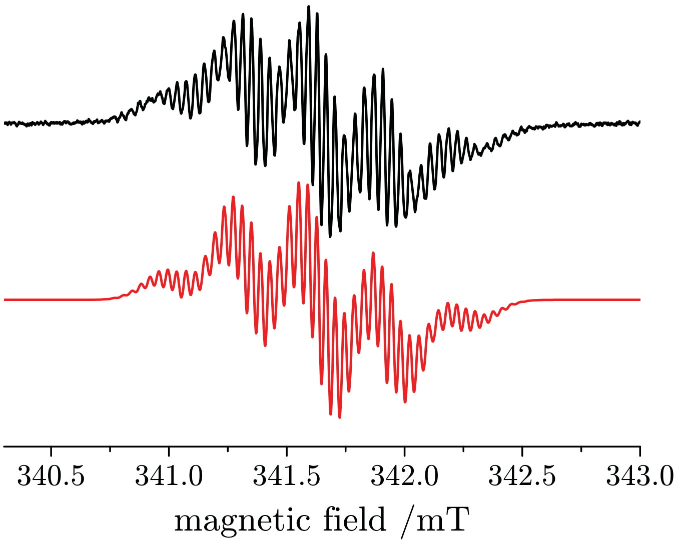

Figure 7.7: Experimental (upper) and simulated (lower) EPR spectra of **2**$^{\bullet\ominus}$.

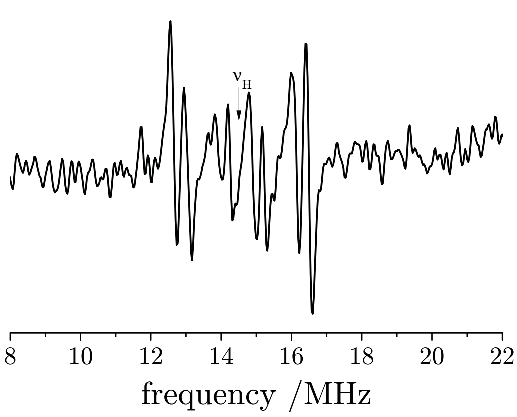

Figure 7.8: ENDOR spectrum of $\mathbf{1}^{\bullet\ominus}$.

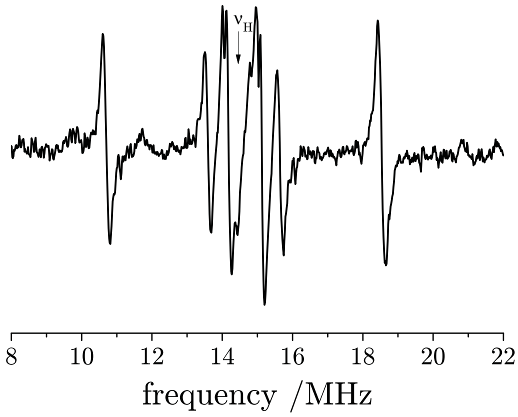

Figure 7.9: ENDOR spectrum of $\mathbf{2}^{\bullet\ominus}$.

equivalent *meta*-protons and the four equivalent *ortho*-protons, respectively, of the outermost phenyl groups. The smaller hfsc of 0.045 mT can be assigned to the four equivalent protons on the central benzene ring. The smallest hfsc of 0.023 mT belongs to the eight equivalent protons of the four α-methylene groups attached to the amino nitrogen atoms. Furthermore, EPR simulation revealed a hfsc of 0.093 mT for the amino nitrogen atom (see table 7.1).

For the radical anion of $\mathbf{2}^{\bullet\ominus}$, the EPR spectrum is made up by four different hyperfine splitting constants. The largest hfsc of 0.280 mT belongs again to the four equivalent *meta*-protons, followed by the four equivalent *ortho*-protons with a hfsc of 0.071 mT. The hfsc of 0.035 mT can be attributed to the twelve protons of the methyl groups. The hfsc of 0.048 mT of the two nitrogen atoms is again well in line with the quantum-mechanical calculations (see table 7.2).

As has been shown in a previous work [152], the hfsc of nitrogen atoms can depend – among other things – on the hybridization, so to speak the extent of pyramidalization on the N center. Contrary to the radical cations, a pyramid can be proposed for the geometry on the nitrogen for the radical anions. Two opposite effects can thus be observed: Due to the sp^3 hybridization, there should be less spin density on the nitrogen atom. However, on the other hand, the more pronounced pyramid leads to a stronger coupling.

The hfsc obtained for the **DPA**-derived molecule **2** are well in line with those of $\mathbf{DPA}^{\bullet\ominus}$ itself. For both molecules, spin population is higher for the ring protons closer to the center (*meta*-H in the case of **2**, *ortho*-H in the

Table 7.3: Hyperfine splitting constants of **DPA**$^{\bullet\ominus}$ obtained by EPR in mT (note the different assignment of *ortho*, *meta* and *para* in this case).

	from [153][a] /mT	from [154][b] /mT	from [155][c] /mT
o-H	0.268 ± 0.005	0.280	0.264
m-H	0.062 ± 0.005	0.060	0.056
p-H	0.475 ± 0.005	0.508	0.482

[a] in THF and DME, 293 K [b] 233 K [c] in DME, 213 K

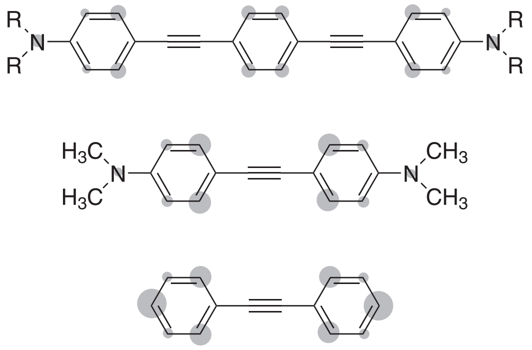

Figure 7.10: Schematic overview of the hfsc of **1**$^{\bullet\ominus}$, **2**$^{\bullet\ominus}$ and **DPA**$^{\bullet\ominus}$.

case of **DPA**) than for those more outside (*ortho*-H in the case of **2**, *meta*-H in the case of **DPA**). The large hyperfine splitting constant in *para*-position of **DPA** is a consequence of the smaller system in **DPA**.

7.3.2 Electrochemistry

Cyclic voltammograms were recorded in acetonitrile with ferrocene as internal standard with a scan rate of 100 mV/s. The oxidation potentials are listed in table 7.4.

The cyclic voltammogram of **1** indicates three irreversible oxidation peaks, at 0.545 V, 0.735 V and 0.830 V *vs.* SCE, respectively. Within the experimental electrochemical window (roughly from +2.5 V to -2.5 V) no reduction was observed. However, the reader should keep in mind that the fact that no reversibility in cyclic voltammetry experiments is observed, is not contradictory to the fact that a stable EPR can be observed. Both, the experimental conditions and sensitivity of EPR spectroscopy differ from those in electrochemical experiments.

Table 7.4: Oxidation peak potentials of **1** and **2** in acetonitrile *vs.* SCE, recorded with a scan rate of $100\,{}^{\mathrm{mV}}/_{\mathrm{s}}$ at room temperature.

	$E_{\mathrm{ox},1}$ /V	$E_{\mathrm{ox},2}$ /V	$E_{\mathrm{ox},3}$ /V
1	0.545	0.735	0.830
2	0.615	0.710	0.914

For **2**, the cyclic voltammogram indicates oxidation peaks at 0.615 V, 0.710 V and 0.914 V *vs.* SCE. The cyclic voltammogram shows a higher reversibility than in the case of **1**, but it is still considered irreversible. Again, no reduction is observed within the experimental electrochemical window (roughly from +2.5 V to -2.5 V).

The shape of the observed cyclic voltammograms can be explained by an ECE (electrochemical-chemical-electrochemical) process, but the attribution is not straightforward. For TMPPD, two separate oxidation steps are reported in the literature (-0.280 V and +0.295 V *vs.* $\mathrm{Fc^+/Fc}$ in acetonitrile [156]) whereas the oxidation potential is decreasing when going to longer substituents [140].

7.3.3 Photophysics

This section describes our photophysical studies in hexane and acetonitrile. A more detailed study on the influence of different studies is presented in the section on solvatochromism (section 7.5.1).

Absorption/Extinction Coefficients

The absorption maximum of **1** in hexane appears at 365 nm, whereas it is red-shifted to 380 nm in acetonitrile (broad and unstructured band). The maximum extinction coefficients in both hexane and acetonitrile are extraordinarily high: $75{,}600\,{}^{1}/_{\mathrm{mol\,cm}}$ and $74{,}400\,{}^{1}/_{\mathrm{mol\,cm}}$, respectively (*cf.* table 7.5). The absorption maximum of **2** in hexane lies at 322 nm, whereas the absorption is again red-shifted to 329 nm in acetonitrile. The maximum extinction coefficients in both hexane and acetonitrile are high: $48{,}300\,{}^{1}/_{\mathrm{mol\,cm}}$ and $47{,}600\,{}^{1}/_{\mathrm{mol\,cm}}$, respectively (*cf.* table 7.5). In acetonitrile, absorption is broad for both molecules.

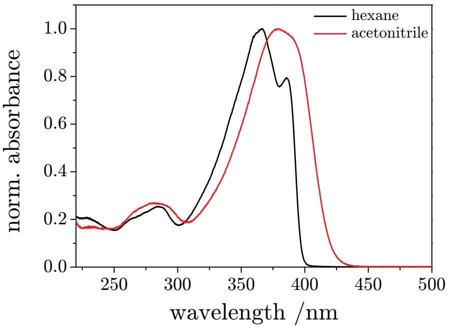

Figure 7.11: Normalized absorption spectra of **1** in hexane and acetonitrile, respectively.

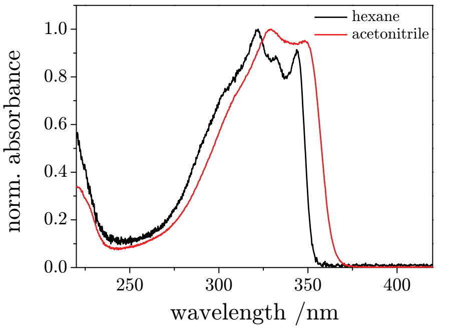

Figure 7.12: Normalized absorption spectra of **2** in hexane and acetonitrile, respectively.

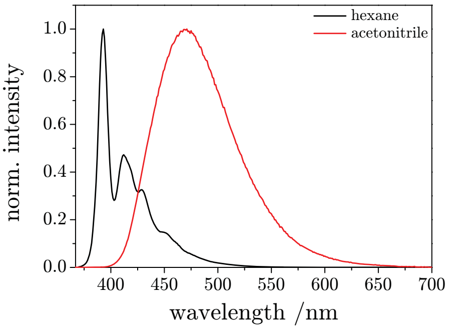

Figure 7.13: Normalized emission spectra of **1** in hexane and acetonitrile, respectively.

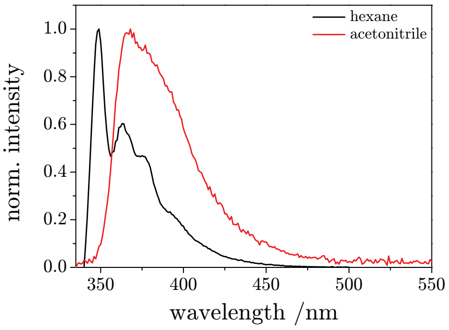

Figure 7.14: Normalized emission spectra of **2** in hexane and acetonitrile, respectively.

Emission

The emission of **1** in hexane is structured and peaks at 393 nm, 412 nm and 429 nm, whereas in acetonitrile, the emission is broad and unstructured with a maximum at 466 nm. A striking resemblance is noticed comparing the spectrum of **1** to that of **BPB**. The emission of **BPB** in chloroform [157] ($\varepsilon_S = 4.806$ at 293 K, $\eta = 1.44293$ cP at 298 K [103]) is of analogous shape like the one presented here in hexane, but blue-shifted.

In hexane, the emission of **2** has a similar structure compared to **1**, but is also blue-shifted. The spectrum shows peaks at 349 nm, 362 nm and 376 nm. However, the fluorescence emission of **2** in acetonitrile is too weak to supply conclusive information, *i.e.* lifetime was too short to be determined with our apparatuses.

Table 7.5: Photophysical properties of **1** and **2** in hexane and acetonitrile, respectively.
ϵ_{max} denotes the molar decadic extinction coefficient at the wavelength of maximum absorbance, $\lambda_{\text{em,max}}$ the wavelength of maximum emission, ϕ the quantum yield, τ the excited-state lifetime and E_{00} the excitation energy.
n.m. stands for "not measured".

	1		**2**	
	hexane	acetonitrile	hexane	acetonitrile
ϵ_{max} /$^{\text{l}}/_{\text{mol cm}}$	75,600^{a}	74,400^{b}	48,300^{c}	47,600^{d}
$\lambda_{\text{em,max}}$ /nm	393	466	349	377
ϕ	0.22^{e}	0.59^{f}, 0.63^{g}	0.04^{h}	n.m.
τ /ns	0.74	1.66	<0.10	<0.10
E_{00} /eV	3.18	2.92	3.58	n.m.

^{a} at 365 nm ^{b} at 380 nm ^{c} at 322 nm ^{d} at 329 nm ^{e} $\lambda_{\text{exc}} = 365$ nm ^{f} $\lambda_{\text{exc}} = 355$ nm ^{g} $\lambda_{\text{exc}} = 340$ nm ^{h} $\lambda_{\text{exc}} = 321$ nm

Table 7.5 summarizes the main photophysical properties, namely the maximum molar decadic extinction coefficient, wavelength of maximum emission, quantum yield, excited-state lifetime and excitation energy, of **1** and **2** in hexane and acetonitrile, respectively. The excitation energy is given as the average of the absorption and first emission peak maxima [158].

The shortening of the conjugated system when going from the three-unit scaffold in **1** to the two-unit core in **2** leads to the observed blue-shift in the fluorescence maximum. This trend is well-known for *para*-connected phenylacetylenic compounds, such as the reference compounds **BPB** and **DPA** [157, 159]. Furthermore, whereas **BPB** is known to be strongly fluorescent ($\phi = 0.58$ in cyclohexane [159], $\phi = 0.79$ in toluene and $\phi = 0.90$ in dioxane [160]), **DPA** has only a very small fluorescence yield ($\phi = 0.006$ in cyclohexane [159]) at 25 °C. This goes hand in hand with what we observed: the molecule with the more extended π conjugation, **1**, shows a quantum yield of 0.22 in hexane and 0.59 in acetonitrile, whereas for the smaller molecule, **2**, the quantum yield was determined to be 0.04 in hexane and even indeterminable small in acetonitrile.
As far as the maximum extinction coefficients of **1** are concerned, it can be summarized that they are about one fifth higher than those known for **BPB** ($\epsilon = 62{,}000\,^{\text{l}}/_{\text{mol cm}}$ in dioxane [160]) but much higher compared to **TMPPD** with a maximum extinction coefficient of about 2,500 $^{\text{l}}/_{\text{mol cm}}$. The extraordi-

narily high extinction coefficients of molecules **1** and **2**, respectively, can be ascribed to the strong donating groups attached to the aromatic ring.
The lifetime of **1** in hexane (0.74 ns) is comparable to that of **BPB** ((0.63 ± 0.05) ns in cyclohexane [161] and 0.64 ns in dioxane [160]), whereas it is much lower compared to that of **TMPPD** (4.3 ns in cyclohexane [162, 163]).

Auristiccio and coworkers performed investigations on molecules interesting for non-linear optics and were using diphenyl acetylene derivatives symmetrically substituted in 4,4'-position, a molecule in principal resembling to our molecule **2**, but with longer alkyl chains attached to the nitrogen atoms, as reference compounds. They observed a small hypsochromic shift when going from dichloromethane to highly polar methanol for the molecule **2** derivative with the longer alkyl-chains [164].
For our molecule **2**, we observed a small bathochromic shift when going from unpolar hexane to polar acetonitrile. Similar to our findings for molecule **2**, Auristiccio observed only very weak emission in dichloromethane and methanol at room temperature [164].

Since the fluorescence of **TMPPD** is known to be quenched by specific electron acceptors [165], we made attempts to quench the fluorescence emission of **1** and **2** by adding tetracyanoethylene (TCNE). However, TCNE did not act as an effective quencher for the fluorescence of **1** and **2** presumably due to inefficient long range electron transfer between the excited fluorophores and TCNE [166, 167].

7.4 Summary

Extended Wurster-type molecules display unique properties: besides their expected well-pronounced electron-donating ability, they can also serve as electron acceptors.
Here we present our studies on the characterization of two elongated tetraalkylated *p*-phenylenediamines. We generated radical cations and analyzed them using EPR/ENDOR spectroscopy and compared the results to other Wurster-type radical cations. We were able to prove the existence of the radical anions of these *p*-phenylenediamine analogous and show EPR and ENDOR spectra thereof. EPR being a much more sensitive method than cyclic voltammetry, it is not surprising that reduction is observable by means of EPR. The cyclic voltammetric study revealed three oxidation peak potentials for each of the molecules under investigation, whereas reduction could not be observed within the experimental electrochemical window. Despite their

strongly negative reduction potential, molecules **1** and **2** have proven to be thermodynamically persistent. Additionally, we performed a photophysical characterization of the *p*-phenylenediamine analogous in an unpolar (hexane) and a polar (acetonitrile) solvent. We show absorption and emission spectra and compared them to the unsubstituted cores of the molecules investigated, namely 1,4-bis(phenylethynyl)benzene and diphenylacetylene. Due to their well-distinguishable absorption bands in their reduced, oxidized or neutral forms, respectively (see section 7.5.2 for spectra), these extended Wurster-type molecules show potential in being used as reversibly acting devices.

7.5 Supplementary Material

Our studies on the solvatochromism of molecules **1** and **2** were published with the title "Photophysics of two Prototypical Molecular-Wire Building Blocks: Solvent-Induced Conformational Dynamics?" in *ChemPhysChem*, **2010**, *11*, 1700-1710. [6]

7.5.1 Solvatochromism

With our study on the symmetrically substituted molecules **1** and **2**, we were able to contribute to the huge amount of research already performed on donor-acceptor substituted *p*-phenylenediamine derivatives. We combined different existing solvent models in order to gain information on the molecular properties both in the ground and in the excited state.

Absorption spectra of **1** are less structured than those of **2** and loose all vibronic structure and become more symmetric in polar solvents. Emission spectra of **1** in unpolar solvents show a vibronically structured pattern whereas in polar solvents, the emission becomes totally unstructured. Absorption and emission spectra of **2** become broader upon increasing solvent polarity and are strongly asymmetric. Furthermore for **2**, absorption spectra always remain broader than the emission spectra in the same solvent.

Mirror symmetry between the emission and the first absorption band could only been found in acrylates for **1** and in none of the 25 solvents investigated for **2**. For **1**, mirror symmetry is observable in propyl acetate, while it completely vanished for *e.g.* propionitrile. In cyclohexane, however, the situation for molecule **1** resembles that of molecule **2**. For **2**, absorption spectra were always found to be much broader than the mirrored emission spectrum, although they are similar close to $\tilde{\nu}_0$.

For **1**, both quantum yield and excited-state lifetime is higher than for molecule **2**. This goes hand in hand with what has been reported for **BPB** (high quantum yield) and **DPA** (low quantum yield) and attributed to the existence of a bent $\pi\sigma^*$ dark state which is accessible in the case of **DPA** [168, 169]. The low quantum yield and the short excited-state lifetime of **2** is furthermore strongly dependent on the energy of the emission transition. [6]

The solvatochromic effects were studied by means of

- empirical solvent parametrization (Catalán) and
- continuum solvent models (Lippert, Liptay).

Catalán

In order to investigate the nature and magnitude of solute–solvent interactions and distinguish between specific and non-specific solvent effects, the empirical solvent parameter scale as proposed by Catalán was applied [170]:

$$\tilde{\nu} = \tilde{\nu}^\circ + a \cdot \mathrm{SP} + b \cdot \mathrm{SdP} + c \cdot \mathrm{SA} + d \cdot \mathrm{SB} \tag{7.1}$$

where $\tilde{\nu}$ denotes the energy of the electronic transition in a given solvent and $\tilde{\nu}^\circ$ is the respective value in the gas phase, SP stands for solvent polarizability, SdP for solvent polarity, SA for solvent acidity and SB for solvent basicity [170].

We found that the response to solvent polarizability is similar for **1** and **2**. The response on solvent polarity indicates a larger dipole moment of the solute in the excited state as it increases upon going from absorption to emission. Furthermore, we found a larger response in emission thus a larger dipole moment in the excited state for molecule **1** than we found for molecule **2**. The response on solvent acidity is rather small and the influence of solvent basicity can be neglected due to the absence of hydrogen-donating groups in **1** and **2**. [6]

Lippert

Using a spherical approximation of the solute molecule and parallel dipole moments, the Lippert model accounts for dipole–dipole and solute dipole–solvent polarizability interactions [171]:

$$\tilde{\nu}_{\mathrm{a}} = \tilde{\nu}_{\mathrm{a}}^{\circ} - \frac{2\mu_{\mathrm{g}}(\mu_{\mathrm{e}}^{\mathrm{FC}} - \mu_{\mathrm{g}})}{hcr^3} \cdot f(\varepsilon) - \frac{(\mu_{\mathrm{e}}^{\mathrm{FC}} - \mu_{\mathrm{g}})^2}{hcr^3} \cdot f(n^2) \tag{7.2}$$

$$\tilde{\nu}_{\mathrm{f}} = \tilde{\nu}_{\mathrm{f}}^{\circ} - \frac{2\mu_{\mathrm{e}}(\mu_{\mathrm{e}} - \mu_{\mathrm{g}}^{\mathrm{FC}})}{hcr^3} \cdot f(\varepsilon) + \frac{(\mu_{\mathrm{e}} - \mu_{\mathrm{g}}^{\mathrm{FC}})^2}{hcr^3} \cdot f(n^2) \tag{7.3}$$

where $f(x) = (x-1)/(2x+1)$, μ_x refers to the relaxed *g*round or *e*xcited state dipole moment and μ_x^{FC} to their Franck Condon counterparts. h denotes Planck's constant, c the velocity of light, and r the Onsager cavity radius. [6]

Absorption data are well described by the Lippert model, however significant systematic deviations arise when applying the model to the fluorescence data. [6]

Liptay

The Liptay approach accounts for dipole–dipole, solute dipole–solvent polarizability, solute polarizability–solvent dipole and polarizability–polarizability interactions. It assumes parallel ground and excited state dipole moments and equalizes ground and excited state solute polarizability [172]:

$$\tilde{\nu}_{\mathrm{a}} = \tilde{\nu}_{\mathrm{a}}^{\circ} - \frac{\mu_{\mathrm{g}}(\mu_{\mathrm{e}}^{\mathrm{FC}} - \mu_{\mathrm{g}})}{hc} \cdot \frac{g(\varepsilon)}{(1-g(\varepsilon)\alpha)} - \frac{(\mu_{\mathrm{e}}^{\mathrm{FC}} - \mu_{\mathrm{g}})^2 + 2hcD}{2hc} \cdot \frac{g(n^2)}{(1-g(n^2)\alpha)} \tag{7.4}$$

$$\tilde{\nu}_{\mathrm{f}} = \tilde{\nu}_{\mathrm{f}}^{\circ} - \frac{\mu_{\mathrm{e}}(\mu_{\mathrm{e}} - \mu_{\mathrm{g}}^{\mathrm{FC}})}{hc} \cdot \frac{g(\varepsilon)}{(1-g(\varepsilon)\alpha)} + \frac{(\mu_{\mathrm{e}} - \mu_{\mathrm{g}}^{\mathrm{FC}})^2 - 2hcD}{2hc} \cdot \frac{g(n^2)}{(1-g(n^2)\alpha)} \tag{7.5}$$

where D denotes the dispersion interaction between solute and solvent, α is the solute polarizability and $g(x) = 2r^{-3}f(x)F(x, A)$ is the modified solvent function, with x taking either n^2 or ε, accounting for the shape and charge distribution of the reaction field.

The dipole moments are closely related to the values of the Onsager radius, whose size is difficult to estimate. Our analysis was thus limited to parameters which remain constant upon changing the Onsager radius:

- Solute polarizability α: We found that compound **1** is more polarizable due to its larger π system in comparison to compound **2**.
- Dispersion interaction term $2D/r^3$: We found that the solvent shift induced by D is identical for compounds **1** and **2**, respectively.

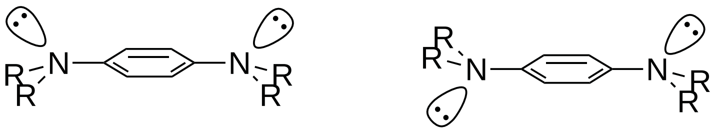

cis *trans*

$\mu > 0$ $\mu = 0$

Figure 7.15: *cis* and *trans* forms of the parent tetraalkyl-*p*-phenylenediamine.

- Relaxed μ_x and Franck Condon dipole moments μ_x^{FC}: We could prove that the dipole moment changes occur mostly in the course of solvent relaxation from the Franck Condon state.

The relative dipole moment changes leading to solvatochromism in absorption were found to be the same for molecules **1** and **2**, respectively. However, as far as fluorescence is concerned, the changes are more pronounced for molecule **1**. [6]

The ground state dipole moments of **1** and **2** are comparable to those of *p*-phenylenediamine [173]. For *p*-phenylenediamine, the dipole moment originates from the *cis* form while the *trans* form does not show any effective dipole moment at all. As the torsional barriers in **1** and **2** are small in the ground state and large in the excited state, the molecules will remain in their more stable planar configuration after excitation and subsequent solvent relaxation. The increase of the dipole moment when going from the ground to the excited state points to a more stable *cis* form than *trans* form in the excited state. [6]

7.5.2 Additional Spectra Representations

Figures 7.16 and 7.17 show the absorption spectra of **1** before and after oxidation and reduction, respectively.
Figures 7.18 and 7.19 show the absorption spectra of **2** before and after oxidation and reduction, respectively.

Figures 7.20 and 7.21 show the absorption and emission spectra of **1** in hexane and acetonitrile, respectively, in the transition dipole moment representation.
Figures 7.22 and 7.23 show the absorption and emission spectra of **2** in hexane and acetonitrile, respectively, in the transition dipole moment representation.

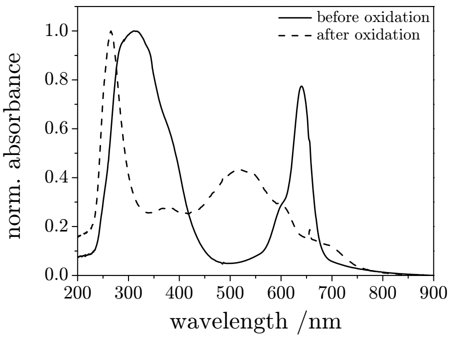

Figure 7.16: Absorption spectra of **1** in HFP before and after oxidation with PIFA/TFA.

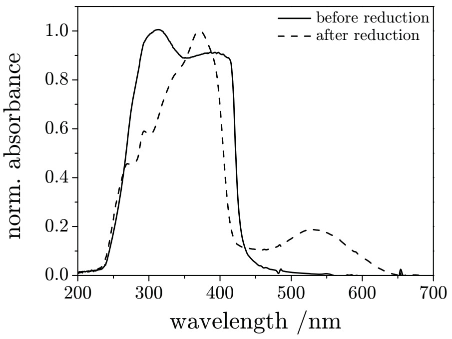

Figure 7.17: Absorption spectra of **1** in DME before and after reduction with K metal mirror.

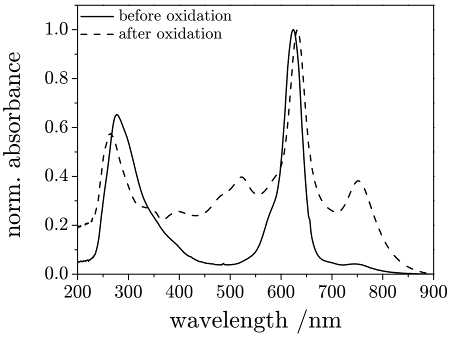

Figure 7.18: Absorption spectra of **2** in HFP before and after oxidation with PIFA/TFA.

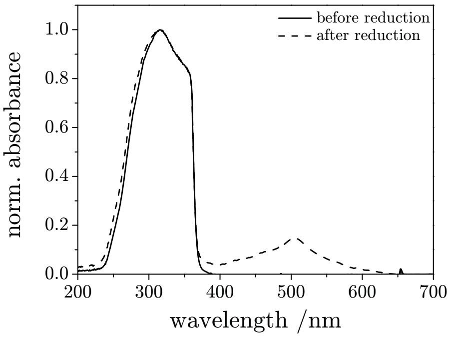

Figure 7.19: Absorption spectra of **2** in DME before and after reduction with K metal mirror.

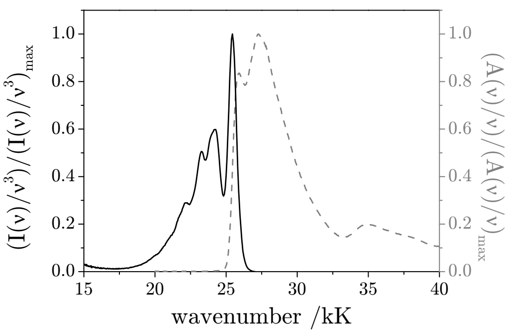

Figure 7.20: Absorption and emission spectra of **1** in hexane in the transition dipole moment representation [174].

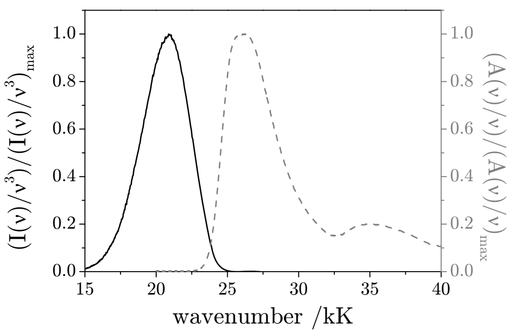

Figure 7.21: Absorption and emission spectra of **1** in acetonitrile in the transition dipole moment representation [174].

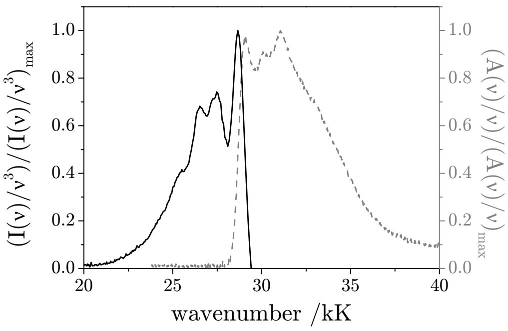

Figure 7.22: Absorption and emission spectra of **2** in hexane in the transition dipole moment representation [174].

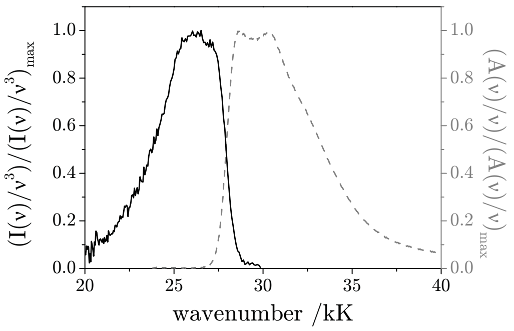

Figure 7.23: Absorption and emission spectra of **2** in acetonitrile in the transition dipole moment representation [174].

Chapter 8

Non-Planar Push-Pull Chromophores

Non-planar push-pull chromophores featuring intense charge-transfer bands with end-absorptions in the near infrared are gaining increasing importance as potential candidates for optoelectronic devices. While non-planar push-pull chromophores bear the advantage of being more easily soluble and sublimable as well as less aggregating compared to their well-investigated planar counterparts, charge-transfer interactions in non-planar molecules are more complex. Steric constraints in these molecules often hinders effective π conjugation and complicates straightforward predictions on their properties. [175]

Therefore, optical spectroscopy together with EPR spectroscopy were applied in order to study the effects of different or additional acceptor or donor moieties, respectively, on the optical, magnetic and electronic properties of these molecules. A variety of compounds with different acceptor or donor strength, respectively, *i.e.* compounds featuring stronger or additional acceptor groups or additional donor groups, were selected for this study. In the following, optical spectra are discussed upon referring to published electrochemical data. EPR spectra enabled us to shed light on the electron distribution in these molecules. The compounds under investigation shall be treated within four sections in the sequence of increasing acceptor strength:

- donor-substituted 1,1,4,4-tetracyanobuta-1,3-dienes (TCBDs)
- donor-substituted 7,7,8,8-tetracyanoquinodimethanes (TCNQs)
- donor-substituted 2,3,5,6-tetrafluoro-7,7,8,8-tetracyanoquinodimethanes (F_4-TCNQs)
- donor-substituted octacyano[4]dendralenes

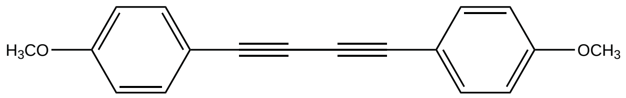

Figure 8.1: Molecular structure of **3**.

8.1 Experimental

The compounds under investigation in this chapter (compounds **1**-**26**) were supplied by the group of Prof. Dr. Diederich from ETH Zürich.
Compounds **1** and **2**, whose analysis was already described in chapter 7, as well as compound **3** (synthesis described in [176], molecular structure shown in figure 8.1) served, among others, as precursor substances for the synthesis of these push-pull chromophores. Molecules **1** and **2** got "activated" for the reaction with TCBD by means of substitution with strong donor groups. This "activation" facilitated further synthesis, while reaction with TCBD and molecule **3** required more drastic reaction conditions [149].
Syntheses of the compounds under investigation have mostly been described by Dr. Kivala in his PhD thesis [177].

All samples were prepared by dissolving a little amount of the substance in the particular solvents. In order to remove oxygen, all samples were deaerated for 10 minutes by bubbling with argon. Much attention was drawn to the usage of pure and dry solvents.
Dichloromethane (99.8 %, Rotidry) and acetonitrile (spektranal. grade) were distilled and dried over molecular sieves, 1,4-dioxane (99.8 %, HPLC unstab.), toluene (>99 %, purum) and cyclohexane (>99.5 %, puriss. p. a.) were used as received.
Absorption spectra were recorded on a Shimadzu UV-3101 PC Spectrophotometer and absorption spectra were mostly normalized to the maximum of their CT band. Fluorescence spectra were recorded on a FluoroMax-2 ISA® Jobin YVON-SPEX Instruments Spectrometer with slit widths of 2 nm.

The experimental conditions for recording EPR/ENDOR spectra are discussed in the respective sections, as experimental parameters were optimized for each set of experiments.

8.2 Donor-Substituted Tetracyanobutadienes

Unimolecular donor/acceptor systems featuring intense intramolecular charge-transfer interactions are of interest for potential applications in optoelectronic devices. Among this class of molecules, donor-substituted 1,1,4,4-tetracyanobuta-1,3-dienes (TCBDs) are already applied in silicon-organic-hybrid waveguides as they can advantageously be deposited as high-optical quality amorphous films. [175]

In this section, monomeric donor-substituted TCBDs (compounds **4-10**), oligomeric donor-substituted TCBDs (compounds **11-14**) and oligomeric donor-substituted TCBDs with triphenylamine core (compounds **15-16**) are discussed. The aim of the present study was to establish their optical properties in terms of absorption and emission characteristics and to investigate how these properties can be tuned upon changing the molecules' structure. Furthermore, it addresses the question, to which extent donor substitution alters the electron transfer properties of the TCBD moiety.

While already the monomeric donor-substituted TCBDs show strong intramolecular charge-transfer interactions, oligomeric or dendritic donor-substituted TCBDs show even more pronounced properties, *i.e.* oligomeric donor-substituted TCBDs can undergo several reversible redox steps. Two dendritic molecules were thus selected to be analyzed by means of EPR with regard to the characterization of higher spin states.

8.2.1 Monomeric Donor-Substituted TCBDs

The molecular structures of the monomeric donor-substituted TCBDs under investigation (compounds **4** to **10**) are shown in figure 8.2.

Optical Properties

Compound **4** is known from X-ray analysis to be non-planar, but with each dicyanovinyl moiety and the adjacent donor-substituted phenyl ring to be co-planar such as to assure that intense intramolecular CT bands are observable [10]. Due to the presence of even two dimethylamino moieties, the observed CT bands are even more intense. The CT band shifts from 484 nm in cyclohexane to 508 nm in 1,4-dioxane, to 514 nm in toluene, to 518 nm in acetonitrile and even to 530 nm in dichloromethane (*cf.* figure 8.4). A strong

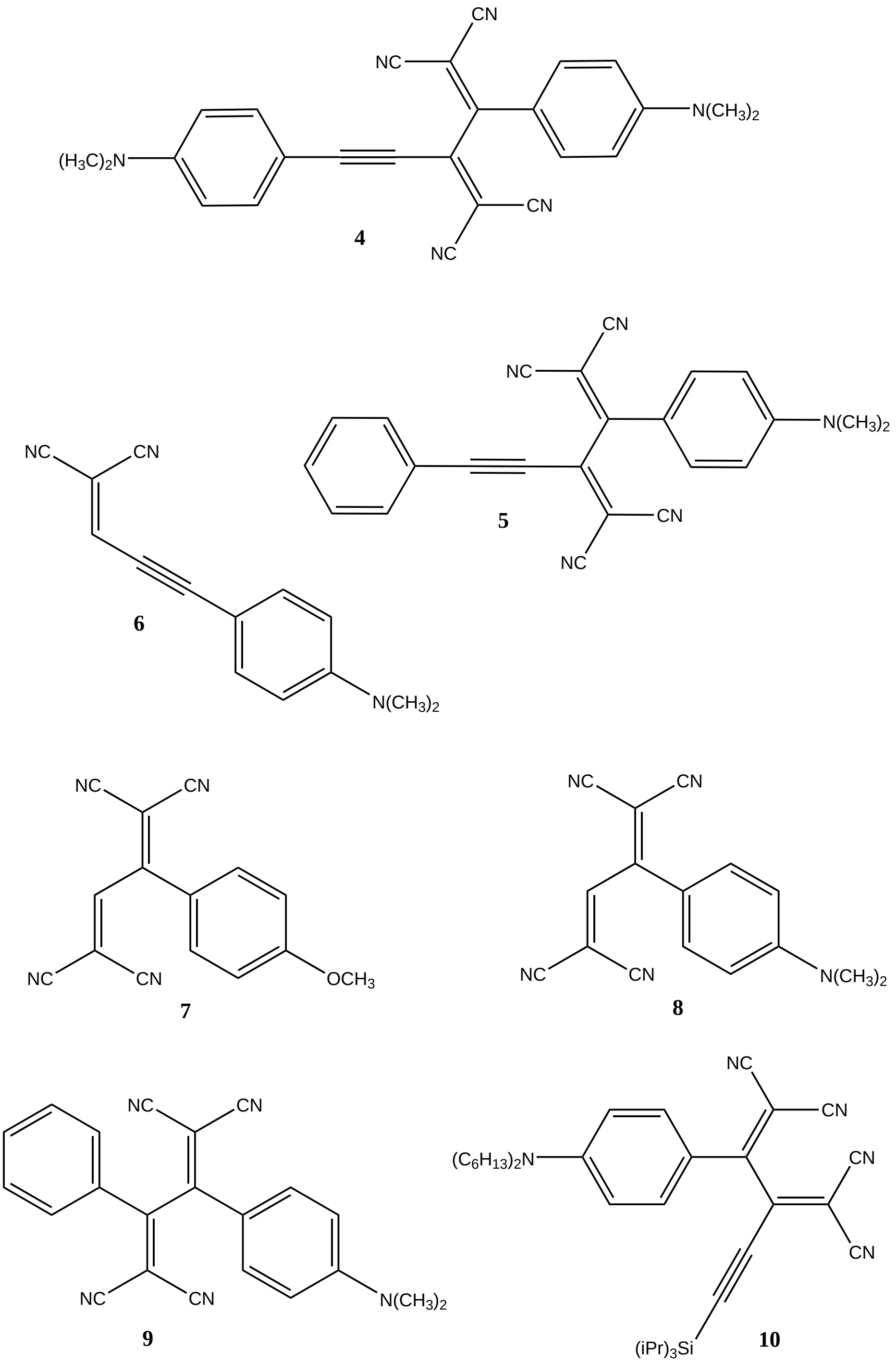

4

5

6

7

8

9

10

Figure 8.2: Molecular structures of **4**, **5**, **6**, **7**, **8**, **9** and **10**.

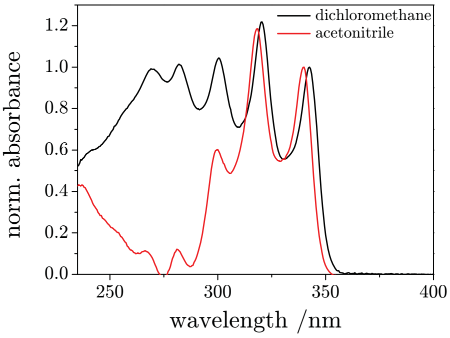

Figure 8.3: Absorption spectra of **3** in dichloromethane and acetonitrile, respectively.

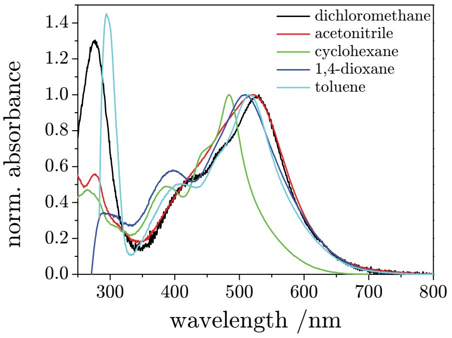

Figure 8.4: Absorption spectra of **4** in dichloromethane, acetonitrile, cyclohexane, 1,4-dioxane and toluene, respectively.

shift from 477 nm in hexane to 526 nm in chloroform with a molar decadic extinction coefficient of $\epsilon = 38{,}100\,{}^{1}\!/_{\mathrm{mol\ cm}}$ is already reported in [7, 10]. No fluorescence was observable in the solvents investigated.

Compound **5** is structurally related to compound **4**. The only difference is one missing dimethylamino moiety on one phenyl ring. The sample is well soluble in acetonitrile and dissolved in hexane after one hour. The absorption spectrum shows a structured pattern in hexane with peaks at 363 nm, 398 nm and 434 nm and one less structured CT band at 450 nm in acetonitrile ($\epsilon = 23{,}000\,{}^{1}\!/_{\mathrm{mol\ cm}}$), respectively (*cf.* figure 8.5). Again, this compound does not fluoresce.

Compound **6** is actually a dicyano-vinyl molecule [10] which shall be treated within this chapter as it shows similar properties. The absorption spectrum of compound **6** shows one CT band at 468 nm in acetonitrile and at 477 nm in dichloromethane (*cf.* figure 8.6), respectively. The pattern of this spectrum can also be recognized in the spectra of the donor-substituted TCBDs. Again, no fluorescence could be observed.

Compound **7** is a *p*-anisyl substituted TCBD which has been synthesized starting from compound **3** as described in [149]. The *p*-anisyl moiety is a weaker electron donor compared to the dimethylamino moiety. The first electron reduction potential of compound **7** lies at -0.56 V in CH_2Cl_2 *vs.* Fc^+/Fc [149]. The CT band of compound **7** appears at 417 nm in acetonitrile and at 443 nm in dichloromethane (*cf.* figure 8.7). Again, it does not fluoresce.

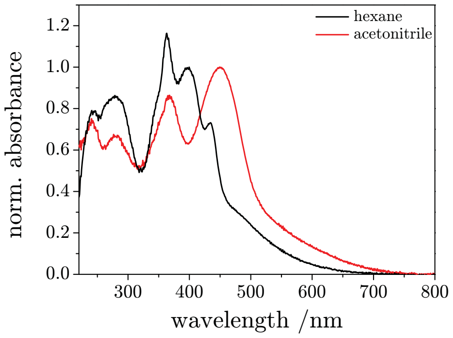

Figure 8.5: Absorption spectra of **5** in hexane and acetonitrile, respectively.

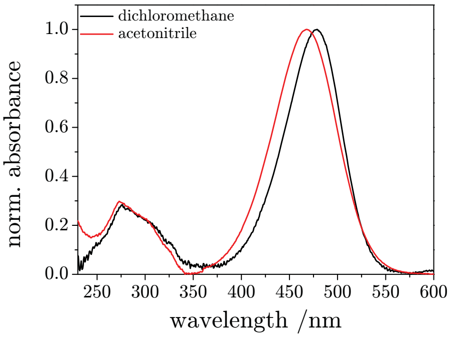

Figure 8.6: Absorption spectra of **6** in dichloromethane and acetonitrile, respectively.

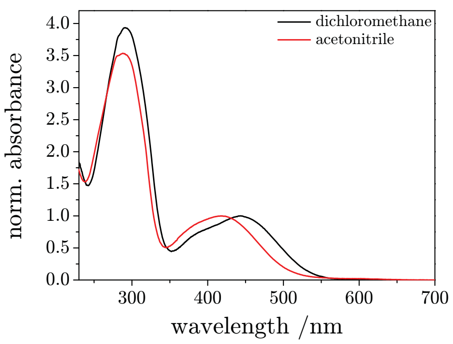

Figure 8.7: Absorption spectra of **7** in dichloromethane and acetonitrile, respectively.

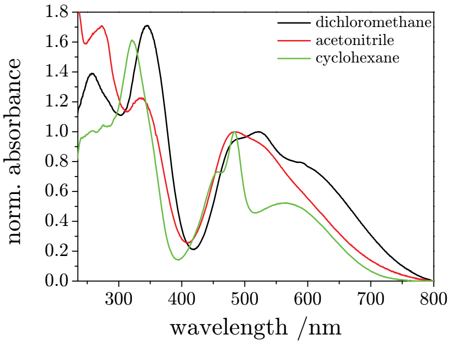

Figure 8.8: Absorption spectra of **8** in dichloromethane, acetonitrile and cyclohexane, respectively.

Compound **8** has the same structure as compound **7** only differing in the donor moiety, which is again the dimethylamino group in this case. The first one-electron reduction potential of compound **8** is known to lie already at -0.69 V in CH_2Cl_2 *vs.* Fc^+/Fc which shows that compound **8** acts as strong electron acceptor. Compared to compound **7**, the first one-electron reduction potential is thus shifted to more negative potentials by 130 mV [149]. The absorption spectrum of compound **8** shows a broad CT band with peaks at 483 nm and 566 nm in cyclohexane, 486 nm in acetonitrile, and at 521 nm with a shoulder at 586 nm in dichloromethane, respectively. Again, compound **8** does not show fluorescence in the solvents investigated.

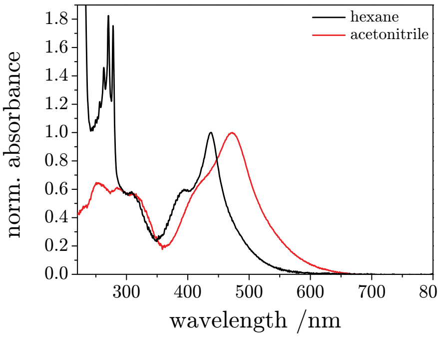

Figure 8.9: Absorption spectra of **9** in hexane and acetonitrile, respectively.

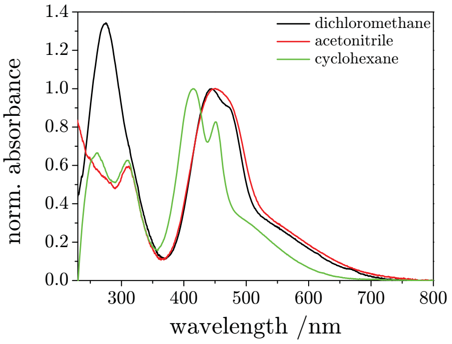

Figure 8.10: Absorption spectra of **10** in dichloromethane, acetonitrile and cyclohexane, respectively.

Compound **9** is similar to compound **8** as the only difference is one additional phenyl ring connected to the TCBD moiety. The sample is a glaring red powder. Its absorption spectrum shows CT bands at 437 nm in hexane and at 473 nm in acetonitrile ($\epsilon = 25{,}000\,{}^{1}\!/_{\text{mol cm}}$), respectively (*cf.* figure 8.9). Compound **9** is non-fluorescent.

Compound **10** serves as educt for preparation of dendritic TCBDs [178]. Its absorption spectrum shows CT bands at 415 nm in cyclohexane, 443 nm in dichloromethane and 450 nm in acetonitrile, respectively (*cf.* figure 8.10). Compound **10** did not show any fluorescence.

It can be summarized that donor-substituted TCBDs show intense CT bands, despite strong distortion out of planarity *via* rotation around the central single bond of the TCBD moiety [149]. Crystal structures indicate preferred s-*trans* conformation of the TCBD moiety as shown for molecules **4**, **7** and **8** in [10, 149].

EPR/ENDOR studies allowed to establish the extent to which this nonplanarity hinders effective π delocalization. It could be shown for the parent radical anions that the type of donor substitution (dialkylamino or *p*-anisyl) does not alter the spin distribution as the spin resides mainly on one TCBD moieties in radical anions. *Vice versa*, for the parent radical cations, the spin resides mainly on one donor moiety. EPR spectra and spin distributions were found to be quite similar for the molecules investigated. [178]

8.2.2 Oligomeric Donor-Substituted TCBDs

Oligomeric or dendritic donor-substituted TCBDs are made up of three or four D–A arrays which are attached to a central benzene ring. The individual donor and acceptor moieties were shown to behave as independent electroactive centers [179] and are able to take up and accommodate an exceptional number of electrons. Dendritic donor-substituted TCBDs of such kind thus have potential in being used as "molecular batteries" with exceptional storage capacity. [7, 180]
Four representatives of this class (compounds **11-14**, shown in figures 8.11 and 8.12, respectively) were investigated in terms of their photophysical behavior. Furthermore, highly charged anions of compounds **11** and **13** were analyzed using EPR spectroscopy, as elucidated later in this section.

Optical Properties

In compound **11**, three D–A arrays are connected to a central benzene ring *via* an ethyn-1,2-diyl bridge. The spacer was used to enlarge the distance between each of the D–A arrays and therefore shift their reduction potentials in a narrower range. The absorption spectrum of compound **11** shows an intense and broad CT band peaking at 457 nm in acetonitrile and at 460 nm in dichloromethane. The CT band has a long tail reaching into the near infrared region (*cf.* figure 8.13). Compound **11** did not show fluorescence. While oxidation is reported to happen in one multi-electron transfer, reductions happen in several reversible one-electron transfer steps where each TCBD moiety can take up two electrons. This makes a total of six electrons for compound **11** [180]. As has been shown by EPR experiments, spin and charge in radical anions of these oligomeric donor-substituted TCBDs are confined to one acceptor moiety while spin transfer between acceptor units was ruled out. [178]

Compound **12** is a black solid and structurally related to compound **11** as the only difference is the alkyl group of the dialkylamino group connected to the phenyl ring (CH_3 as for compound **12** and for solubility reasons C_6H_{13} for compound **11**). Compound **12** is well soluble in acetonitrile but not soluble in hexane. The absorption spectrum of compound **12** shows a broad CT band at 450 nm ($\epsilon = 77{,}000\,{}^{1}\!/_{\mathrm{mol\ cm}}$) in acetonitrile with a broad shoulder reaching in the near infrared region similar to compound **11** (*cf.* figure 8.14).

Compound **13** features four D–A arrays connected to a central benzene

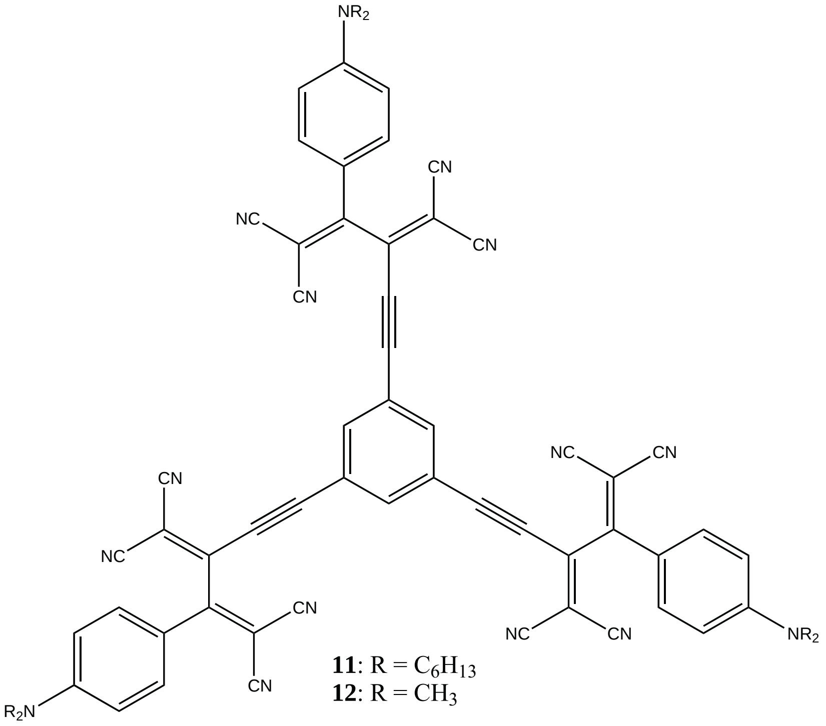

11: R = C_6H_{13}
12: R = CH_3

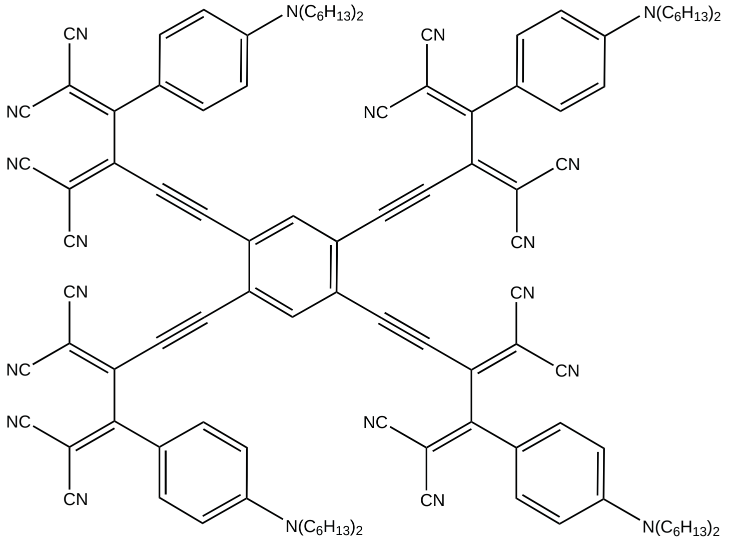

13

Figure 8.11: Molecular structures of **11**, **12** and **13**.

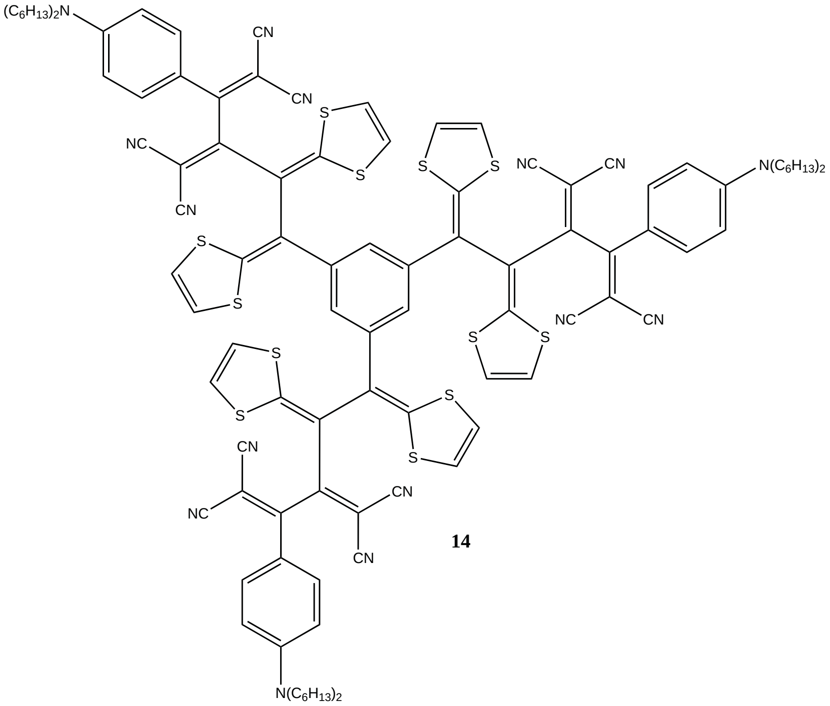

14

Figure 8.12: Molecular structure of **14**.

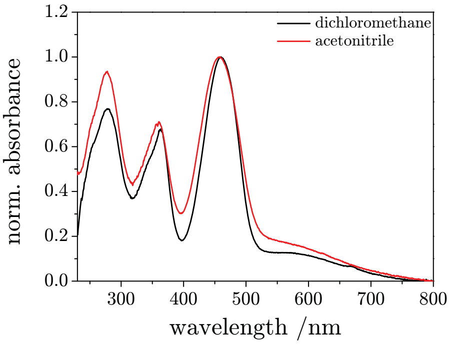

Figure 8.13: Absorption spectra of **11** in dichloromethane and acetonitrile, respectively.

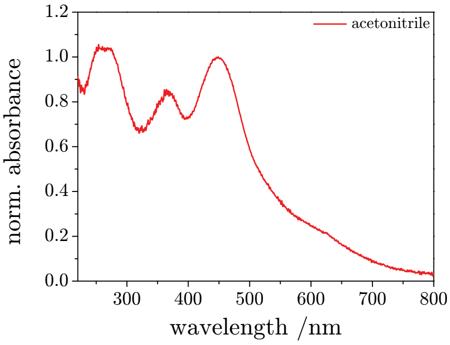

Figure 8.14: Absorption spectrum of **12** in acetonitrile.

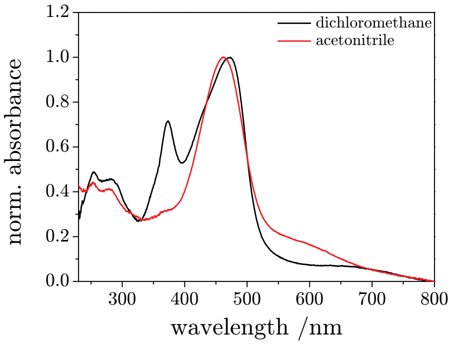

Figure 8.15: Absorption spectra of **13** in dichloromethane and acetonitrile, respectively.

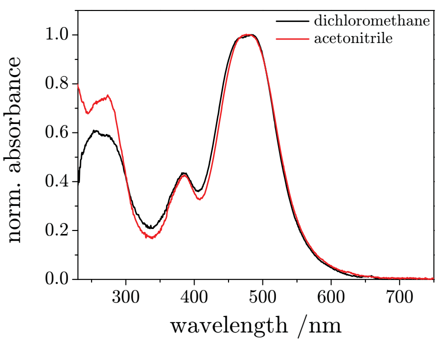

Figure 8.16: Absorption spectra of **14** in dichloromethane and acetonitrile, respectively.

ring. Its absorption spectrum shows CT bands at 461 nm in acetonitrile and at 470 nm in dichloromethane with again broad shoulders reaching into the near infrared region of the spectrum (*cf.* figure 8.15). EPR experiments revealed similar conclusions as already for compound **11**. Spin and charge are confined to one TCBD moiety as for radical anions and to one dialkylamino moiety as for radical cations. These observations were explained in terms of counterion effects and in terms of non-planarity of the π system which goes hand in hand with limited π delocalization [178].

Compound **14** is a black-metallic solid featuring not only dialkylamino moieties but as well tetrathiafulvalene (TTF) moieties acting as strong electron donors. The absorption spectrum shows an intense CT band at 473 nm for acetonitrile and at 484 nm for dichloromethane, respectively (*cf.* figure 8.16). The EPR spectrum of the radical cations of compound **14** shows an unresolved signal which is indication for spin and charge being present at sulfur atoms. Furthermore, the first oxidation potential is reported to be +0.41 V *vs.* Fc^+/Fc in CH_2Cl_2 and thus much lower than those reported for compound **11** (+0.88 V *vs.* Fc^+/Fc in CH_2Cl_2) and compound **13** (+0.89 V *vs.* Fc^+/Fc in CH_2Cl_2), respectively. [178, 180]

Magnetic Properties

In order to investigate highly charged species of this dendrimer type of molecules, a series of EPR experiments was undertaken where the sample was subjected to exhaustive reduction upon contact with a K metal mirror.

Experiments were performed with compound **11**, a dendritic molecule with three D–A arrays and with compound **13**, the analogon with four D–A arrays. As compound **11** was expected to give promising results due to its high symmetry (compare as well [51]), the following analysis is mainly devoted to compound **11**. It should, however, be noted that analogous observations were made for compound **13**.

All samples were prepared under high vacuum in MTHF, which had been refluxed, distilled and stored over a Na/K alloy. MTHF bears the advantage to freeze in a glassy matrix and is thus suited for EPR measurements in frozen solutions. Radical ions were generated by means of K metal mirror contact under high vacuum and at 190 K in an isopropanole/dry ice bath. Sample preparation thus followed the guidelines described in subsection 4.2.1. As the idea was to generate high spin states, multiple redox processes of increasing duration, *i.e.* contacts of the solution with the K metal mirror, were performed.

Measurements at 220 K were performed on our Bruker ESP300E X-band spectrometer, while low-temperature measurements were performed in liquid nitrogen on our MiniScope MS 100 X-band spectrometer (Magnettech). Using both instruments simultaneously, one being thermostatted to 220 K and the other to 77 K, allowed consecutive measurements without any delay due to cooling-down or heating-up of the cavity. UV/Vis spectra were recorded on our TIDAS UV/Vis/NIR spectrometer (J&M).
A total of five series were performed in order to assure the reproducibility of the results. Prior to any contact with the K metal mirror, EPR and absorption spectra were recorded. No EPR signal was observed in case of the neutral species and the absorption spectrum resembled that in dichloromethane and acetonitrile (*vide supra*). Reductions were performed in following steps:

- 1 short contact with the K metal mirror
- +1 additional minute
- +5 additional minutes
- +10 additional minutes
- +1 additional hour
- +over-night contact with the K metal mirror (approx. 14 hours)
- +1 additional day (approx. 24 hours)

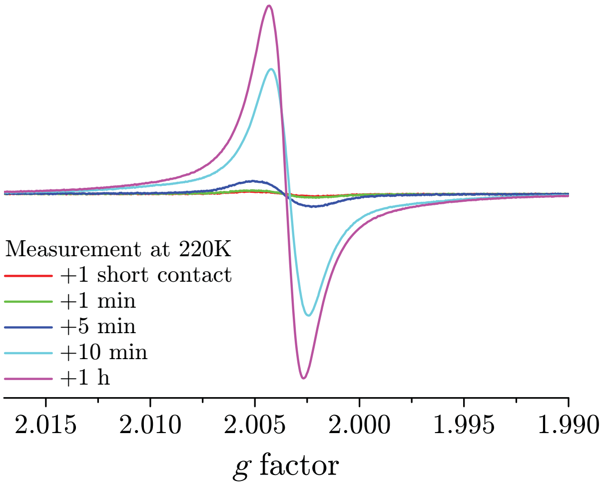

Figure 8.17: EPR spectra of **11** at various stages in the reduction process on a g factor scale at 220 K.

After each of these steps, EPR spectra at 220 K and at 77 K, respectively, and a UV/Vis spectrum were recorded, before putting the sample back into the isopropanole/dry ice bath for the next reduction step. As soon as a fading of the metal mirror became visible (usually after the first four steps), the mirror was re-activated after each reduction step under high vacuum in the sample tube *via* re-sublimation: therefore, the mirror was carefully heated with the flame of a Bunsen burner and re-condensed to where the sample tube was cooled with liquid nitrogen.

After the first reductions, no noteworthy increase in the intensity of the EPR signal at 220 K was observed. The intensity of the EPR signal slowly increases after the 5 minutes and drastically increases after the 10 minutes and the one hour reduction steps. The observations made by UV/Vis absorption spectroscopy are in line with those made by EPR: after the 10 minutes reduction step an absorption band arises at about 691 nm, which can be attributed to the radical anion of **11**. This absorption band gets more intense after the 1 hour reduction step. Additionally, the absorption band at 454 nm is shifted to 439 nm.

However, upon further reduction, the intensities of the EPR spectrum and the low-energy absorption band, respectively, decrease. After the over-

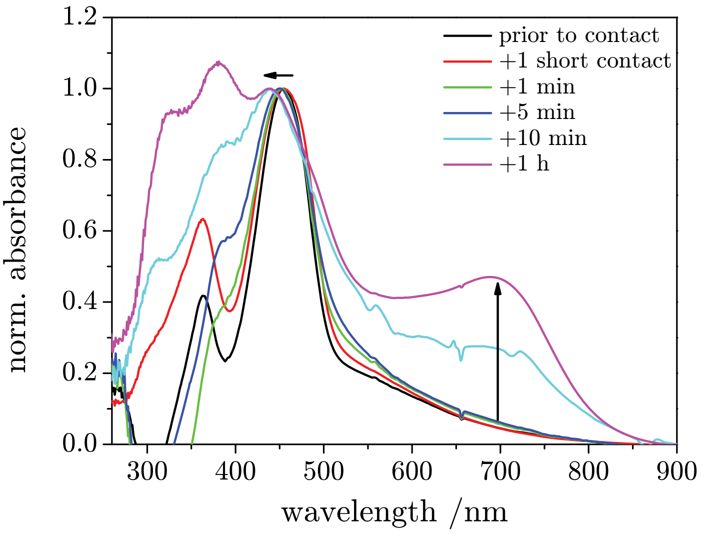

Figure 8.18: Absorption spectra of neutral **11** and at various stages in the reduction process.

night reduction process, the EPR signal completely vanishes. Furthermore, the sample solution turned from deep greenish-brown into a colorless solution with visible undissolved particles, presumably due to the crystallization of salts.

The EPR experiments at 77 K drew a similar picture: A small signal appears after the 5 minutes reduction step, which gets more intense after the 10 minutes and the 1 hour reduction steps, respectively. The EPR spectra recorded in the frozen matrix, however, show the central, intense but unresolved line but with two additional lines at lower and higher field values, respectively. These lines *could* be attributed to the higher spin states. However, measurements at half-field did not give a signal, which could either be explained in terms of a too low triplet concentration or *could* indicate that no triplets but anisotropy is observed.

In order to reveal the origin of these additional bands, the experimental spectra were simulated using WINEPR SimFonia software from Bruker and the interspin distance between the charge bearing moieties was calculated by means of molecular mechanics calculations in Chem3D. Taking the interspin distance of 10 $\AA$ as a basis and assuming that the additional bands in the spectra arise from triplet states, simulation with different D factors gave ev-

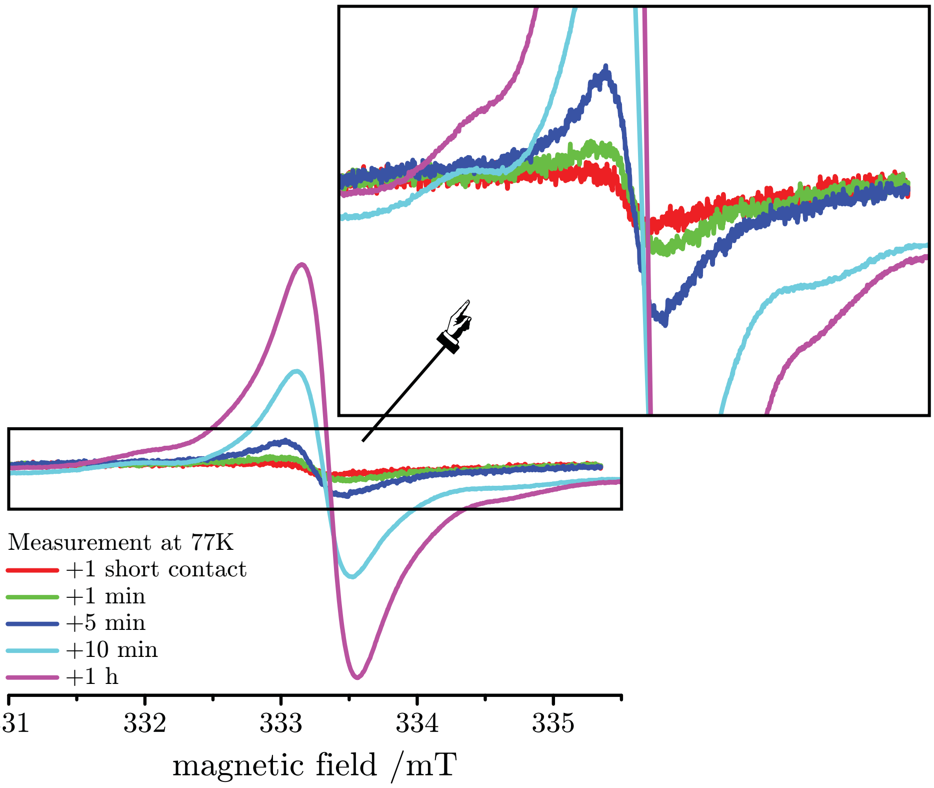

Figure 8.19: EPR spectra of **11** at various stages in the reduction process at 77 K.

idence that the observed spectra are not derived from triplet states but most likely from a mixture of species.

The conclusion which can be drawn based on these observations is that highly charged species have been generated by means of the multiple reduction processes. However, with a certain concentration of highly charged species being reached, the sample particles "aggregated" and did not dissolve anymore. The characterization of higher spin states is thus limited by these solubility issues.

8.2.3 Oligomeric Donor-Substituted TCBDs with Triphenylamine Core

Two molecules of the class of oligomeric donor-substituted TCBDs with triphenylamine core (**15** and **16** – for molecular structures see figure 8.22) were investigated in terms of their absorption and emission characteristics.

Optical Properties

Compound **15** consists of a triphenylamine core with three D–A arrays connected to it *via* ethyn-1,2-diyl bridges. The absorption spectrum of this deep-colored solid shows a broad CT band with a maximum at 462 nm and a shoulder at 522 nm in dichloromethane and at 463 nm in acetonitrile with a shoulder similar to the observations in dichloromethane (*cf.* figure 8.20).

Compound **16** has the same triphenylamine core like compound **15** but with six D–A arrays connected *via* 1-(buta-1,3-diyn-1-yl)-3,5-diethynylbenzene bridges. The sample is as well a deep-colored solid but insoluble in acetonitrile. The absorption spectrum in dichloromethane of compound **16** features a CT band at 456 nm with a long tail into the red region (*cf.* figure 8.21).

For the generation of radical cations, chemical oxidations as described in subsection 4.3.1 were applied. As the triphenylamine core is oxidizable, the EPR spectrum of the radical cation of **15** is dominated by the ^{14}N core and consists of three lines, *i.e.* the expected pattern (similar to other dendritic donor-substituted TCBDs) is only observable for a short period of time. In the case of compound **16**, the EPR spectra immediately showed three signals resulting from the central ^{14}N atom which was explained in terms of more distant electron-withdrawing TCBD groups compared to **15**. [178]

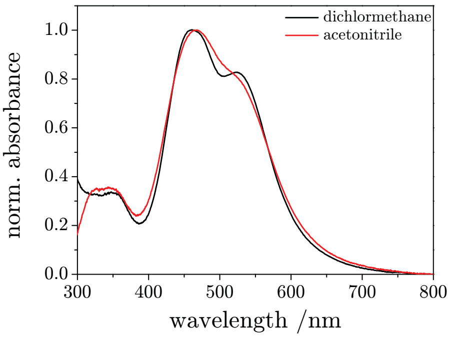

Figure 8.20: Absorption spectra of **15** in dichloromethane and acetonitrile, respectively.

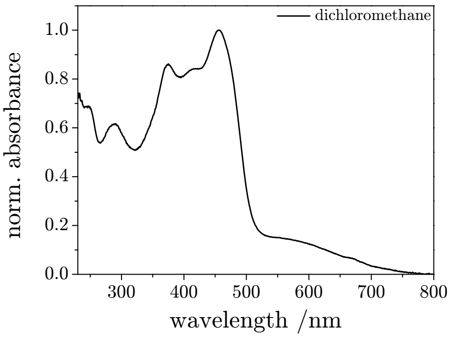

Figure 8.21: Absorption spectrum of **16** in dichloromethane.

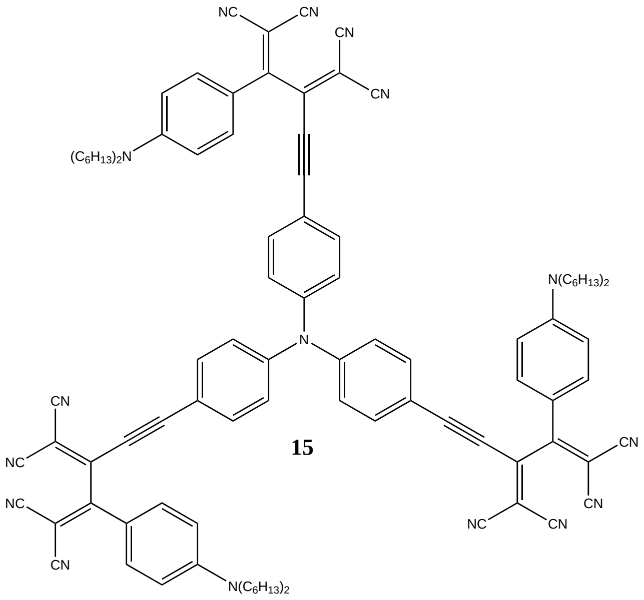

15

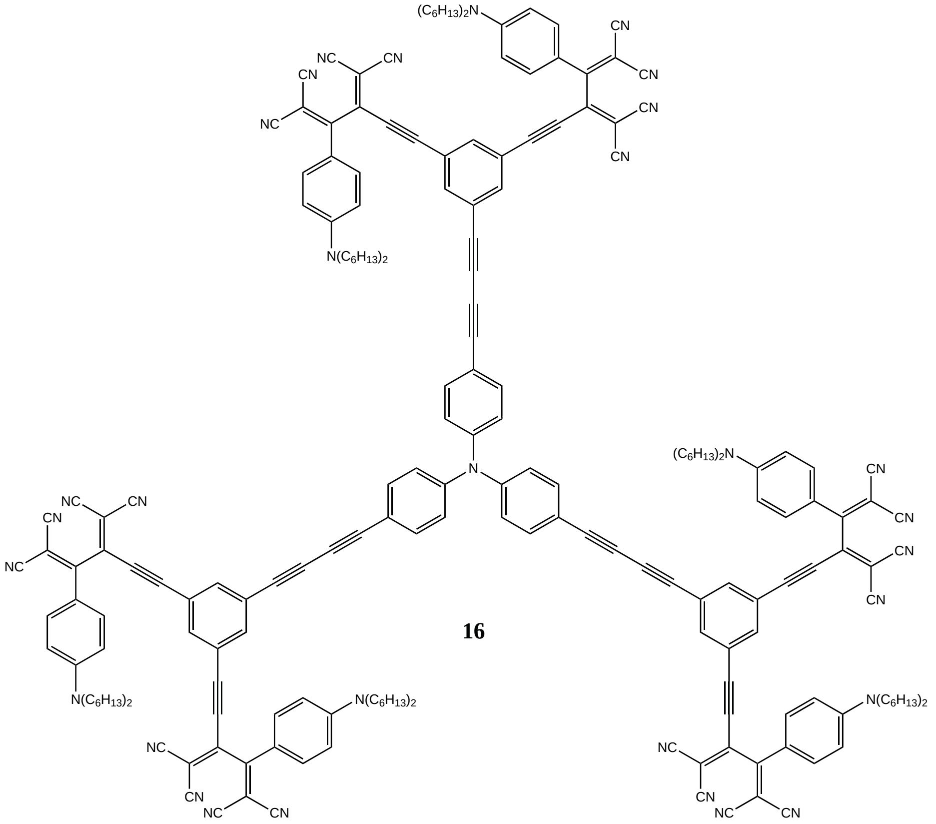

16

Figure 8.22: Molecular structures of **15** and **16**.

8.3 Donor-Substituted Tetracyanoquinodimethanes

Donor-substituted 7,7,8,8-tetracyanoquinodimethanes (TCNQs) constitute another class of compounds for potential application in optoelectronic devices. They feature intense intramolecular charge-transfer interactions whose absorption bands appear bathochromically shifted compared to those of donor-substituted TCBDs which were described in the previous section. Despite substitution with donors, the compounds presented in this section (compounds **17-21**, for molecular structure see figure 8.23) remain strong acceptors and show reversible electron uptake abilities. As environmentally stable acceptors, these molecules have gained importance as alternative p-type dopants.

Compounds **17-21** are black solids which are well soluble in polar solvents, *e.g.* acetonitrile and only hardly soluble in unpolar solvents, *e.g.* hexane. Interestingly, compounds **17** and **20** were found to fluoresce in hexane. Fluorescence spectroscopy being a very sensitive method, it was possible to record emission spectra even though only very little amounts of the substances dissolved in hexane.

8.3.1 Optical Properties

Compound **17** is a reddish-black solid which dissolves well in polar solvents, *e.g.* acetonitrile. Dissolving it in hexane required warming the solution to 50 °C and the usage of an ultrasonic bath. The absorption spectrum shows two CT bands in acetonitrile, namely at 409 nm (ϵ = 28,000 $^1/_{\text{mol cm}}$) and at 742 nm (ϵ = 21,000 $^1/_{\text{mol cm}}$) with an end-absorption reaching in the near infrared region. It was not possible to determine the extinction coefficient in hexane, as the sample was hardly soluble in unpolar solvents. However, the absorption spectrum that could be recorded from what had dissolved in hexane shows peaks at 392 nm and at 708 nm, respectively (*cf.* figure 8.24*). Interestingly for this type of molecules, compound **17** gave a fluorescence spectrum in hexane (*cf.* figure 8.25) upon excitation at 392 nm or 370 nm, respectively. The slightly structured emission with a maximum at 461 nm does not depend on the excitation wavelength. The excitation spectrum recorded at the wavelength of maximum emission ($\lambda_{\text{max}} = 461$ nm) is congruent with the absorption spectrum.

---

* Note that the solution in hexane was perturbated due to the presence of undissolved particles.

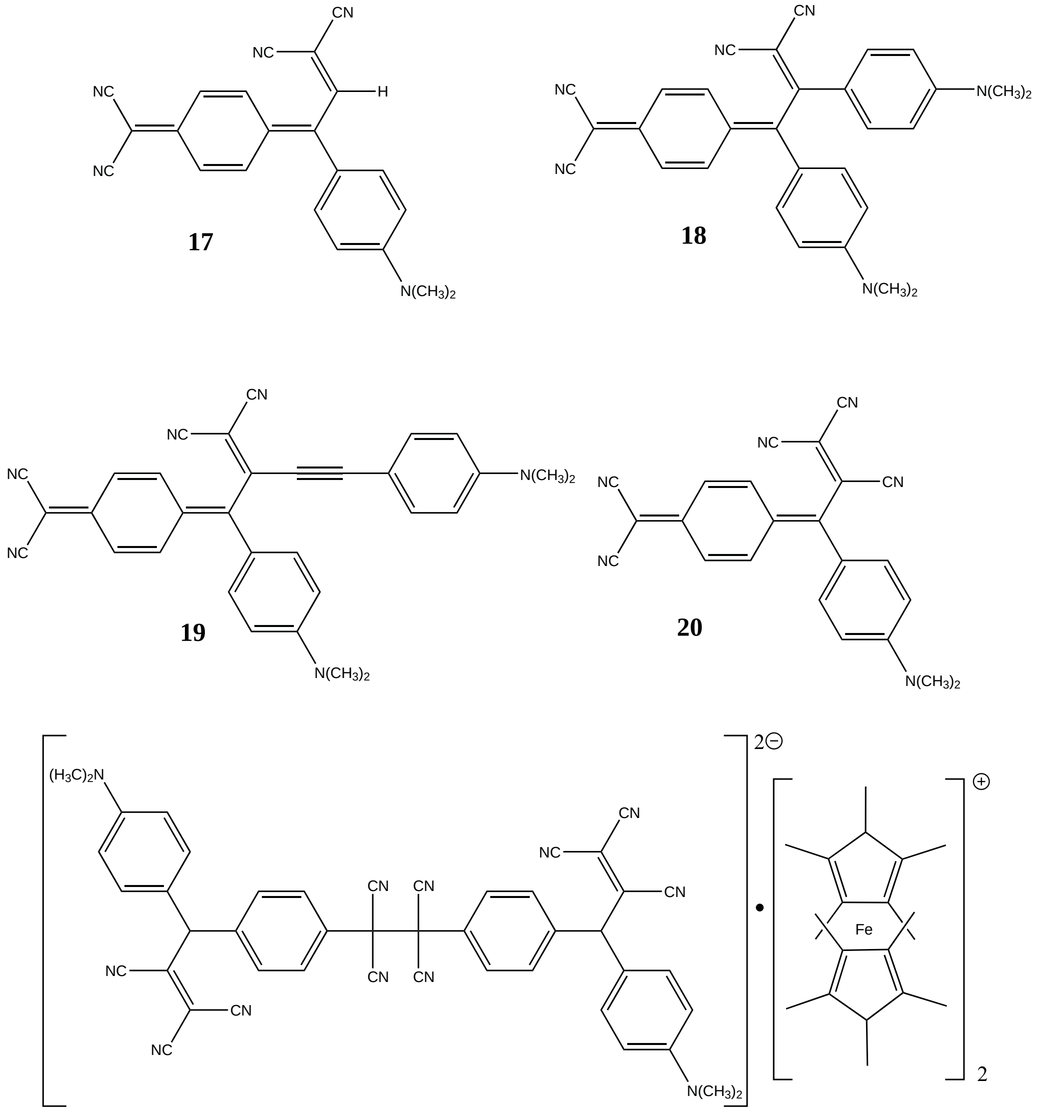

17

18

19

20

21

Figure 8.23: Molecular structures of **17**, **18**, **19**, **20** and **21**.

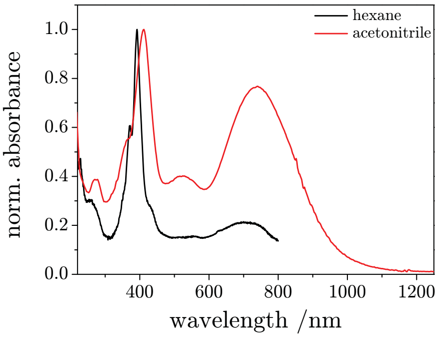

Figure 8.24: Absorption spectra of **17** in hexane and acetonitrile, respectively.

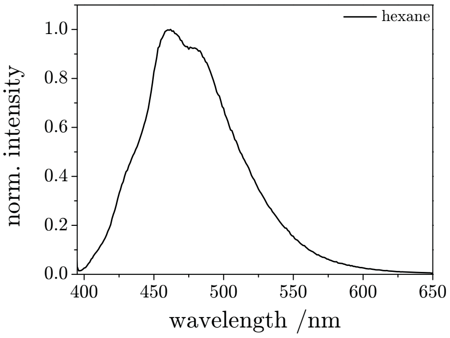

Figure 8.25: Emission spectrum of **17** in hexane ($\lambda_{\mathrm{exc}} = 392\,\mathrm{nm}$).

It was revealed by means of cyclic voltammetry that conjugation between donor and acceptor moieties is more pronounced in compound **17** compared to **18** or **19**, respectively [181]. Compound **17** can adapt a more planar structure compared to **18** or **19**, respectively, due to substitution with the small H atom. [182]

Compound **18** is a derivative of compound **17** where the H atom is replaced by a dimethylaminophenyl group. Compound **18** gave an absorption spectrum in acetonitrile with peaks at 424 nm ($\epsilon = 38{,}000\,{}^{1}\!/\mathrm{mol\ cm}$) and at 674 nm ($\epsilon = 42{,}000\,{}^{1}\!/\mathrm{mol\ cm}$), respectively (*cf.* figure 8.26).

Compound **19** is structurally related to compound **18** as the only difference is an ethyn-1,2-diyl spacer. Compound **19** gave an absorption spectrum in acetonitrile with a structured peak at 449 nm and at 486 nm ($\epsilon = 32{,}000\,{}^{1}\!/\mathrm{mol\ cm}$), respectively, and a broad peak at 687 nm ($\epsilon = 37{,}000\,{}^{1}\!/\mathrm{mol\ cm}$) with an end-absorption reaching in the near infrared region (*cf.* figure 8.27). The introduction of a second donor moiety in **18** and **19** compared to **17** is expressed in the absorption spectra in terms of an increasing intensity of the CT bands as already observed in [180] with similar molecules.

Compound **20** is again related to the previous compounds, but with a CN group instead of the H atom in compound **17**.
The absorption spectrum of compound **20** in acetonitrile features peaks at 489 nm ($\epsilon = 12{,}600\,{}^{1}\!/\mathrm{mol\ cm}$) and at 827 nm ($\epsilon = 7{,}300\,{}^{1}\!/\mathrm{mol\ cm}$) with again a long end-absorption in the near infrared region near 1,400 nm (*cf.* figure 8.28). Note that such a small HOMO–LUMO gap is very remarkable for such a small molecule [183, 184]. The absorption spectrum is comparable to

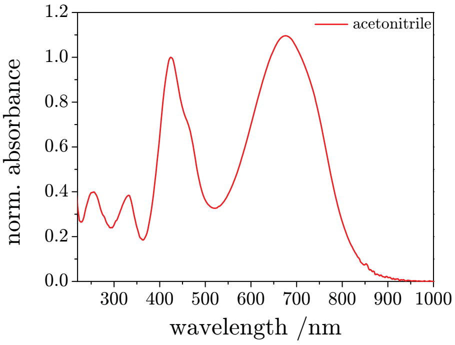

Figure 8.26: Absorption spectrum of **18** in acetonitrile.

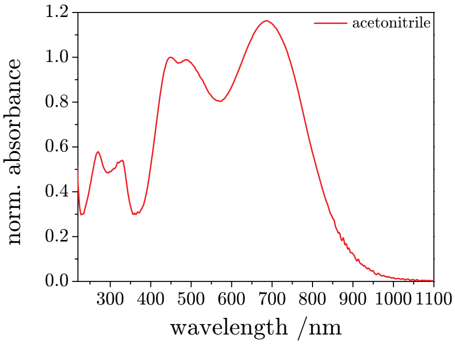

Figure 8.27: Absorption spectrum of **19** in acetonitrile.

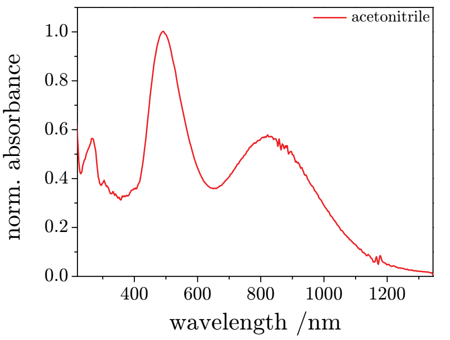

Figure 8.28: Absorption spectrum of **20** in acetonitrile.

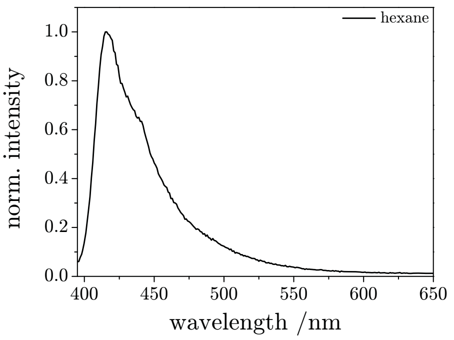

Figure 8.29: Emission spectrum of **20** in hexane ($\lambda_{\text{exc}} = 391\,\text{nm}$).

the spectrum of compound **17** where the CT band intensity is also rather weak due to the presence of only one donor group. However, the CT band is shifted to even lower energies in compound **20** due to the presence of one additional CN group.

Only a very small peak at 391 nm could be made out in the absorption spectrum in hexane, due to bad solubility. This wavelength was used as excitation wavelength and a fluorescence spectrum with a maximum at 416 nm could be recorded in hexane (*cf.* figure 8.29). An excitation spectrum recorded at the wavelength of maximum emission tentatively describes the absorption spectrum.

Compound **20** was also analyzed by means of EPR. The corresponding spectra and g factors are summarized together with **20**'s fluorinated counterparts in section 8.4.2.

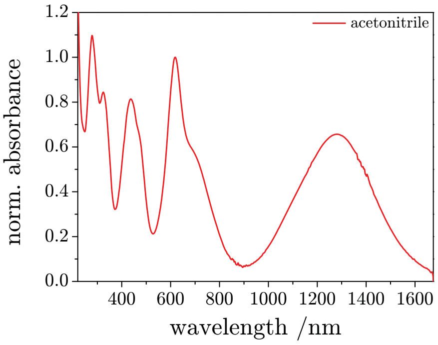

Figure 8.30: Absorption spectrum of **21** in acetonitrile.

Compound **21** is formed spontaneously out of **20** in the presence of decamethylferrocene *via* reductive σ dimerization. Interestingly, solid samples of **21** were found to be EPR silent, whereas in solution a signal attributable to the radical anion of **20** could be observed [7, 185].

The absorption spectrum of compound **21** in acetonitrile shows intense CT peaks at 618 nm ($\epsilon = 43{,}500\,{}^{1}\!/\mathrm{mol\ cm}$) and even at 1,279 nm ($\epsilon = 29{,}600\,{}^{1}\!/\mathrm{mol\ cm}$), respectively (*cf.* figure 8.30). Due to bad solubility in hexane only a very weak absorption spectrum could be recorded. No fluorescence was observable, neither in hexane nor in acetonitrile.

Specific Characteristics of 17 and 20

It is striking that compounds **17** and **20** were the only two TCNQ adducts under investigation to emit fluorescence. The reason for this is most likely to be found in their structural resemblance (H substituted by CN group) as well as the presence of only one instead of two donor moieties (as in non-fluorescent **18** or **19**, respectively).

It could be revealed in cyclic voltammetry experiments that both one-electron reduction steps of compound **20** are anodically shifted by 230 mV due to the presence of the additional CN group compared to **17** [181]. Due to the proximity of the CN groups in **17** and **20**, the difference between their two one-electron reduction potentials (260 mV) is larger compared to compounds where a spacer isolates the CN groups. Furthermore, the additional CN group in compound **20** anodically shifts the oxidation potential by 100 mV to 0.52 V compared to **17** (0.42 V, *cf.* table 8.1) [185]. The dimethyl-

Table 8.1: Cyclic voltammetry data for **17** [182] and **20** [181] in CH_2Cl_2 + 0.1 M Bu_4NPF_6 *vs.* Fc^+/Fc, scan rate 100 mV/s.
E° stands for the average of cathodic and anodic peak potentials and E_p denotes the irreversible peak potential.

17		**20**	
E° /V	E_p /V	E° /V	E_p /V
	+0.42		+0.52
-0.50		-0.27	
-0.76		-0.53	

anilino donor is thus readily oxidized and as a result, less electron density is transferred to the acceptor moieties. Ground-state CT interactions are thus expected to be less efficient in this type of molecules [181].

Weak ground-state CT interactions can also be made out in the absorption spectrum, as the relative intensity of the CT band is lower compared to compounds **18** or **19**, respectively. Additional donor groups are known to favor CT interactions and promote strong structural self-quenching effects [186]. The additional donor groups in **18** or **19** are thus expected to enhance the ionic character of the CT state and accelerate non-radiative decay [187].

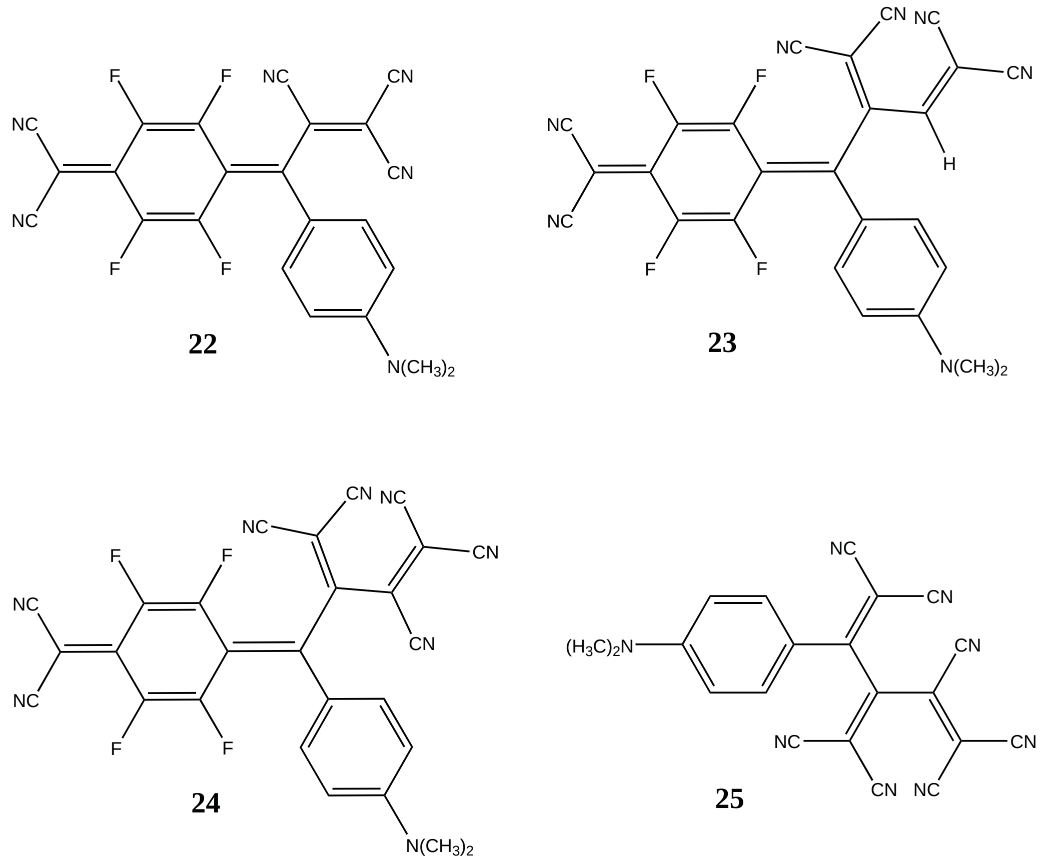

22 **23** **24** **25**

Figure 8.31: Molecular structures of **22**, **23**, **24** and **25**.

8.4 Donor-Substituted F_4-Tetracyanoquinodimethanes

Based on compounds introduced in the previous section, this section is devoted to even stronger organic acceptors, so-called “super-acceptors”. “Super-acceptors” are characterized by the incorporation of strong acceptor groups such as F_4-TCNQ or additional CN groups. However, high steric demand in these molecules enhances non-planarity and therefore, efficient π conjugation is hindered. The presence of electron-withdrawing fluorine groups anodically shifts and thus facilitates their first reduction step. Exceptionally small HOMO–LUMO gaps make these compounds again interesting for optoelectronic applications. [7, 185]
Compounds **22-25** are dark metallic-like solids. Their structures are shown in figure 8.31.

Table 8.2: Absorption maxima of **20**, **22**, **23** and **24** in acetonitrile.

	20	**22**	**23**	**24**
1^{st} CT band /nm	489	529	682	754
2^{nd} CT band /nm	827	960	886	1,050

8.4.1 Optical Properties

Compound **22** has essentially the same structure as compound **20** but with fluorine atom substitution. The first electron reduction of **22** is reported to be facilitated compared to **20** due to the presence of the electron withdrawing F atoms by 270 mV [7]. The absorption spectrum of compound **22** in acetonitrile shows peaks at 529 nm (ϵ = 27,500 $^{1}/_{\text{mol cm}}$) and at 960 nm (ϵ = 21,500 $^{1}/_{\text{mol cm}}$) with an end-absorption reaching in the near infrared region close to 1,600 nm (*cf.* figure 8.32). The compound is not very well soluble in hexane and does not fluoresce in neither hexane nor acetonitrile.

Compound **23** has one additional CN group compared to **22**. Its absorption spectrum features two CT bands at 682 nm (ϵ = 29,000 $^{1}/_{\text{mol cm}}$) and at 886 nm (ϵ = 21,700 $^{1}/_{\text{mol cm}}$) with an end-absorption at about 1,500 nm (*cf.* figure 8.33). The sample is again hardly soluble in hexane and does not show fluorescence in neither hexane nor acetonitrile.

Compound **24** has one more additional CN group compared to **23**. Its absorption spectrum peaks at 754 nm (ϵ = 26,000 $^{1}/_{\text{mol cm}}$) and at 1,050 nm (ϵ = 8,300 $^{1}/_{\text{mol cm}}$) with an end-absorption beyond 1,600 nm (*cf.* figure 8.34).

The introduction of additional CN groups (from compound **22** to **23** and **24**) thus leads to a bathochromic shift of the CT absorption bands. A comparison of fluorinated and unfluorinated compounds (compound **22** and compound **20**, respectively) shows that the substitution with F atoms further lowers the energy of the CT absorption band as summarized in table 8.2.
Hand in hand with these findings is the observation of an anodical shift of the first electron reduction potential when going from **22** to **24**. However, a cathodic shift was observed when going from **22** to **23**. Thus it is likely that structural congestions hamper efficient π conjugation between donor and acceptor in these molecules and thus complicate straightforward analysis of the correlation of redox properties and acceptor strength. [7]

Compound **25** is a TCNE adduct and can, due to its strong electron ac-

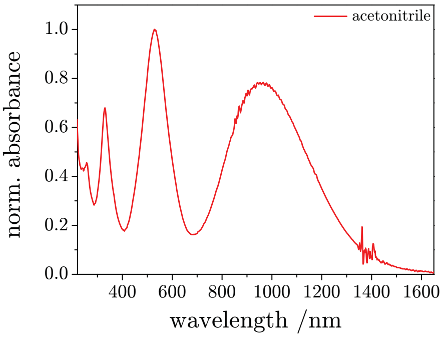

Figure 8.32: Absorption spectrum of **22** in acetonitrile.

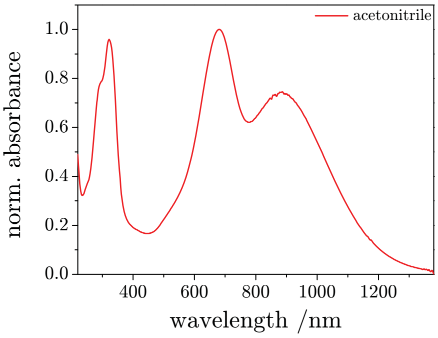

Figure 8.33: Absorption spectrum of **23** in acetonitrile.

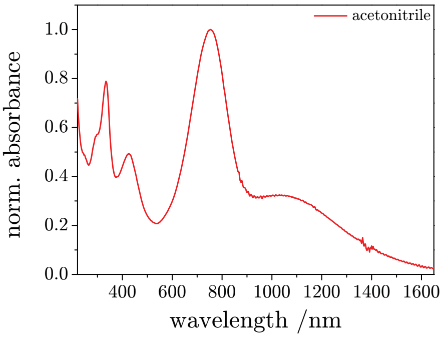

Figure 8.34: Absorption spectrum of **24** in acetonitrile.

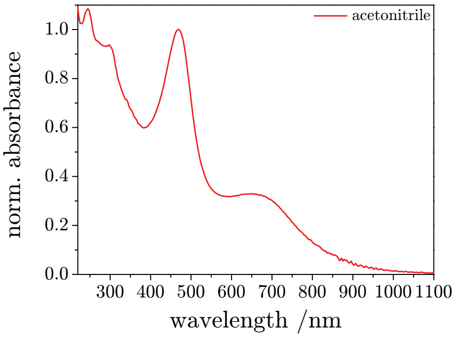

Figure 8.35: Absorption spectrum of **25** in acetonitrile.

cepting properties, as well be classified a "super-acceptor". Its absorption spectrum in acetonitrile shows peaks at 469 nm ($\epsilon = 16{,}500\,{}^{1}\!/_{\mathrm{mol\,cm}}$) and at 656 nm ($\epsilon = 5{,}500\,{}^{1}\!/_{\mathrm{mol\,cm}}$) with an end-absorption at 1,100 nm (*cf.* figure 8.35).

The relatively high oxidation potential of compound **25** indicates efficient ground-state interaction between donor and acceptor moieties ($E_\mathrm{p} = 0.91\,\mathrm{V}$ in CH_2Cl_2 + 0.1 M Bu_4NPF_6 *vs.* Fc^+/Fc). Comparative studies on compounds featuring less CN groups show that the optical HOMO–LUMO gaps correlate well with the electrochemical gaps and ascribe the small electrochemical gap of **25** to the increased acceptor strength due to the presence of the CN groups. [185]

8.4.2 Magnetic Properties

Compounds **20**, **22**, **23** and **24** were furthermore analyzed by means of EPR in order to investigate how geometric constraints in these molecules influence electron delocalization. As no NMR spectrum could be obtained for these species, EPR spectroscopy was applied in order to identify the paramagnetic character of this species.

EPR spectra were recorded on our Bruker ESP300E X-band spectrometer by DI B. Enko (TU Graz). Interestingly, all compounds revealed EPR spectra of remarkable intensity, though unresolved, already in the solid state without applying any redox reactions. Due to anisotropic interactions, however, the lines observed in the solid state are rather broad. [185]

Compounds **20** and **22** were dissolved in dry DME and spectra of remarkable intensity could be recorded of the unreduced species. Reduction on a K metal mirror yielded compatible spectra at 270 K and 180 K, respectively. In both, liquid (270 K) and frozen (180 K) solution, intense but unresolved EPR spectra were observable which could tentatively be ascribed to the respective radical anions (*cf.* figures 8.36 and 8.37 for **20** and figures 8.38 and 8.39 for **22**, respectively).

Compounds **23** and **24** were analyzed in the solid state as well as dissolved in acetone-d_6 which was deaerated by bubbling with argon (*cf.* figures 8.40 and 8.41 for **23** and figures 8.42 and 8.43 for **24**, respectively). These two compounds were furthermore analyzed by means of NMR. The fact that no NMR spectrum is observable, is again in line with the paramagnetism revealed by EPR experiments.

Table 8.3 summarizes the g factors for compounds **22**-**24** as well as for the unfluorinated reference **20**. The virtually matching g factors indicate compatible electronic structures. Furthermore, the obtained g factors are in good agreement with the values published for $TCNE^{\bullet\ominus}$ (2.0026 ± 0.0002 [188]), $TNCQ^{\bullet\ominus}$ (2.0027 ± 0.0001 [189]) and F_4-$TCNQ^{\bullet\ominus}$ (2.0029 ± 0.0001 [189]).

Table 8.3: g factors of **20**, **22**, **23** and **24** at different conditions.

	g factor
20 in DME at 180 K	2.0034
$\mathbf{20}^{\bullet\ominus}$ in DME at 180 K	2.0036
22 in DME at 270 K	2.0033
$\mathbf{22}^{\bullet\ominus}$ in DME at 270 K	2.0037
solid **23**	2.0037
1 mM **23** in acetone-d_6 deaerated with Ar	2.0032
solid **24**	2.0033
1 mM **24** in acetone-d_6 deaerated with Ar	2.0032

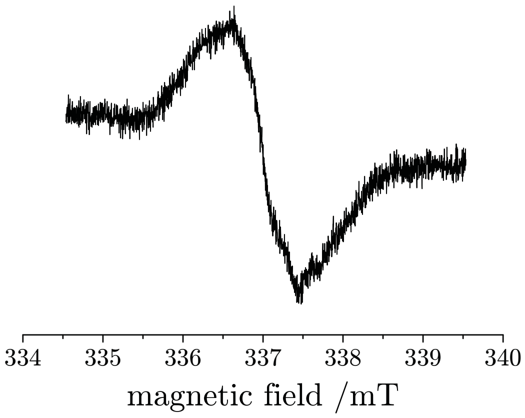

Figure 8.36: EPR spectrum of **20** in DME at 180 K.

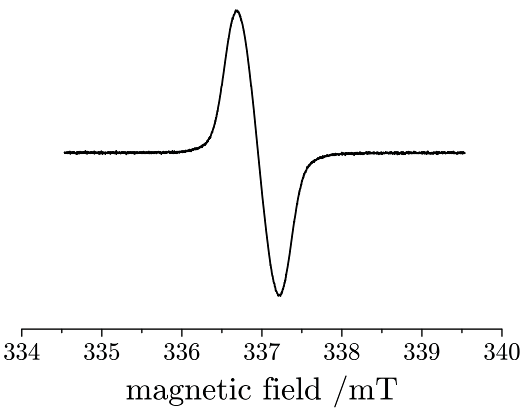

Figure 8.37: EPR spectrum of $\mathbf{20}^{\bullet\ominus}$ in DME at 180 K.

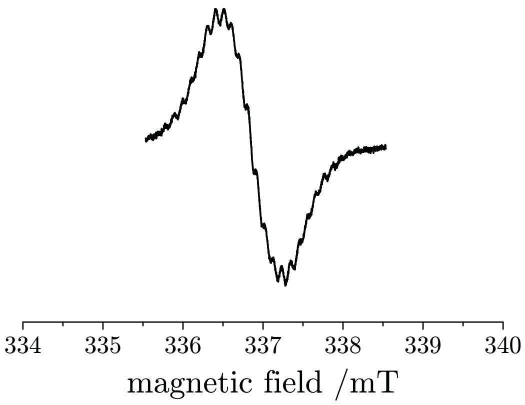

Figure 8.38: EPR spectrum of **22** in DME at 270 K.

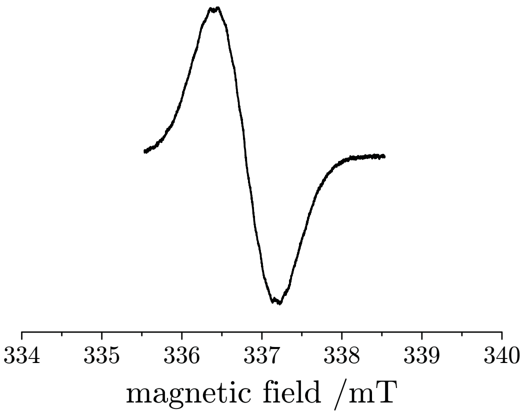

Figure 8.39: EPR spectrum of $\mathbf{22}^{\bullet\ominus}$ in DME at 270 K.

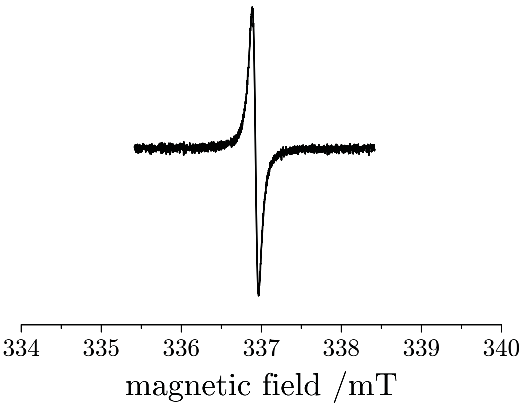

Figure 8.40: EPR spectrum of solid **23**.

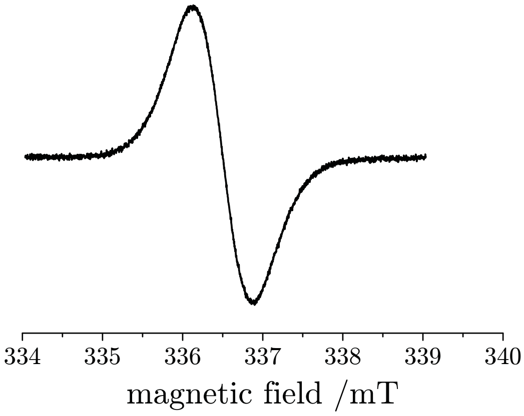

Figure 8.41: EPR spectrum of 1 mM **23** in acetone-d_6 deaerated with Ar.

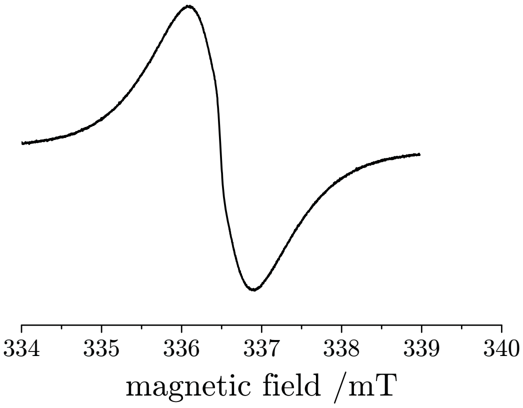

Figure 8.42: EPR spectrum of solid **24**.

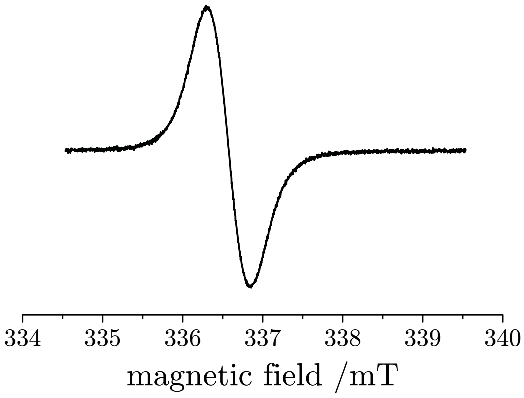

Figure 8.43: EPR spectrum of 1 mM **24** in acetone-d_6 deaerated with Ar.

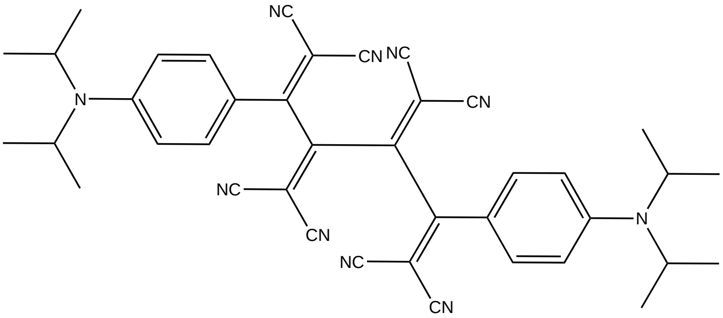

Figure 8.44: Molecular structure of **26**.

8.5 Donor-Substituted Octacyano[4]dendralenes

The molecule under investigation in this section is a donor-substituted octacyano[4]dendralene, namely 3,4-bis(dicyanomethylene)-2,5-bis[4-(diisopropylamino)phenyl]hexa-1,5-diene-1,1,6,6-tetracarbonitrile (**26**, *cf.* figure 8.44). Synthesis of this type of molecules has been reported by Diederich and coworkers by means of a double addition of tetracyanoethylene (TCNE) to buta-1,3-diynes which got activated by two terminal anilino donor groups. [190]

Molecules of this class show intense charge-transfer absorption bands of low energy. Due to their eight cyano groups and despite substitution by strong donors, they act as strong electron acceptors with very low reversible one-electron reduction potentials (-0.09 to -0.17 eV in CH_2Cl_2 + 0.1 M Bu_4NPF_6 *vs.* Fc^+/Fc). As far as the computed adiabatic electron affinity is concerned, this class of molecules is comparable to the reference acceptor 2,3,5,6-tetrafluoro-7,7,8,8-tetracyanoquinodimethane (F_4-TCNQ) which is used as p-type dopant in organic light-emitting diodes and solar cells.

A detailed study on **26**'s structural and physical properties has been submitted to a peer-reviewed journal at the time of the submission of this thesis. Our studies on the magnetic properties shall be elaborated in this section in more detail. [190]

8.5.1 Experimental

CD_3CN (Sigma-Aldrich) was used as received. ^1H NMR experiments were performed on a Bruker AVANCE 200 MHz DPX NMR spectrometer equipped with a 5 mm BBO (BB-1H) probehead and a temperature controller (BVT 3200) by DI M. Griesser (TU Graz). Magnetic susceptibility measurements were performed by Prof. Dr. K. Gatterer (TU Graz) on a SUS-10 from Anton Paar KG, Austria. EPR spectra were taken on a Bruker ESP300E spectrometer (variable temperature unit) as well as on our benchtop EPR spectrometer MiniScope MS 100 from Magnettech.

8.5.2 Magnetic Properties

The ^{1}H NMR spectra of **26** in CD_3CN (200 MHz) reveal strong line broadening at 293 K. Upon raising the temperature in 10 K-steps to 343 K, the lines become substantially narrower (*cf.* figure 8.47). The fact that all lines in the NMR spectrum are broadened to the same extent indicates that this observation cannot be attributed to dynamic effects, *e.g.* a hindered rotation about a single bond. It is more likely that this observation is based on the presence of paramagnetic, charge-separated stages of **26**. Therefore, the exact same sample used for the NMR measurements was placed into an EPR spectrometer.

In EPR, a well distinguishable, but unresolved spectrum could be recorded. The results obtained from EPR measurements perfectly reflect the results obtained by NMR, as the intensity of the EPR spectrum decreases upon increasing the temperature (*cf.* figure 8.46). This observation can be explained by a higher amount of paramagnetic stage being present at lower temperatures. As solvent polarity decreases upon increasing the temperature, the observations made in the EPR experiments point to a charged or charge-separated species, which is stabilized under more polar conditions [28]. Although the EPR spectrum is unresolved, its width of about 2 mT and its g factor of 2.0030 are characteristic for delocalized organic radical anions in which the spin population resides mainly on cyano group containing moieties [28]. Furthermore, radical anions similar to $\mathbf{26}^{\bullet\ominus}$ often lead to unresolved EPR spectra [185]. Taking into account the LUMO of **26** which describes the electron distribution in **26** upon one-electron reduction, the recorded spectrum can tentatively be assigned to $\mathbf{26}^{\bullet\ominus}$.
It is interesting to note that also a solid sample of **26** gives rise to an EPR spectrum (*cf.* figure 8.45) compatible with $\mathbf{26}^{\bullet\ominus}$.

In order to estimate the amount of the content of the paramagnetic species, the magnetic susceptibility of solid **26** was determined. At room temperature, the value of χ_m = -2.16*10^{-9} $^{\mathrm{m}^3}/_{\mathrm{kg}}$ indicates that the sample

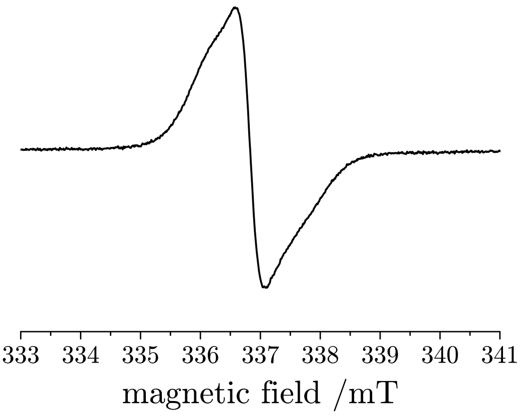

Figure 8.45: EPR spectrum of **26**$^{\bullet\ominus}$ in the solid state at 293 K.

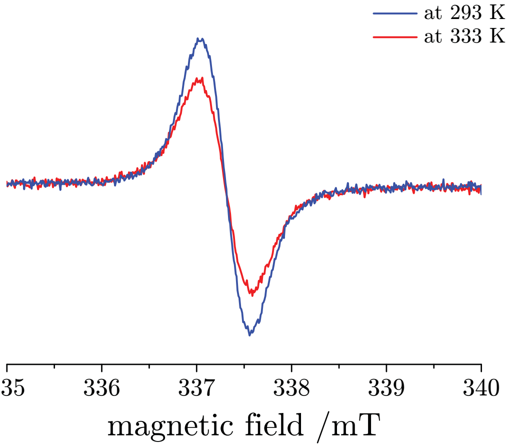

Figure 8.46: EPR spectra of **26**$^{\bullet\ominus}$ in CD_3CN at 293 K and 333 K.

is basically diamagnetic. However, this value depends on the strength of the magnetic field – a fact which suggests some paramagnetic content. This observation is again in line with the observations made by NMR and EPR.

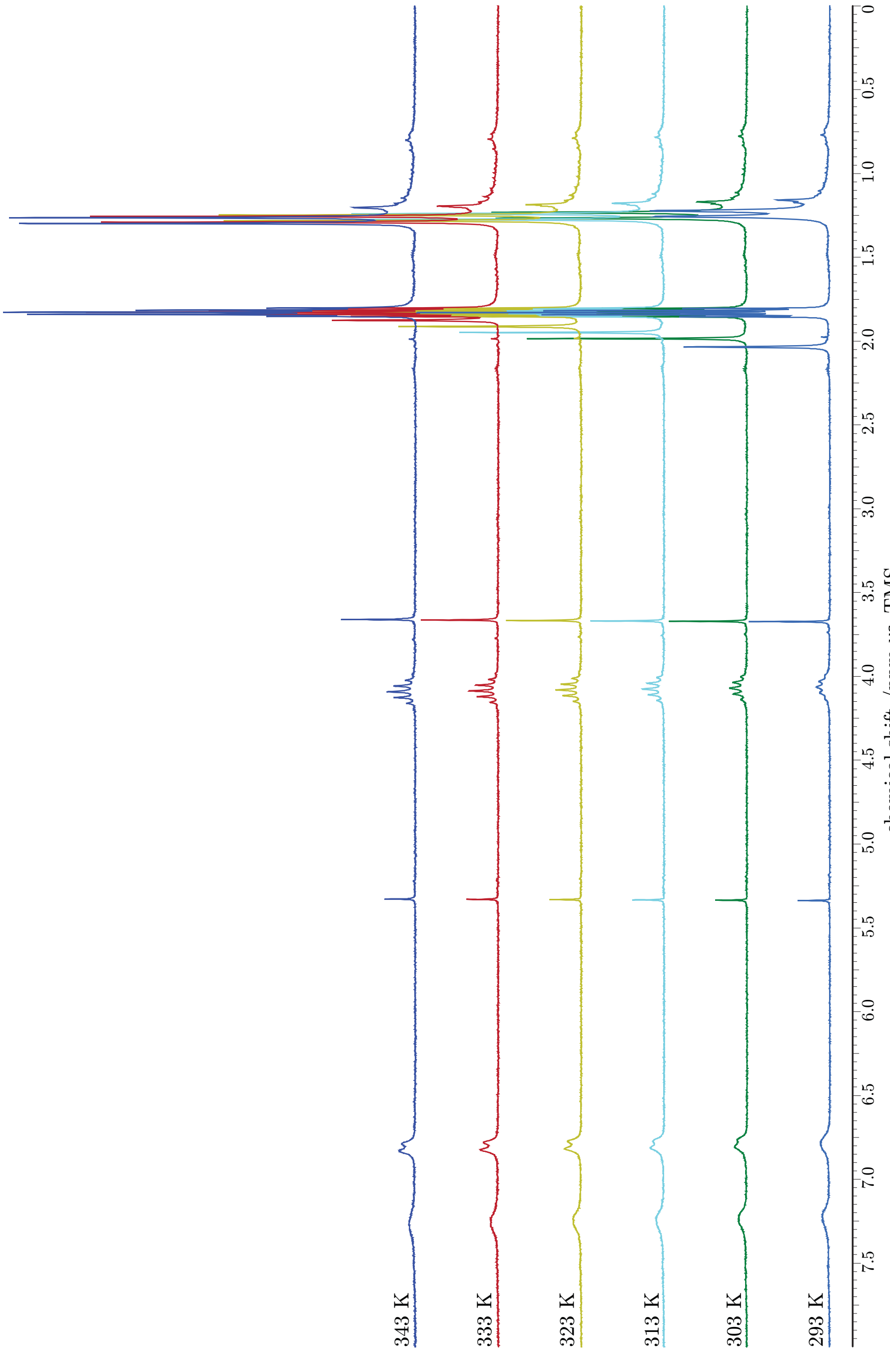

Figure 8.47: Variable temperature ^{1}H NMR spectra of **26** in CD_3CN (200 MHz).

Appendix A

Glossary of Compounds

The following table attributes the compounds' numbering used in this thesis to the acronyms used by Prof. Diederich's group.

Table A.1: Attribution of the compounds' numbering to the acronyms used by Prof. Diederich's group.

compound **1**	CN1	compound **14**	CN11
compound **2**	CN2	compound **15**	CN12
compound **3**	CN3	compound **16**	CN13
compound **4**	CN4	compound **17**	MK589/08
compound **5**	MK607/08	compound **18**	MK587/08
compound **6**	CN5	compound **19**	MK588/08
compound **7**	CN6	compound **20**	MK568/08
compound **8**	CN7	compound **21**	MK583/08
compound **9**	MK634/08	compound **22**	MK542/07
compound **10**	CN10	compound **23**	MK621/08
compound **11**	CN8	compound **24**	MK636/08
compound **12**	MK637/08	compound **25**	MK635/08
compound **13**	CN9	compound **26**	BB/58/1

List of Figures

List of Tables

List of Abbreviations

α	solute polarizability
χ_m	magnetic susceptibility
ϵ	molar decadic extinction coefficient
η	dynamic viscosity
γ_e	gyromagnetic ratio of the electron
μ_0	permeability of vacuum
μ_B	Bohr magneton
μ_N	nuclear magneton
μ_x	dipole moment
ν	kinematic viscosity
ν_i	frequency
ϕ_i	quantum yield
ρ	mass density
τ	excited-state lifetime
θ	temperature
$\tilde{\nu}$	wavenumber
ε_0	vacuum permittivity
ε_S	dielectric constant of the solvent
φ_X^Ψ	spin population in orbital Ψ centered on nucleus X

φ_S	electron spin density
$\vec{\mu}_e$	magnetic moment of the electron
$\vec{\mu}_n$	nuclear magnetic moment
$\vec{B}$	magnetic field
$\vec{I}$	nuclear spin
$\vec{S}$	electron spin
A	hyperfine coupling constant
a	hyperfine splitting constant
A'	empirical parameter describing π,σ-spin polarization
A_i	absorbance
B	magnetic field strength
B'	empirical parameter describing hyperconjugation
c	concentration
c	velocity of light
D	dispersion interaction between solute and solvent
D and E	zero-field splitting parameter D and E
D_{XX}, D_{YY}, D_{ZZ}	principal values of the zero-field splitting tensor
E	energy
E°	average of cathodic and anodic peak potentials
e_0	elementary charge
E_p	irreversible peak potential
E_dip	dipole interaction term
E_Fc	Fermi contact term
E_{00}	excitation energy
$G(\lambda)$	sensitivity ratio of the detection system

g_e	g factor of the free electron
g_n	g factor of the nucleus
h	Planck's constant
I	ionic strength
I	nuclear spin quantum number
$I(\lambda)$	fluorescence emission intensity
k	Boltzmann constant
K_A	association constant
k_d	diffusional rate constant
k_q	bimolecular quenching rate constant
K_{SV}	Stern-Volmer constant
k_{ET}	electron transfer rate constant
m_e	mass of the electron
m_I	nuclear magnetic spin quantum number
m_p	mass of the proton
m_S	magnetic spin quantum number
N_A	Avogadro constant
n_i	refractive index
$n_{\alpha,\beta}$	population in the α, β state
Q	McConnell's proportionality constant
R	universal gas constant
r	Onsager cavity radius
R_c	contact radius
S	spin quantum number
T	absolute temperature

$T(\lambda)$	transmittance
T_e	spin-lattice relaxation time
W_e	electron spin-lattice relaxation
W_r	coulombic work term
W_n	nuclear spin-lattice relaxation
W_x	cross-relaxation process
z	charge
(O)LED	(organic) light-emitting diode
3cmlf	3-(carboxymethyl)-lumiflavin
BPB	1,4-bis(phenylethynyl)benzene
DPA	diphenylacetylene
TMPPD	*N,N,N',N'*-tetramethyl-*p*-phenylenediamine
"Magic Blue"	tris-(*p*-bromophenyl)ammoniumyl hexachloroantimonate
CIDNP	Chemically Induced Dynamic Nuclear Polarization
CT	charge-transfer
Cys	DL-cysteine
DDQ	2,3-dichloro-4,5-dicyanobenzoquinone
DEE	diethylether
DFT	density functional theory
DME	dimethoxyethane
DPPH$^\bullet$	2,2-diphenyl-1-picrylhydrazyl radical
ENDOR	Electron Nuclear DOuble Resonance
EPR	Electron Paramagnetic Resonance
ESR	Electron Spin Resonance
F_4-TCNQ	2,3,5,6-tetrafluoro-7,7,8,8-tetracyanoquinodimethane

Fc^+/Fc	ferrocenium/ferrocene
HFP	1,1,1,3,3,3-hexafluoro-2-propanole
hfsc	hyperfine splitting constant(s)
His	DL-histidine
HMPT	*N,N,N',N',N",N"*-hexamethylphosphoric triamide
HOMO	highest occupied molecular orbital
ICA	independent component analysis
IND	factor indicator function
LUMO	lowest unoccupied molecular orbital
Met	DL-methionine
MTHF	2-methyltetrahydrofuran
NMR	nuclear magnetic resonance
OD	optical density
PCA	principal component analysis
PIFA	phenyliodine(III) bistrifluoroacetate
RE	real error
SA	solvent acidity
SB	solvent basicity
SCE	saturated calomel electrode
SdP	solvent polarity
SP	solvent polarizability
TCBD	1,1,4,4-tetracyanobuta-1,3-diene
TCNE	tetracyanoethylene
TCNQ	7,7,8,8-tetracyanoquinodimethane
$TEMPO^\bullet$	2,2,6,6-tetramethyl-4-oxopiperidinyl-1-oxyl radical

TFA	trifluoroacetic acid
THF	tetrahydrofuran
Trp	DL-tryptophan
TTF	tetrathiafulvalene
ZFS	zero-field splitting

Bibliography

[1] V. Balzani, *Pure and Applied Chemistry* **2008**, *80*, 1631–1650.

[2] S. Horiuchi, T. Hasegawa, Y. Tokura, *Journal of the Physics Society Japan* **2006**, *75*, 051016/01–051016/14.

[3] J. Jortner, M. Bixon, M. A. Ratner, *Proceedings of the Indian Academy of Sciences (Chemical Sciences)* **1997**, *109*, 365–377.

[4] V. Balzani, A. Credi, M. Venturi, *Molecular Devices and Machines: Concepts and Perspectives for the Nanoworld 2nd ed.*, Wiley-VCH, **2008**.

[5] A. C. Benniston, A. Harriman, D. B. Rewinska, S. Yang, Y.-G. Zhi, *Chemistry - A European Journal* **2007**, *13*, 10194–10203.

[6] A. Rosspeintner, G. Angulo, C. Onitsch, M. Kivala, F. Diederich, G. Grampp, G. Gescheidt, *ChemPhysChem* **2010**, *11*, 1700–1710.

[7] S.-i. Kato, F. Diederich, *Chemical Communications* **2010**, *46*, 1994–2006.

[8] C. Li, M. Liu, N. G. Pschirer, M. Baumgarten, K. Müllen, *Chemical Reviews* **2010**, *ASAP*.

[9] R. R. Tykwinski, U. Gubler, R. E. Martin, F. Diederich, C. Bosshard, P. Günter, *The Journal of Physical Chemistry B* **1998**, *102*, 4451–4465.

[10] T. Michinobu, J. C. May, J. H. Lim, C. Boudon, J.-P. Gisselbrecht, P. Seiler, M. Gross, I. Biaggio, F. Diederich, *Chemical Communications* **2005**, 737–739.

[11] B. I. Kochelaev, Y. V. Yablokov, *The Beginning of Paramagnetic Resonance*, World Scientific Publishing, **1995**.

[12] R. Cummerow, D. Halliday, *Physical Review* **1946**, *70*, 433–433.

[13] D. M. S. Bagguley, J. H. E. Griffiths, *Nature* **1947**, *160*, 532–533.

[14] C. J. Rhodes, *Annual Reports Section "C" (Physical Chemistry)* **2006**, *102*, 166–202.

[15] C. J. Rhodes, *Annual Reports Section "C" (Physical Chemistry)* **2004**, *100*, 149–193.

[16] T. Prisner, M. Rohrer, F. MacMillan, *Annual Review of Physical Chemistry* **2001**, *52*, 279–313.

[17] G. Feher, *Physical Review* **1956**, *103*, 500–501.

[18] R. Biehl, M. Plato, K. Möbius, *The Journal of Chemical Physics* **1975**, *63*, 3515–3522.

[19] J. A. Weil, J. R. Bolton, J. E. Wertz, *Electron Paramagnetic Resonance: Elementary Theory and Practical Applications*, Wiley-Interscience, **1994**.

[20] M. Brustolon, *What Can Be Studied with Electron Paramagnetic Resonance*, M. Brustolon, E. Giamello (Eds.), John Wiley & Sons, Inc., Hoboken, New Jersey, **2009**, chapter 3, pp. 83–108.

[21] A. Rosspeintner, M. Griesser, N. Pucher, K. Iskra, R. Liska, G. Gescheidt, *Macromolecules* **2009**, *42*, 8034–8038.

[22] F.-J. Methner, T. Kunz, *Genauere Prognosen zur oxidativen Bierstabilität mittels ESR-Spektroskopie*, **2006**.

[23] A. Staško, V. Brezová, M. Mazúr, M. Čertík, M. Kalinák, G. Gescheidt, *LWT - Food Science and Technology* **2008**, *41*, 2126–2135.

[24] M. Polovka, *Journal of Food and Nutrition Research* **2006**, *45*, 1–11.

[25] W. Lubitz, F. Lendzian, R. Bittl, *Accounts of Chemical Research* **2002**, *35*, 313–320.

[26] L. Kulik, W. Lubitz, *Photosynthesis Research* **2009**, *102*, 391–401.

[27] G. E. Uhlenbeck, S. Goudsmit, *Nature* **1926**, *117*, 264–265.

[28] F. Gerson, W. Huber, *Electron Spin Resonance Spectroscopy of Organic Radicals*, Wiley VCH, **2003**.

[29] C. Corvaja, *Introduction to Electron Paramagnetic Resonance*, M. Brustolon, E. Giamello (Eds.), John Wiley & Sons, Inc., Hoboken, New Jersey, **2009**, chapter 1, pp. 3–35.

[30] C. P. Poole, *Electron spin resonance: a comprehensive treatise on experimental techniques*, Courier Dover Publications, **1996**.

[31] C. P. Slichter, *Principles of Magnetic Resonance (Springer Series in Solid-State Sciences) (v. 1)*, Springer, **1989**.

[32] K. Scheffler, H. Stegmann, *Elektronenspinresonanz.: Grundlagen und Anwendung in der organischen Chemie. (Organische Chemie in Einzeldarstellungen) (German Edition)*, Springer, **1970**.

[33] G. Gescheidt, *Electron Paramagnetic Resonance Spectroscopy in the Liquid Phase*, M. Brustolon, E. Giamello (Eds.), John Wiley & Sons, Inc., Hoboken, New Jersey, **2009**, chapter 4, pp. 109–157.

[34] F. Gerson, *Hochauflösende ESR-Spektroskopie, dargestellt anhand aromatischer Radikal-Ionen*, Verlag Chemie, **1967**.

[35] H. M. McConnell, *The Journal of Chemical Physics* **1956**, *24*, 632–633.

[36] H. M. McConnell, H. H. Dearman, *The Journal of Chemical Physics* **1958**, *28*, 51–53.

[37] H. M. McConnell, D. B. Chesnut, *The Journal of Chemical Physics* **1958**, *28*, 107–117.

[38] J. S. Hyde, A. H. Maki, *The Journal of Chemical Physics* **1964**, *40*, 3117–3118.

[39] D. M. Murphy, R. D. Farley, *Chemical Society Reviews* **2006**, *35*, 249–268.

[40] H. Kurreck, B. Kirste, W. Lubitz, *Angewandte Chemie (International Edition)* **1984**, *23*, 173–194.

[41] H. Kurreck, B. Kirste, W. Lubitz, *Electron Nuclear Double Resonance Spectroscopy of Radicals in Solution: Application to Organic and Biological Chemistry (Methods in Stereochemical Analysis)*, Wiley-VCH, **1988**.

[42] R. W. Holmberg, R. Livingston, W. T. Smith, *The Journal of Chemical Physics* **1960**, *33*, 541–546.

[43] J. Krzystek, A. Sienkienwicz, L. Pardi, L. C. Brunel, *Journal of Magnetic Resonance* **1997**, *125*, 207–211.

[44] O. Chen, J. Zhuang, F. Guzzetta, J. Lynch, A. Angerhofer, Y. C. Cao, *Journal of the American Chemical Society* **2009**, *131*, 12542–12543.

[45] E. Rozantzev, M. Neiman, *Tetrahedron* **1964**, *20*, 131–137.

[46] M. J. Davies, *Electron Paramagnetic Resonance Detection Of Radicals In Biology And Medicine*, M. Brustolon, E. Giamello (Eds.), John Wiley & Sons, Inc., Hoboken, New Jersey, **2009**, chapter 11, pp. 427–450.

[47] B. J. McClelland, *Chemical Reviews* **1964**, *64*, 301–315.

[48] K. W. Bowers, F. D. Greene, *Journal of the American Chemical Society* **1963**, *85*, 2331–2332.

[49] K. W. Bowers, G. J. Nolfi, F. D. Greene, *Journal of the American Chemical Society* **1963**, *85*, 3707–3707.

[50] A. G. Davies, A. G. Neville, *Journal of the Chemical Society, Perkin Transactions 2* **1992**, 163–169.

[51] E. Beer, J. Daub, C. Palivan, G. Gescheidt, *Journal of the Chemical Society, Perkin Transactions 2* **2002**, 1605–1610.

[52] T. Takeshita, N. Hirota, *Journal of the American Chemical Society* **1971**, *93*, 6421–6429.

[53] M. Scholz, G. Gescheidt, U. Schöberl, J. Daub, *Journal of the Chemical Society, Perkin Transactions 2* **1995**, 209–213.

[54] A. G. Davies, G. Gescheidt, *Electron Spin Resonance - Specialist Periodical Reports* **1993**, *14*, 1–31.

[55] A. G. Davies, *Journal of Chemical Research (S)* **2001**, *2001*, 253–261.

[56] A. G. Davies, K.-M. Ng, *Australian Journal of Chemistry* **1995**, *48*, 167–173.

[57] M. N. Khan, C. Palivan, F. Barbosa, J. Amaudrut, G. Gescheidt, *Journal of the Chemical Society, Perkin Transactions 2* **2001**, 1522–1526.

[58] H. Bock, U. Lechner-Knoblauch, *Journal of Organometallic Chemistry* **1985**, *294*, 295–304.

[59] F. A. Bell, A. Ledwith, D. C. Sherrington, *Journal of the Chemical Society C: Organic* **1969**, 2719–2720.

[60] L. Eberson, M. P. Hartshorn, O. Persson, *Acta Chimica Scandinavica* **1995**, *49*, 640–644.

[61] L. Eberson, M. P. Hartshorn, O. Persson, *Journal of the Chemical Society, Chemical Communications* **1995**, 1131–1132.

[62] L. Eberson, M. P. Hartshorn, O. Persson, *Journal of the Chemical Society, Perkin Transactions 2* **1995**, 1735–1744.

[63] I. H. Elson, J. K. Kochi, *Journal of the American Chemical Society* **1973**, *95*, 5060–5062.

[64] W. Adam, C. van Barneveld, O. Emmert, H. M. Harrer, F. Kita, A. S. Kumar, W. Maas, W. M. Nau, S. H. K. Reddy, J. Wirz, *Pure and Applied Chemistry* **1997**, *69*, 735–742.

[65] W. Adam, H. M. Harrer, T. Heidenfelder, T. Kammel, F. Kita, W. M. Nau, C. Sahin, *Journal of the Chemical Society, Perkin Transactions 2* **1996**, 2085–2089.

[66] W. Adam, C. van Barneveld, J.-S. Gerke, F. G. Klärner, *Journal of the Chemical Society, Perkin Transactions 2* **1999**, 2723–2728.

[67] C. Thomson, *Quarterly Reviews, Chemical Society* **1968**, *22*, 45–74.

[68] B. Kirste, H. Van Willigen, H. Kurreck, K. Moebius, M. Plato, R. Biehl, *Journal of the American Chemical Society* **1978**, *100*, 7505–7513.

[69] J. Brickmann, G. Kothe, *The Journal of Chemical Physics* **1973**, *59*, 2807–2814.

[70] S. Nakazawa, K. Sato, T. Kinoshita, T. Takui, K. Itoh, T. Nakamura, T. Momose, T. Shida, T. Okuno, A. Izuoka, T. Sugawara, *Synthetic Metals* **1997**, *85*, 1735–1736.

[71] M. Matsushita, T. Nakamura, T. Momose, T. Shida, Y. Teki, T. Takui, T. Kinoshita, K. Itoh, *Journal of the American Chemical Society* **1992**, *114*, 7470–7475.

[72] K. Itoh, *Pure and Applied Chemistry* **1978**, *50*, 1251–1259.

[73] T. Takui, K. Itoh, *Chemical Physics Letters* **1973**, *19*, 120–124.

[74] Y. Teki, T. Takui, T. Kinoshita, S. Ichikawa, H. Yagi, K. Itoh, *Chemical Physics Letters* **1987**, *141*, 201–205.

[75] Y. Teki, T. Takui, K. Itoh, H. Iwamura, K. Kobayashi, *Journal of the American Chemical Society* **1983**, *105*, 3722–3723.

[76] H. Iwamura, *Pure and Applied Chemistry* **1986**, *58*, 187–196.

[77] M. Matsushita, T. Momose, T. Shida, Y. Teki, T. Takui, K. Itoh, *Journal of the American Chemical Society* **1990**, *112*, 4700–4702.

[78] R. J. Van Zee, C. M. Brown, K. J. Zeringue, W. Weltner, *Accounts of Chemical Research* **1980**, *13*, 237–242.

[79] R. Huang, H. J. Kim, D. B. Min, *Journal of Agricultural and Food Chemistry* **2006**, *54*, 2359–2364.

[80] M. Y. Jung, D. B. Min, *Journal of Food Science* **2009**, *74*, C449–C455.

[81] G. R. Penzer, G. K. Radda, *Quarterly Reviews, Chemical Society* **1967**, *21*, 43–65.

[82] G. R. Penzer, G. K. Radda, *The Biochemical Journal* **1968**, *109*, 259–268.

[83] A. Kozik, W. Korytowski, T. Sarna, A. S. Bloom, *Biophysical Chemistry* **1990**, *38*, 39–48.

[84] P. Drössler, W. Holzer, A. Penzkofer, P. Hegemann, *Chemical Physics* **2003**, *286*, 409–420.

[85] S. D. M. Islam, A. Penzkofer, P. Hegemann, *Chemical Physics* **2003**, *291*, 97–114.

[86] E. Sikorska, I. Khmelinskii, A. Komasa, J. Koput, L. F. V. Ferreira, J. R. Herance, J. L. Bourdelande, S. L. Williams, D. R. Worrall, M. Insinska-Rak, *Chemical Physics* **2005**, *314*, 239–247.

[87] C. Onitsch, Diploma thesis, Graz University of Technology, Graz, **2007**.

[88] P. Hore, E. Zuiderweg, R. Kaptein, K. Dijkstra, *Chemical Physics Letters* **1981**, *83*, 376–383.

[89] R. Kaptein, K. Dijkstra, F. Müller, C. G. van Schagen, A. J. W. G. Visser, *Journal of Magnetic Resonance (1969)* **1978**, *31*, 171–176.

[90] R. Kaptein, K. Nicolay, K. Dijkstra, *Journal of the Chemical Society, Chemical Communications* **1979**, 1092.

[91] S. Landgraf, *Spectrochimica Acta Part A: Molecular and Biomolecular Spectroscopy* **2001**, *57*, 2029–2048.

[92] E. Sikorska, I. V. Khmelinskii, W. Prukala, S. L. Williams, M. Patel, D. R. Worrall, J. L. Bourdelande, J. Koput, M. Sikorski, *The Journal of Physical Chemistry A* **2004**, *108*, 1501–1508.

[93] E. Sikorska, J. Herance, J. Bourdelande, I. Khmelinskii, S. Williams, D. Worrall, G. Nowacka, A. Komasa, M. Sikorski, *Journal of Photochemistry and Photobiology A: Chemistry* **2005**, *170*, 267–272.

[94] M. Insinska-Rak, E. Sikorska, J. R. Herance, J. L. Bourdelande, I. V. Khmelinskii, M. Kubicki, W. Prukala, I. F. Machado, A. Komasa, L. F. V. Ferreira, M. Sikorski, *Photochemical & Photobiological Sciences* **2005**, *4*, 463–468.

[95] E. Sikorska, I. V. Khmelinskii, J. Koput, M. Sikorski, *Journal of Molecular Structure (Theochem)* **2004**, *676*, 155–160.

[96] E. Sikorska, I. V. Khmelinskii, J. Koput, J. L. Bourdelande, M. Sikorski, *Journal of Molecular Structure* **2004**, *697*, 137–141.

[97] A. Tyagi, A. Penzkofer, *Journal of Photochemistry and Photobiology A: Chemistry* **2010**, *215*, 108–117.

[98] O. Stern, M. Volmer, *Physikalische Zeitschrift* **1919**, *20*, 183–188.

[99] J. R. Lakowicz, *Principles of Fluorescence Spectroscopy 2nd ed.*, Kluwer Academic/Plenum Publishers, **1999**.

[100] R. D. Draper, L. L. Ingraham, *Archives of Biochemistry and Biophysics* **1970**, *139*, 265–268.

[101] K. A. Muszkat, T. Wismontski-Knittel, *Biochemistry* **1985**, *24*, 5416–5421.

[102] N. Leesakul, Dissertation, Graz University of Technology, Graz, **2007**.

[103] J. A. Riddick, W. B. Bunger, T. K. Sakano, *Organic Solvents: Physical Properties and Methods of Purification 4th ed.*, Wiley-Interscience, **1986**.

[104] L. Eberson, *Electron Transfer Reaction in Organic Chemistry*, Springer-Verlag, **1987**.

[105] J. B. Birks, *Reports on Progress in Physics* **1975**, *38*, 904–974.

[106] J. A. Degheili, R. M. Moustafa, D. Patra, B. R. Kaafarani, *The Journal of Physical Chemistry A* **2009**, *113*, 1244–1249.

[107] P. Sonar, M. S. Soh, Y. H. Cheng, J. T. Henssler, A. Sellinger, *Materials Research* **2010**, *12*, 3292–3295.

[108] H. Zhang, Y. Wang, K. Shao, Y. Liu, S. Chen, W. Qiu, X. Sun, T. Qi, Y. Ma, G. Yu, Z. Su, D. Zhu, *Chemical Communications* **2006**, 755–757.

[109] J. Kwon, J.-P. Hong, W. Lee, S. Noh, C. Lee, S. Lee, J.-I. Hong, *Organic Electronics* **2010**, *11*, 1103–1110.

[110] A. Rosspeintner, C. Onitsch, G. Gescheidt, *Photophysical Properties of "Pyrene A"*, **2008**.

[111] J. B. Birks, *Photophysics of Aromatic Molecules*, Wiley - Interscience, London, New York, Sydney, Toronto, **1970**.

[112] T. Förster, K. Kasper, *Zeitschrift für Physikalische Chemie N. F.* **1954**, *1*, 275–277.

[113] B. Stevens, E. Hutton, *Nature* **1960**, *186*, 1045–1046.

[114] J. B. Birks in *Academic Press Inc.*, London, pp. 39–73.

[115] K. Zachariasse, *Chemical Physics Letters* **1985**, *113*, 337–343.

[116] M. Goldenberg, J. Emert, H. Morawetz, *Journal of the American Chemical Society* **1978**, *100*, 7171–7177.

[117] G. Liu, J. E. Guillet, *Macromolecules* **1990**, *23*, 4292–4298.

[118] P. Reynders, W. Kuehnle, K. A. Zachariasse, *Journal of the American Chemical Society* **1990**, *112*, 3929–3939.

[119] M. Van der Auweraer, A. Gilbert, F. C. De Schryver, *Journal of the American Chemical Society* **1980**, *102*, 4007–4017.

[120] A. Tsuchida, T. Ikawa, T. Tomie, M. Yamamoto, *The Journal of Physical Chemistry* **1995**, *99*, 8196–8199.

[121] M. J. Snare, P. J. Thistlethwaite, K. P. Ghiggino, *Journal of the American Chemical Society* **1983**, *105*, 3328–3332.

[122] A. C. Benniston, A. Harriman, S. L. Howell, C. A. Sams, Y.-G. Zhi, *Chemistry - A European Journal* **2007**, *13*, 4665–4674.

[123] K. A. Zachariasse, G. Duveneck, R. Busse, *Journal of the American Chemical Society* **1984**, *106*, 1045–1051.

[124] R. Nandy, M. Subramoni, B. Varghese, S. Sankararaman, *The Journal of Organic Chemistry* **2007**, *72*, 938–944.

[125] S. Sankararaman, G. Venkataramana, B. Varghese, *The Journal of Organic Chemistry* **2008**, *73*, 2404–2407.

[126] J. N. Demas, G. A. Crosby, *The Journal of Physical Chemistry* **1971**, *75*, 991–1024.

[127] E. R. Malinowski, *Analytical Chemistry* **1977**, *49*, 612–617.

[128] I. M. Warner, G. D. Christian, E. R. Davidson, J. B. Callis, *Analytical Chemistry* **1977**, *49*, 564–573.

[129] M. Dalibart, *Talanta* **1997**, *44*, 2231–2235.

[130] D. R. Kattnig, A. Rosspeintner, G. Grampp, *Angewandte Chemie (International Edition)* **2008**, *47*, 960–962.

[131] J. Jaumot, R. Gargallo, A. de Juan, R. Tauler, *Chemometrics and Intelligent Laboratory Systems* **2005**, *76*, 101–110.

[132] C. Wurster, R. Sendtner, *Berichte der Deutschen Chemischen Gesellschaft* **1879**, *12*, 1803–1807.

[133] U. Nickel, M. D. G. Garcia-Angel, U. Ramminger, B. Weidinger, *Zeitschrift für Physikalische Chemie (München, Germany)* **2006**, *220*, 497–509.

[134] A. Ito, D. Sakamaki, H. Ino, A. Taniguchi, Y. Hirao, K. Tanaka, K. Kanemoto, T. Kato, *European Journal of Organic Chemistry* **2009**, *2009*, 4441–4450.

[135] S. I. Weissman, *Journal of Chemical Physics* **1954**, *22*, 1135–1136.

[136] L. Michaelis, M. P. Schubert, S. Granick, *Journal of the American Chemical Society* **1939**, *61*, 1981–1992.

[137] R. F. Milligan, *Journal of the American Chemical Society* **1950**, *72*, 2775–2776.

[138] J. Yamauchi, H. Fujita, Y. Deguchi, *Bulletin of the Chemical Society of Japan* **1979**, *52*, 2819–2822.

[139] J. Yamauchi, H. Fujita, *Bulletin of the Chemical Society of Japan* **1990**, *63*, 2928–2932.

[140] G. Grampp, A.-M. Kelterer, S. Landgraf, M. Sacher, D. Niethammer, J. P. Telo, R. M. B. Dias, A. J. S. C. Vieira, *Monatshefte für Chemie* **2005**, *136*, 519–536.

[141] G. Grampp, S. Landgraf, K. Rasmussen, S. Strauss, *Spectrochimica Acta Part A: Molecular and Biomolecular Spectroscopy* **2002**, *58*, 1219–1226.

[142] L. Omelka, S. Ondrášová, L. Dunsch, A. Petr, A. Staško, *Monatshefte für Chemie* **2001**, *132*, 597–606.

[143] F. Gerson, U. Krynitz, H. Bock, *Helvetica Chimica Acta* **1969**, *52*, 2512–2521.

[144] F. Gerson, U. Krynitz, H. Bock, *Angewandte Chemie* **1969**, *81*, 786–787.

[145] H. Bock, J. Meuret, C. Näther, U. Krynitz, *Tetrahedron Letters* **1993**, *34*, 7553–7556.

[146] H. B. Stegmann, K. Hieke, K. B. Ulmschneider, K. Scheffler, *Chemische Berichte* **1976**, *109*, 2243–2258.

[147] G. Angulo, G. Grampp, J. Grilj, P. Jacques, S. Landgraf, A. Rosspeintner, *Journal of Photochemistry and Photobiology A: Chemistry* **2008**, *199*, 204–210.

[148] A. P. Rudenko, A. V. Vasil'ev, *Russian Journal of Organic Chemistry* **1995**, *31*, 1360–1379.

[149] T. Michinobu, C. Boudon, J.-P. Gisselbrecht, P. Seiler, B. Frank, N. N. P. Moonen, M. Gross, F. Diederich, *Chemistry - A European Journal* **2006**, *12*, 1889–1905.

[150] D. R. Duling, *WinSim*, **1995**.

[151] G. Grampp, G. Stiegler, *Zeitschrift für Physikalische Chemie (München, Germany)* **1984**, *141*, 185–200.

[152] J. M. Zwier, A. M. Brouwer, T. Keszthelyi, G. Balakrishnan, J. F. Offersgaard, R. Wilbrandt, F. Barbosa, U. Buser, J. Amaudrut, G. Gescheidt, S. F. Nelsen, C. D. Little, *Journal of the American Chemical Society* **2002**, *124*, 159–167.

[153] J. G. Broadhurst, E. Warhurst, *Journal of the Chemical Society A: Inorganic, Physical, Theoretical* **1966**, 351–352.

[154] R. E. Sioda, D. O. Cowan, W. S. Koski, *Journal of the American Chemical Society* **1967**, *89*, 230–234.

[155] C. S. Johnson Jr., R. Chang, *The Journal of Chemical Physics* **1965**, *43*, 3183–3192.

[156] G. Grampp, P. Pluschke, *Collection of Czechoslovak Chemical Communications* **1987**, *52*, 819–829.

[157] W. Zhang, P. C. Huang, *Materials Chemistry and Physics* **2006**, *96*, 283–288.

[158] B. Valeur, *Molecular Fluorescence: Principles and Applications 1st ed.*, Wiley-VCH Verlag GmbH, Weinheim, New York, Chichester, Brisbane, Singapore, Toronto, **2001**.

[159] Q. Chu, Y. Pang, *Spectrochimica Acta Part A: Molecular and Biomolecular Spectroscopy* **2004**, *60*, 1459–1467.

[160] E. Birckner, U.-W. Grummt, A. H. Goller, T. Pautzsch, D. A. M. Egbe, M. Al-Higari, E. Klemm, *The Journal of Physical Chemistry A* **2001**, *105*, 10307–10315.

[161] A. Beeby, K. Findlay, P. J. Low, T. B. Marder, *Journal of the American Chemical Society* **2002**, *124*, 8280–8284.

[162] J. Eriksen, *The Journal of Physical Chemistry* **1980**, *84*, 276–281.

[163] I. B. Berlman, *Handbook of Fluorescence Spectra of Aromatic Molecules 2nd ed.*, Academic Press, New York and London, **1971**.

[164] C. Aurisicchio, B. Ventura, D. Bonifazi, A. Barbieri, *The Journal of Physical Chemistry C* **2009**, *113*, 17927–17935.

[165] D. Greatorex, T. J. Kemp, J. P. Roberts, *The Journal of Physical Chemistry* **1969**, *73*, 1616–1617.

[166] T. Okada, H. Oohari, N. Mataga, *Bulletin of the Chemical Society of Japan* **1970**, *43*, 2750–2758.

[167] K. Kikuchi, T. Niwa, Y. Takahashi, H. Ikeda, T. Miyashi, *The Journal of Physical Chemistry* **1993**, *97*, 5070–5073.

[168] M. Z. Zgierski, E. C. Lim, *Chemical Physics Letters* **2004**, *387*, 352–355.

[169] T. Fujiwara, M. Z. Zgierski, E. C. Lim, *The Journal of Physical Chemistry A* **2008**, *112*, 4736–4741.

[170] J. Catalán, *The Journal of Physical Chemistry B* **2009**, *113*, 5951–5960.

[171] E. Lippert, *Zeitschrift für Elektrochemie, Berichte der Bunsengesellschaft für physikalische Chemie* **1957**, *61*, 962–975.

[172] W. Liptay, *Zeitschrift für Naturforschung* **1965**, *20a*, 1441–1471.

[173] R. Noto, M. Leone, G. La Manna, F. Brugè, S. L. Fornili, *Journal of Molecular Structure (Theochem)* **1998**, *422*, 35–48.

[174] G. Angulo, G. Grampp, A. Rosspeintner, *Spectrochimica Acta Part A: Molecular and Biomolecular Spectroscopy* **2006**, *65*, 727–731.

[175] S.-i. Kato, M. Kivala, W. B. Schweizer, C. Boudon, J.-P. Gisselbrecht, F. Diederich, *Chemistry - A European Journal* **2009**, *15*, 8687–8691.

[176] W. Schroth, S. Dunger, F. Billig, R. Spitzner, R. Herzschuh, A. Vogt, T. Jende, G. Israel, J. Barche, D. Ströhl, *Tetrahedron* **1996**, *52*, 12677–12698.

[177] M. Kivala, Dissertation, Eidgenössische Technische Hochschule Zürich, **2007**.

[178] M. Kivala, T. Stanoeva, T. Michinobu, B. Frank, G. Gescheidt, F. Diederich, *Chemistry - A European Journal* **2008**, *14*, 7638–7647.

[179] J. B. Flanagan, S. Margel, A. J. Bard, F. C. Anson, *Journal of the American Chemical Society* **1978**, *100*, 4248–4253.

[180] M. Kivala, C. Boudon, J.-P. Gisselbrecht, P. Seiler, M. Gross, F. Diederich, *Angewandte Chemie (International Edition)* **2007**, *46*, 6357–6360.

[181] P. Reutenauer, M. Kivala, P. D. Jarowski, C. Boudon, J.-P. Gisselbrecht, M. Gross, F. Diederich, *Chemical Communications* **2007**, 4898–4900.

[182] M. Kivala, C. Boudon, J.-P. Gisselbrecht, P. Seiler, M. Gross, F. Diederich, *Chemical Communications* **2007**, 4731–4733.

[183] M. Kivala, F. Diederich, *Accounts of Chemical Research* **2009**, *42*, 235–248.

[184] D. F. Perepichka, M. R. Bryce, *Angewandte Chemie (International Edition)* **2005**, *44*, 5370–5373.

[185] M. Kivala, C. Boudon, J.-P. Gisselbrecht, B. Enko, P. Seiler, I. B. Müller, N. Langer, P. D. Jarowski, G. Gescheidt, F. Diederich, *Chemistry - A European Journal* **2009**, *15*, 4111–4123.

[186] X. Zhang, Z.-C. Li, K.-B. Li, S. Lin, F.-S. Du, F.-M. Li, *Progress in Polymer Science* **2006**, *31*, 893–948.

[187] S.-l. Zhang, M. J. Lang, S. Goodman, C. Durnell, V. Fidlar, G. R. Fleming, N.-c. C. Yang, *Journal of the American Chemical Society* **1996**, *118*, 9042–9051.

[188] W. D. Philipps, J. C. Rowell, *The Journal of Chemical Physics* **1960**, *33*, 626–627.

[189] F. Gerson, R. Heckendorn, D. O. Cowan, A. M. Kini, M. Maxfield, *Journal of the American Chemical Society* **1983**, *105*, 7017–7023.

[190] B. Breiten, Y.-L. Wu, P. D. Jarowski, J.-P. Gisselbrecht, C. Boudon, M. Griesser, C. Onitsch, G. Gescheidt, W. B. Schweizer, N. Langer, C. Lennartz, F. Diederich, *Chemical Science* **2010**, *submitted.*